Université de Montréal

Characterization of mineral dust emitted from an actively retreating glacier in Yukon, Canada

par Jill Bachelder

Département de Chimie, l'Université de Montréal
Faculté des Arts et Sciences

Mémoire présentée
en vue de l'obtention du grade de M.Sc.
en chimie
option chimie analytique

25 avril 2019

© Jill Bachelder, 2019

Université de Montréal
Département de Chimie, Faculté des Arts et Sciences

Ce mémoire intitulé

Characterization of mineral dust emitted from an actively retreating glacier in Yukon, Canada

Présenté par

Jill Bachelder

A été évalué par un jury composé des personnes suivantes

Kevin Wilkinson

Président-rapporteur

Patrick Hayes

Directeur de recherche

Pierre Chaurand

Membre du jury

Résumé

La poussière minérale atmosphérique émise dans les régions arctiques peut modifier de manière significative le bilan énergétique de l'atmosphère nordique en diffusant et en absorbant la radiation. La poussière joue également un rôle important dans le cycle biogéochimique des métaux et peut avoir des effets négatifs sur la qualité de l'air et la santé publique. L'impact des sources de poussière du Nord sur l'atmosphère et l'environnement peut changer rapidement, car le réchauffement du climat dans le Nord peut augmenter la production de poussière minérale et peut affecter les régions d'origine. Cependant, à l'heure actuelle, l'impact de ces changements est difficile à évaluer, car très peu d'études scientifiques effectuent des mesures directes des émissions de poussières minérales ainsi que des propriétés chimiques et microphysiques des poussières minérales dans les régions arctiques. Pour combler cette lacune, nous avons fait des mesures de la poussière minérale en juin 2017 et en mai 2018 près de l'Ä'äy Chù (rivière Slims), dans une vallée proglaciale du Yukon, qui est un site important des émissions de la poussière. Le changement climatique a eu de lourdes conséquences sur la vallée d'Ä'äy Chù. Le retrait rapide du glacier Kaskawulsh laissant le lit de la rivière exposé augmentant ainsi potentiellement sa surface érodable qui peut produire de la poussière. Nous avons collecté des échantillons d'aérosols (PM_{10} et poussières minérales déposées) dans toute la vallée Ä'äy Chù et avons enregistré des données météorologiques afin d'établir un lien entre des facteurs environnementaux et l'émission de poussières. Nous avons également utilisé une méthode quantitative pour analyser les métaux traces dans les poussières minérales par spectrométrie de masse à plasma à couplage inductif (ICP-MS) afin de quantifier les métaux traces dans les échantillons de PM_{10}, du sol et de poussières minérales déposées.

Notre étude est la première à mener une caractérisation chimique et microphysique des poussières minérales émises directement par une source de poussière de haute latitude au Canada. L'analyse des données obtenues par un compteur de particules optiques (OPC) a indiqué à quelle heure des événements de poussière se sont produits pendant la journée, tandis qu'une analyse gravimétrique d'échantillons de filtres a montré des concentrations ambiantes

entre 240 µg / m³ et 3 950 µg / m³ à la source des poussières. En outre, les seuils de qualité de l'air de l'Organisation de la Santé Mondial (OSM) ont été dépassés aux sites proches de la source de poussière, notamment au centre des visiteurs Thachäl Dhäl géré par Parcs Canada et à un site situé à proximité de la route de l'Alaska. Nous n'avons pas réussi à analyser nos échantillons en utilisant l'ablation au laser ICP-MS et l'ICP-MS à particule unique. Néanmoins, nous avons validé avec succès un protocole d'analyse ICP-MS d'échantillons digérés et avons ainsi pu appliquer cette technique à l'analyse de nos échantillons. L'analyse de la composition élémentaire par ICP-MS a révélé l'enrichissement en échantillons de PM_{10} de la composition des éléments mineurs et des éléments traces par rapport aux sols, généralement par un facteur de 1,5 à 2. De plus, une analyse SEM / EDS a démontré que les poussières émises se composent principalement de particules non sphériques composées d'agrégats minéraux d'argile aluminosilicate. Enfin, nous avons calculé le flux vertical de masse de particules, et nous avons utilisés le flux, la distribution de taille et la composition du PM_{10} afin d'évaluer plusieurs théories relatives au mécanisme prédominant d'émission de poussière qui se produit dans la vallée d'Ä'äy Chù.

Mots-clés : La poussière minérale, Nord du Canada, Chimie atmosphérique, Aérosols, Changement climatique

Abstract

Airborne mineral dust emitted in Arctic regions can significantly alter the energy balance of the Northern atmosphere through scattering and absorption of radiation; dust also plays an important role in the biogeochemical cycling of metals and can have deleterious effects on air quality and public health. The impact of northern dust sources on the atmosphere and environment may change rapidly, as warming temperatures in the North can increase mineral dust production and source regions by inducing topographical changes due to rapid glacier ablation. However, at present, the impact of such changes is difficult to evaluate because there are very few scientific studies that perform direct field measurements of mineral dust emissions as well as of mineral dust chemical and microphysical properties in Arctic regions. To address this knowledge gap, we performed mineral dust measurement campaigns in June 2017 and May 2018 near the Ä'äy Chù (Slims River), within a proglacial valley in Yukon, Canada that has exhibited strong dust emissions. The Ä'äy Chù Valley has been impacted heavily by climate change, as the rapid retreat of the adjacent Kaskawulsh glacier, recently routed waters away from the river valley, leaving the riverbed exposed and thus potentially increasing its dust-producing erodible surface area. We have collected aerosol samples (PM_{10} and deposited mineral dust) throughout the Ä'äy Chù Valley, and have recorded weather data to establish a link between environmental factors and the emission of dust. We have also employed an efficient, quantitative method for analysis of trace metals in mineral dust via inductively coupled plasma mass spectrometry (ICP-MS) to quantify trace metals in PM_{10} samples, soil and in deposited mineral dust samples.

Ours is the first field campaign to provide chemical and microphysical characterization of mineral dust emitted directly from a high-latitude dust source in Canada. Analysis of data obtained by an optical particle counter (OPC) indicated dust events occurred during both daylight and non-daylight hours, while gravimetric analysis of filter samples found ambient concentrations ranging between 240 $\mu g/m^3$ and 3950 $\mu g/m^3$ at the dust source during the course of the dust observation campaign. Furthermore, air quality thresholds of the World Health Organization (WHO) were exceeded at sites near the dust source, including at the

Thachäl Dhäl Visitor's Center run by Parks Canada and a site next to the Alaska Highway. We were unable to successfully analyze our samples using laser ablation ICP-MS and single particle ICP-MS. Nevertheless, we successfully validated a protocol for performing ICP-MS analysis of digested samples and were thus able to apply this technique to the analysis of our samples. Analysis of elemental composition via ICP-MS has revealed enrichment of minor and trace element content in ambient air samples as compared to soils and dust deposition, generally by a factor of 1.5 to 2. Moreover, SEM/EDS analysis has demonstrated that the emitted dust primarily consists of non-spherical particles composed of aluminosilicate clay mineral aggregates. Finally, we have calculated the vertical flux of particulate mass, and have used the flux, the size distribution, and the composition of both PM_{10} and soil samples to evaluate several theories related to the predominant dust emission mechanism that occurs in the Ä'äy Chù Valley.

Keywords : Mineral dust, Canadian North, Atmospheric chemistry, Aerosols, Climate change

Table des matières

Liste des tableaux

Liste des figures

Liste des sigles

APS**:** Aerodynamic Particle Sizer

HLD**:** High-Latitude Dust

HLDE**:** High-Latitude Dust Emissions

ICP-AES: Inductively Coupled Plasma – Atomic Emission Spectroscopy

ICP-AAS: Inductively Coupled Plasma – Atomic Absorption Spectroscopy

ICP-MS**:** Inductively Coupled Plasma – Mass Spectrometry

ICP-OES: Inductively Coupled Plasma – Optical Emission Spectroscopy

INAA: Instrumental Neutron Activation Analysis

LA-ICP-MS**:** Laser Ablation – Inductively Coupled Plasma – Mass Spectrometry

LPM**:** Liters Per Minute

OPC**:** Optical Particle Counter

OMS: *Organisation Mondial de la Santé*

PIXE: Particle Induced X-ray Emission

PM_1**:** Particulate matter smaller than 1 µm in diameter.

$PM_{2.5}$**:** Particulate matter smaller than 2.5 µm in diameter; a class of particles used by air quality monitoring agencies to gauge the potential health effects of fine ambient aerosols.

PM_{10}**:** Particulate matter smaller than 10 µm in diameter; a class of particles used by air quality monitoring agencies to gauge the potential health effects of coarse ambient aerosols.

SEM/EDS**:** Scanning Electron Microscopy – Energy Dispersive X-Ray Spectroscopy

SP-ICP-MS**:** Single Particle – Inductively Coupled Plasma – Mass Spectrometry

SP-ICP-TOF-MS**:** Single Particle – Inductively Coupled Plasma – Time of Flight – Mass Spectrometry

U.S. EPA**:** United States Environmental Protection AgencyWHO **:** World Health Organization

XRD: X-Ray powder Diffraction

XRF: X-Ray Fluorescence

Liste des abréviations

Aucunes.

For my Ah Mah and Ah Gong.

Remerciements

Thank you to Patrick L. Hayes, James King, and Kevin J. Wilkinson for supervising my work on this project and for obtaining the funds and resources necessary for my fieldwork and analyses. I have truly enjoyed working on this project and am grateful for having had the opportunity to perform fieldwork and travel to conferences in Quebec, Ontario, and Iceland. In addition, I am grateful for the professional development resources provided by these truly kind professors, such as advice on future career options, graduate school programs, and the provision of numerous letters of recommendation.

I am also grateful for the contribution of the community members with whom I have worked in Yukon, including but not limited to Sian and Lance Goodwin of Outpost Research Station, James Allen of the Shakat Tun Wilderness Camp, and Alex Bouchard of Parks Canada. Their aid and support for the completion of our fieldwork, as well as their enthusiasm in learning about the results of our experiments, were highly motivating and helped me understand the broader implications of our research at the dust at Kluane Lake.

One of the highlights of my time as a master's student at Université de Montréal was the opportunity to work on this project with so many wonderful interns, graduate students, and post-doctoral fellows. I would like to offer my sincerest thanks to the undergraduate interns, Carolyn Liu-Kang, Marie Cadieux, and Marie-Pierre Bastien-Thibaut; my fellow graduate students, Pérrine Lambert, Alexane Filoche, and Amélie Chaput; and the post-docs, Juliana Galhardi and Miriam Hurkuck, all of whom I feel so lucky to have known and worked with. Known collectively as the « dust girls » by our hosts at Kluane Lake, it cannot be denied that the contribution of each and every one of these students and employees has been vital for the realization of the research presented in this thesis, and I strongly believe that the future success of the project on dust emissions from Kluane Lake will be in large part due to the powerful legacy and the amazing work of these incredible women in science. Moving forward, I am so excited to see where life takes each and every one of them, and I wish them all the best.

Finally, I would like to end this section by expressing my graditude for the support of all the students and employees in the department of chemistry at UdeM who have supported

me and aided in this research. In particular, the laboratories of the Hayes Group, the LEE Group (in the department of geography), and the Wilkinson Group deserve many thanks. From Madjid Hadioui, who was so kind and patient during my ICP-MS analyses and always willing to help and answer questions, to Kevin Delorme, for allowing me to borrow his vacuum pumps whenever I needed them, to even the Sauve lab, who allowed me to keep my filter samples in their freezer and my pet crayfish in their kitchen, I have truly enjoyed my experience as a student at UdeM and am grateful for all the friends and acquaintences I have made at this university.

Chapter 1 – Introduction

Mineral dust is the most abundant total suspended particle aerosol species in the atmosphere and plays an important role in many atmospheric and environmental processes (Formenti et al. 2003). It can interact with atmospheric radiation directly, by scattering and absorbing radiation, and indirectly, by acting as cloud condensation nuclei or ice nuclei (Huang et al. 2006; Lohmann and Diehl 2006; Sokolik and Toon 1996). Furthermore, mineral dust can transport nutrients to aquatic and terrestrial environments; it can also take part in heterogeneous chemical reactions that can alter the composition of the atmosphere and can negatively impact air quality and public health (Avila et al. 1998; Phalen et al. 1991; Prospero 1999b; Usher et al. 2002).

Emissions of particulate matter can greatly impact the atmosphere of Arctic and sub-Arctic regions, as its radiative effects are more pronounced in the pristine air of the North. In addition, the dust emitted from these regions has been shown to make up 90% of mineral deposition in the North, and thus likely plays a much larger role in provision of minerals to local ecosystems as compared to dust transported to the North from lower-latitude sources (Groot Zwaaftink et al. 2016). Moreover, the rapid warming of the North has induced topographical changes that have potentially created new dust sources or altered the emissions of existing sources – these changes will likely continue as Northern temperatures continue to rise. However, despite its significance, there are very few scientific studies that characterize mineral dust in Arctic regions.

For these reasons, we have collected airborne particulate matter samples near the Ä’äy Chù (Slims River) in the Canadian Yukon, a location at which dust storms are regularly produced during the spring and summer, and whose topography has been greatly impacted due to climate change (Shugar et al. 2017). Through our analysis, we hope to characterize the collected dust by determining its composition, morphology, and processes of emission, while developing a method for performing this analysis that allows sample collection and instrument maintenance in the harsh and remote conditions of the Canadian North.

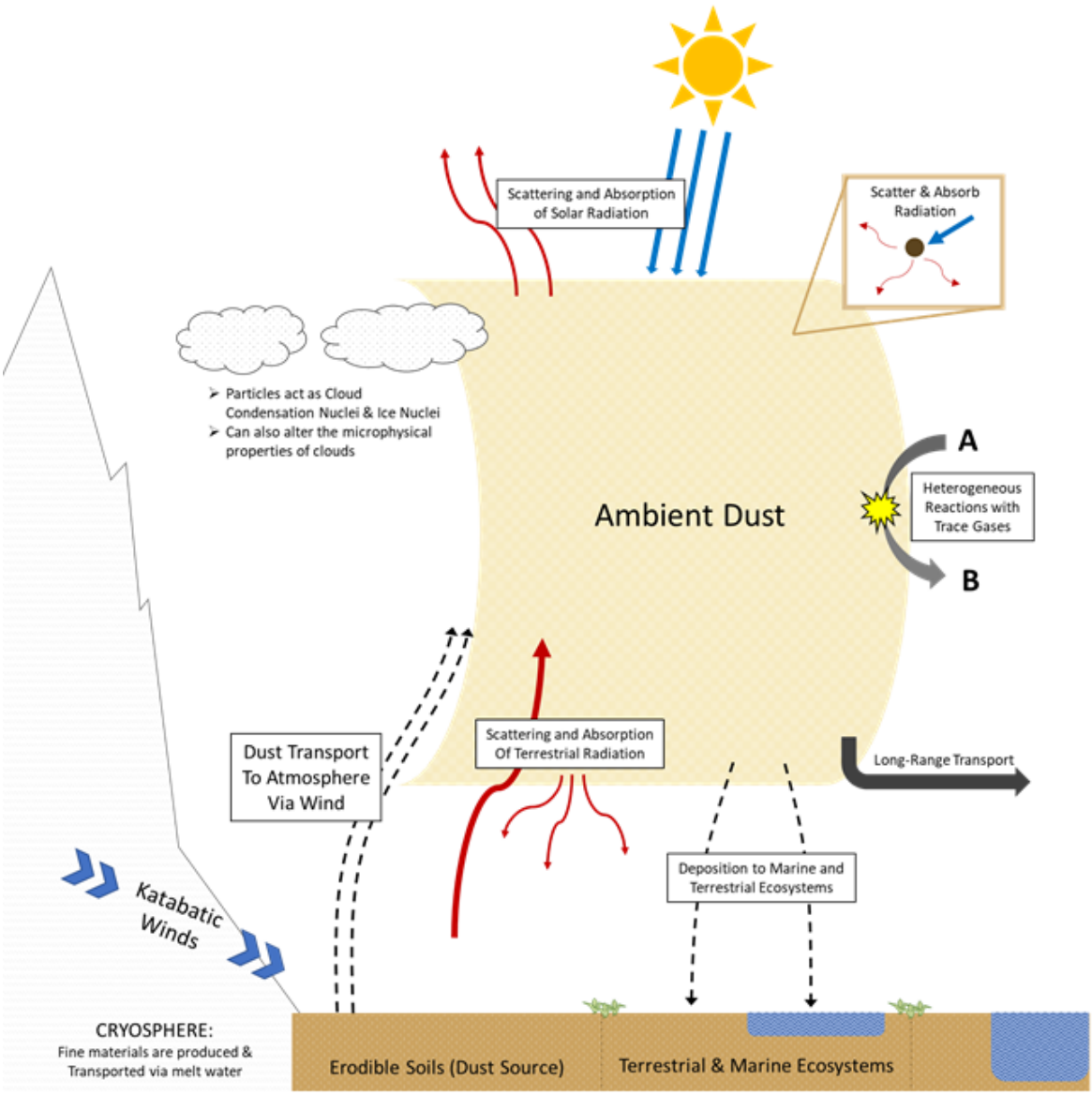

Figure 1-1. Schematic detailing the processes of mineral dust emission as well as subsequent atmospheric and environmental impacts in high latitude regions. (Adapted from: Bullard, J. E. et al., High-latitude dust in the Earth system. *Reviews of Geophysics* **2016,** *54* (2), 447-485.)

1.1 Mineral dust in the atmosphere and environment

As mineral dust is pervasive in the environment and exists in large quantities in the atmosphere, it is important to understand the impact mineral dust can have on atmospheric

radiative forcing, heterogeneous chemistry in the atmosphere, biogeochemical cycling of minerals, and public health. It is evident that the size distribution, shape characteristics, and chemical composition of mineral dust ultimately determine the effect it will have on the atmosphere and environment. These qualities are not independent, and are often highly correlated; for example, the overall elemental or mineralogical composition may change depending on the particle size range, with certain minerals dominating the coarse fraction and others dominating the fine fraction. Thus, an all-encompassing analysis of the size, composition, and morphology of ambient mineral dust is necessary to gauge its behavior and impact. A summary graphic that includes the impact of dust on the atmosphere and environment is provided in Figure 1-1.

1.1.1 Radiative forcing

The energy in the earth's atmosphere is provided by incoming solar radiation. This radiation can be reflected back into space, absorbed by the earth, or lost from the earth through emission of infrared radiation. The imbalance between incoming and outgoing radiation is known as "radiative forcing" and can ultimately have either a net warming or net cooling of the planet (Seinfeld and Pandis 2006). There are a variety of atmospheric factors that can influence radiative forcing, including the reflectivity of the Earth's surface, the presence of greenhouse gases such as carbon dioxide, and interaction of radiation with clouds or particulate matter in the atmosphere (Seinfeld and Pandis 2006). It is important for global climate models to be able to quantify the degree to which anthropogenic and natural emissions will influence radiative forcing, in order to predict a timeline for the future warming of the planet. However, the uncertainties present in recent attempts to quantify the impact of anthropogenic activity on radiative forcing are so large that predictions of future climate change have uncertainties of several degrees Celsius – this is largely due to a lack of understanding of direct and indirect effects of ambient aerosol species on the radiative balance of the atmosphere (Figure 1-2) (Stocker et al. 2013). Among these aerosols, the contribution of mineral dust to radiative forcing has not been well quantified in global climate models (Stocker 2014).

Atmospheric aerosols, including mineral dust, can influence radiative forcing directly, through scattering and absorption of light by individual particles. They can also indirectly affect radiative forcing by serving as cloud condensation nuclei (CCN) or ice nuclei (IN), influencing the formation of clouds that can themselves alter the radiative balance of the atmosphere. The optical properties of a given particle and its CCN or IN activity are determined by its size, morphology, and chemical composition; thus, characterization of these factors is crucial to determining the impact a given dust source will have on both indirect and direct radiative forcing (Stocker 2014).

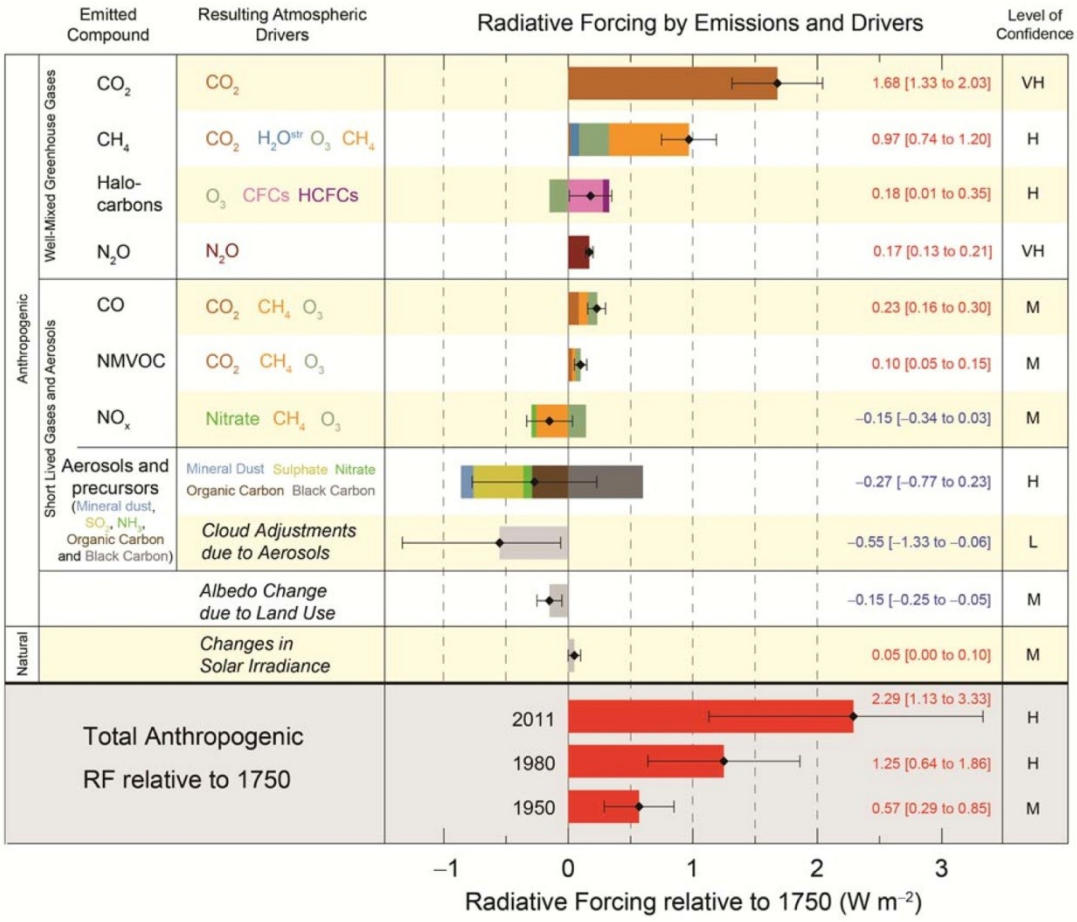

Figure 1-2. Radiative forcing estimates and uncertainty resulting from anthropogenic activity, which demonstrates that the majority of uncertainty lies in predictions of aerosol direct and indirect radiative effects. Figure provided by the International Panel on Climate Change AR5 2013 report. (Image Source: Stocker, T. F. et al., Climate change 2013: the physical science basis. Intergovernmental panel on climate change, working group I contribution to the IPCC fifth assessment report (AR5). *New York* **2013**.)

The size distribution of mineral dust in the atmosphere is often very large, as dust can exist anywhere in the range of nanometers to hundreds of microns (Archuleta et al. 2005; Betzer et al. 1988). Particles in the size range of fifty to several hundred nanometers greatly influence the ability of mineral dust to act as CCN; Dusek et al. (2006) demonstrated that mineral dust CCN activity depends more strongly on the particle number distribution, in which the smallest particles are most abundant, than it does on chemical composition. With regard to larger mineral dust particles, model studies have indicated that increased presence of particles in the coarse mode (which comprises particles between 2.5 and 10 μm in diameter) generally produce more of a warming direct effect, and that the distribution of sizes within this coarse mode can significantly alter the overall radiate effects of the dust (Otto et al. 2007).

In addition, particle size is proportional to atmospheric lifetime, as larger particles are more prone to deposition due to their larger mass; particles with diameters less than 10 μm (PM_{10}) are better able to undergo long-range transport in the atmosphere (Mahowald et al. 2014; Prospero 1999a). As a result, the effects of PM_{10} on radiative forcing can be felt over a wider area and for a longer period of time than those of larger particles. This further emphasizes the importance of the size distribution of mineral dust to characterize the dust's potential impact on radiative forcing.

The shape of mineral dust particles is highly variable and rarely spherical, and this non-sphericity can greatly influence the optical properties of the dust. The physics of light scattering and absorption by particles with irregular shapes is extremely complex as compared to that of spherical particles, and applications of Mie theory used in most atmospheric studies – which assume that light is scattered by spherical particles with a smooth surface – are not applicable to mineral dust (Mishchenko et al. 1999). Thus, non-sphericity may contribute error to model studies that assume all particles are spherical. Kalashnikova et al. (2004) found that non-spherical particle shapes had greater extinction coefficients and single-scattering albedo when compared to their spherical counterparts; they attributed this difference to the increased surface area resulting from the angularity and non-sphericity of the particles. Furthermore, the

results of their study indicated that the assumption of sphericity could lead to a significant underprediction of radiative forcing if calculated on the global scale (Kalashnikova and Sokolik 2004).

Chemical composition is another factor that can greatly influence the contribution of mineral dust to radiative forcing. Mineral dust is typically externally mixed and comprised of a wide range of minerals (Falkovich et al. 2001). The ability of a particle to scatter and absorb light depends greatly on the particle's mineralogy (Lide 1964). As a result, direct radiative forcing depends greatly on the mineralogy of the dust in the atmosphere. There have been many studies that demonstrate the effect of mineralogy on radiative forcing – for example, it has been shown that hematite content is a major factor that determines the capacity of the dust to absorb radiation (Dubovik et al. 2002). Indeed, darker minerals such as iron oxides form the component of dust that is more able to absorb at wavelengths in the visible range.

Chemical composition can also influence the indirect effects of mineral dust on radiative forcing (Haywood and Boucher 2000). Laboratory studies have demonstrated carbonate particles to be favorable for the formation of CCN as a result of atmospheric reactions with nitrogen-containing trace gases that increase the hygroscopicity of these minerals; clay particles such as kaolinite and illite are generally thought to be responsible for the formation of IN, though recent studies suggest feldspar may also play a significant role (Atkinson et al. 2013; Krueger et al. 2004; Mason and Maybank 1958; Sullivan et al. 2009). Consequently, a more complete understanding of mineralogy will aid in model predictions of the influence of mineral dust aerosols on the radiative balance of the atmosphere.

1.1.2 Impact of mineral dust on nutrient cycling

In addition to its radiative effects, mineral dust can impact the biogeochemical cycling of nutrients when it is deposited in the local environment. This is because deposition of mineral dust can serve as a source of P, soluble Fe, and various minor and trace elements, which in turn can influence primary productivity in both terrestrial and marine ecosystems (Prospero et al. 1987; Richon et al. 2018; Schroth et al. 2009; Shelley et al. 2012). The effect of mineral dust on biogeochemical cycling of elements relies on the bioavailability of the deposited

minerals – this is influenced by a wide array of factors, including the speciation and solubility of the various mineral dust components in the aqueous matrix (Schulz et al. 2012). Thus, though determination of the total elemental content of dust deposition is a key step in evaluating its impact on the local environment, further analysis of the bioavailability of the nutrient is needed to fully illustrate the effect that dust deposition will have on both marine and terrestrial ecosystems. While the impact of minor and trace elements on marine ecosystems is dictated by the bioavailability of the elements in question once deposition has occurred, many studies choose to use solubility as a proxy for bioavailability as this is much simpler to determine (Fan et al. 2006). However, solubility and bioavailability of a given species in the environment are not interchangeable, as there are many factors that may influence bioavailability in addition to solubility, such as complexation and redox chemistry (Lis et al. 2014).

Iron is an important micronutrient that marine phytoplankton use during both photosynthesis and respiration processes (Morel et al. 1991; Ye and Völker 2017). The importance of mineral dust in transporting and depositing soluble iron has been well-documented, and it has even been shown that mineral dust is the dominant source of iron in certain marine regions (Ye and Völker 2017). However, soluble iron content is not consistent and depends on the chemical composition of the dust deposited, with certain iron-containing minerals, such as clays, possessing much higher solubility as compared to others, such as magnetite, hematite, and goethite (Journet et al. 2008). Thus, it has been demonstrated that the soluble iron content varies in the soils of dust source regions, with glacial flour (whose iron content is primarily in the form of iron-containing silicates) possessing higher levels of soluble iron as compared to soils from typical arid regions, which possess a larger fraction of iron oxides and hydroxides (Schroth et al. 2009). As dissolved iron tends to adsorb to the surfaces of particles suspended in seawater, the deposition of mineral dust into marine ecosystems can also serve as a soluble iron sink (Ye and Völker 2017). Furthermore, atmospheric processes can alter the solubility, as well as the bioavailability, of the iron contained in mineral dust. For example, it was found that atmospheric processing can lead to the formation of iron nanoparticles which are more bioavailable than the original iron contained in mineral dust particles (Shi et al. 2009; Shi et al. 2015).

While iron is by far the most widely discussed component of mineral dust in relation to biogeochemical cycling of metals, there are several other minor and trace elements essential for primary production. We will restrict our discussion of these elements to those we have analyzed in our current study. Cobalt is involved in the synthesis of vitamin B12 in marine phytoplankton, and can also act as a co-factor in enzymatic processes that allow phytoplankton uptake of inorganic dissolved carbon (Lane and Morel 2000; Shelley et al. 2012). Dust is also a major source of atmospheric nickel globally, as 30-50% of natural nickel emissions occur via wind-blown dust (Sigel et al. 2007), and is essential for the conversion of urea to usable ammonia in plants (Witte 2011). Elevated nickel concentrations can be toxic, while nickel deficiency can also negatively impact plant growth (Brown et al. 1987; Sigel et al. 2007). Dust deposition can also be a source of manganese, which may trigger slight growth in phytoplankton when enriched (Baker et al. 2006; Buma et al. 1991). Copper is an essential micronutrient, the depletion of which may decrease the rate of metabolic processes in phytoplankton; demand for copper can be further increased in iron-depleted environments (Posacka et al. 2017). As arsenic is naturally occurring in both lakes and sediment, it can be a significant component of natural emissions of wind-blown dust (Cutter et al. 2001; Thornton 1996). Arsenic speciation determines its toxicity, with the inorganic arsenate and arsenite species – As(V) and AS(III), respectively – being more toxic than organic arsenic compounds (Pongratz 1998). Elevated levels of lead and cadmium are associated with anthropogenic activity, though these elements may also exist naturally at trace levels in soils and sediment (Alloway and Steinnes 1999; Hutton 1983; Lepow et al. 1975). All the aforementioned trace elements become toxic when present at highly elevated concentrations.

When discussing the impact of trace element deposition on the environment, it is also important to consider the interdependence of micronutrient effects. Many studies have indicated a co-limiting process occurs in which the primary productivity is controlled by several nutrients, as opposed to a single limiting nutrient (Moore et al. 2013). Finally, while it is not analyzed in this work, it is important to note that mineral dust can be a very important source of nitrogen and phosphorus for both marine and terrestrial ecosystems.

1.1.3 Impact on air quality and public health

Atmospheric particulate matter can have a significant impact on local communities. Wind-blown dust storms can cause decreased visibility, resulting in hazardous conditions for road and air traffic. Furthermore, particles smaller than 10 μm in diameter (PM_{10}) can have a negative impact on lungs and heart health. The size distribution of PM_{10} dictates how far the particles are able to penetrate into the respiratory and pulmonary systems (Phalen et al. 1991). Air quality guidelines provided by the U.S. Environmental Protection Agency (EPA) and the World Health Organization (WHO) give 24-hr air quality standards for ambient PM_{10} concentrations. That of the U.S. EPA is 150 $\mu g/m^3$, which should not be surpassed more than once per year on average over 3 years. The guideline set by the WHO of 50 $\mu g/m^3$ is a target value for limiting risks to public health (WHO 2006). These guidelines indicate the levels of PM_{10} that may induce short-term or long-term health impairments, including premature death, decreased lung function, decreased heart health, and the exacerbation of respiratory conditions such as asthma (Kelly and Fussell 2015).

1.2 Mineral dust at high latitudes

High-latitude dust (HLD) is defined as wind-blown re-suspended particulate matter that is emitted either north of 50°N or south of 40°S (Bullard et al. 2016). Until recently, high-latitude dust emission (HLDE) sources have been overlooked by researchers of dust, who typically focus on a few key dust emission sources in Sub-Central Africa, Central Asia, the Middle East, and the Southeast United States. After a study by Bullard et al. (2016) identified the potential significance of HLD both regionally and globally, there has been a growing effort to characterize the frequency, magnitude, and correlation of HLDE with meteorological factors such as temperature, wind speed and direction, and precipitation. This analysis is crucial for determining the impact of HLDE on the radiative balance and biogeochemical cycling of nutrients in high-latitude regions.

1.2.1 Emissions mechanisms of Northern dust

While it is unknown which dust emissions mechanisms dominate at high latitudes, there are several possible dust emission mechanisms that are known to take place. An important process that leads to the emission of wind-blown dust is the saltation-sandblasting mechanism (Gillies and Berkofsky 2004). Saltation occurs when large particles, projected through the air by turbulent winds, impact with the surface; sandblasting is the release of fine particulate matter as a result of the saltation process (Grini and Zender 2004). The saltation-sandblasting mechanism can lead to the emission of wind-blown dust if fine particulate matter is released from surface soils by the saltating particle, or if the saltating particle itself disintegrates upon impact with the surface, leading to the release of fine materials. Furthermore, the presence of fine particulate matter coatings, such as clays, on larger particles can lead to dust production if this coating is shattered during saltation. The impact of saltating particles can also lead to the abrasion of larger particles, chipping off smaller pieces of these particles which can contribute

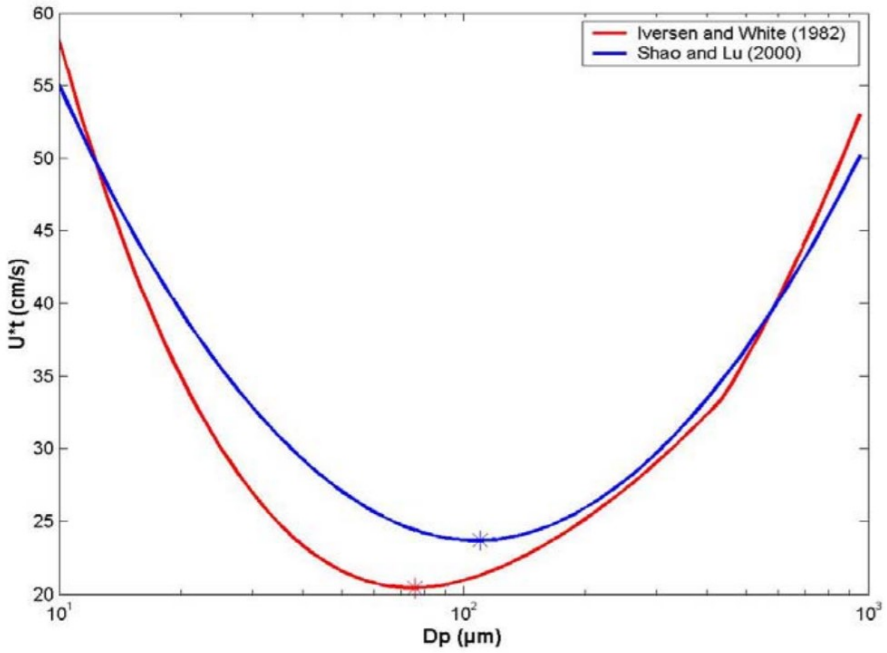

Figure 1-3. Plot showing the relationship between threshold shear velocity (u^*_t) and particle diameter (D_p) for particles emitted through direct entrainment, parameterized based on studies of well-characterized low-latitude dust sources, such as the Sahara Desert. (Image Source: Bergametti, G., *Dust emission processes*. 2004.)

to the emission of dust (Huang et al. 2019).

In addition to the saltation-sandblasting mechanism, dust can be levitated directly into the atmosphere by aeolian, or wind-related, processes (Huang et al. 2019). However, this is not thought to be a dominant dust emission mechanism, as particles in the smaller size range that are most dominant in mineral dust (less than 100 μm in diameter) are not entrained in significant quantities this way as they do not possess enough drag to be lifted into the air (Figure 1-3) , although there has been some evidence that particles smaller than 10 μm in diameter can be entrained in the absence of saltation (Bergametti 2004; Harris and Davidson 2009). Furthermore, this theory is based on the conditions of well-characterized low-latitude dust sources – the increased air density and turbulence in the North alter the drag forces to which particles are subjected (Bullard et al. 2016), and this may affect the particle size range subjected to direct entrainment. There have been no studies that detail which dust emission mechanism dominates at high-latitude dust sources; as a result, while the potential dust emissions mechanisms are known, it is unclear which processes occur at high latitudes.

Source regions and meteorological conditions at high-latitudes are quite different than those at their more extensively studied low-latitude counterparts. As noted previously, an overview of dust emission and transport processes at high latitudes, based on the work of Bullard et al (2016), is provided in Figure 1-1. Many important HLD emitting sources are located in pro-glacial regions, or regions that are adjacent to glacier activity. These areas are characterized by intense and complex wind systems with strong ice sheet and katabatic winds originating from both the glacier mass and mountainous terrain of Northern regions. There exists much higher variability in altitude and topography in the North as compared to the relatively leveled desert dust sources at low-latitudes, and this can result in lee effects (because as winds travel over mountainous regions, wind speed and direction may be impacted), converging and diverging winds, and friction effects that further result in the unpredictability of the wind systems up North (Ed Hudson 2001). As discussed in the previous paragraph, the cold air of the North is able to exert a larger drag force on particles, as it is characterized by higher density and a greater intensity of turbulence, and thus for a given wind speed may be more effective in suspending particles than the warmer winds of low-latitude regions (Bullard et al. 2016).

Moreover, the erodible sediments in these regions that are conducive to the production of dust typically comprises either glacial flour, volcanic ash deposits, or are the result of anthropogenic activity, such as over-grazing of fields by the agricultural industry (Bullard et al. 2016). The wide range of geological systems in which erodible soils at high latitudes are found translates to high variation in the particle sizes, morphology, and chemical composition of the emitted dust as compared to the erodible sediment of low-latitude dust sources, whose composition is more consistent from one site to the next. The particle sizes of the erodible sediment at high-latitudes, and in turn the emitted dust, are also quite different from those at low latitudes (Arnalds 2004; Nickling 1978; Stuut et al. 2009). This likely means that established dust emissions flux parameterizations, which have been validated using specifically low-latitude sediment such as from the Sahara Desert (Zhang et al. 2013), may require modification before they are applicable to HLDE. The seasonality of HLDE sources is noteworthy in that dust activity is often highest in the spring and summer, when there is less glacier run-off due to lower temperatures, decreasing soil moisture and thus increasing soil erodibility (Bullard et al. 2016).

1.2.2 Impact of high latitude dust on local, regional, and global dust cycles

The impact of HLDE is also unique as compared to the impact of dust emitted from low-latitude sources. The emission of particles directly into the pristine polar atmosphere has strong radiative effects, and it is important to examine HLDE for their impact on the radiative balance of the Northern atmosphere. Furthermore, the transport and deposition pathways of emitted particles differ from those of particulate matter emitted from lower latitudes, and the impact of HLD deposition on local and regional biogeochemical nutrients cycling is likely significant (Bullard 2017). In addition, deposition of dust can increase the albedo of snowpacks and ice, leading to faster rates of melting and changes to the hydrological cycle (Miller et al. 2016), and specifically, the potential for HLD deposition on glaciers and snowpacks is rather high, as many of the known HLDE sources are situated in proglacial regions with extensive snow and ice cover.

Initial studies on the transport and deposition of HLDE have already been performed. Bullard et al. (2016) have estimated that total HLDE constitute 80-100 Tg/year, or 5% of global dust emissions. The results of a modelling study by Zwaaftink et al. (2016) indicate that 3% of global dust emissions is sourced at Northern high-latitude sources; their study also found that Northern HLDE are the dominant source of dust deposition in the Arctic, with about 90% of total dust deposition in the Arctic originating from high-latitude sources.

Finally, while the majority of HLDE research to date has focused on emissions from Iceland, Greenland, and Antarctica, there have also been studies published that attempt to characterize HLDE in North America, specifically in Alaska, United States and Yukon, Canada. A study by Nickling published in 1978 evaluated the effects of shear velocity – a parameter related to the vertical force felt by particles on the surface of erodible soils – and soil moisture on dust emissions from the Ä'äy Chù (Nickling 1978). Zdanowicz et al. (2006) investigated the deposition of Asian dust in the St. Elias Mountain range, but did not analyze local dust sources. In addition, satellite imagery and meteorological data were used to monitor dust emissions from the Copper River, whose sediments consist primarily of glacial flour, and to observe the transport of Fe from this dust source to the Gulf of Alaska; the study found exceptionally high interannual variability in the quantity of dust emitted from this dust source, with the variation affected by the soil moisture, wind velocity, and hydrological cycling at the dust source (Schroth et al. 2017).

1.2.3 Challenges to high-latitude dust studies and the need for ground-based measurement at the source

The majority of the above-mentioned studies on HLDE have been performed using satellite data, which face significant challenges in observing high-latitude regions due to limited visibility caused by extensive cloud cover and long periods of darkness (Bullard et al. 2016). Ground measurements are able to overcome these obstacles as dust events can be sampled directly, avoiding the need for the use of remote sensing. Furthermore, collecting air samples directly in HLD sources allows for the more accurate and precise investigation of the meteorological factors associated with HLDE at a specific site, particularly in mountainous

Northern regions where the variation in meteorological conditions varies greatly from site-to-site.

1.3 Analysis of ambient concentrations and particle size distributions

In studies of mineral dust, it is crucial to measure ambient dust concentrations to gauge the frequency of dust events, to evaluate the impact of dust emissions on air quality, and to perform further analysis, such as correlation of dust events with certain meteorological conditions or calculation of the vertical aerosol flux from the source region. As the size range of mineral dust particles is quite large, spanning from several nanometers to hundreds of microns in diameter, it can be difficult to measure the concentration and size distribution of the total suspended particulate matter at a given site (Ryder et al. 2018). Our examination focuses primarily on mineral dust aerosols smaller than 10 μm in diameter, and thus the following techniques are those best suited for the study of these size ranges. Both gravimetric and particle sizing techniques have been used to monitor ambient aerosol concentrations. While these techniques do not necessarily discriminate between mineral dust and other atmospheric particles, the relatively coarse size range of mineral dust as well as its predominance within the site of dust emission make these techniques useful for the observation of ambient dust.

Ambient concentrations of mineral dust over a longer (typically 24 – 72 hr) time scale can be determined by performing gravimetric analysis of filter samples, typically of PM_{10} (McInnes et al. 1996). The low time-resolution of this method is offset by its cost efficiency and low instrument maintenance requirements. Furthermore, an advantage of this technique is that filters can be used to perform offline compositional analysis.

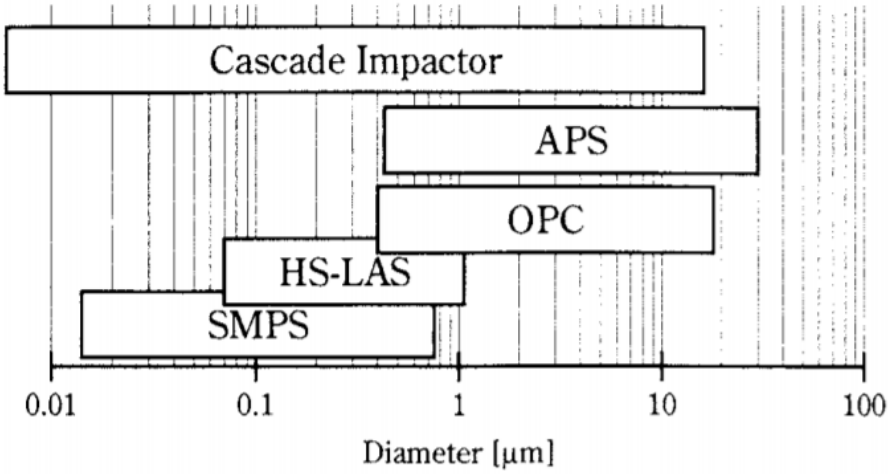

Figure 1-4. Detection range of various ambient aerosol particle sizing techniques applicable to the sizing of atmospheric particles 0.01 – 20 μm in diameter. The instruments included are a cascade impactor, aerodynamic particle sizer (APS), optical particle counter (OPC), high sensitivity – laser aerosol spectrometer (HS-LAS), and a scanning mobility particle sizer (SMPS). (Image Source: Friehmelt, R. et al., *KONA Powder and Particle Journal* **2000,** *18*, 183-193)

In addition, a wide array of particle sizers exists for monitoring both the size distribution and total ambient concentration of particles in the atmosphere; an overview of these instruments and their detection range is provided in Figure 1-4 (Friehmelt et al. 2000). Aerodynamic particle sizers (APS) and optical particle counters (OPC) both perform high time resolution measurements of the size-resolved number concentration of particles in the atmosphere. As these systems often require tubing to guide the particles to the instrument inlet, evaluation of the particle losses during transfer is necessary to evaluate the accuracy of the output size distribution; available software renders this calculation relatively simple if the setup characteristics are known (Von der Weiden et al. 2009). *In situ* measurements of particle size distribution can also be performed using a scanning mobility particle sizer (Formenti et al. 2011). As we have employed both an APS and OPC, our discussion of particle sizing will focus on these techniques

1.3.1 Optical Particle Counter (OPC)

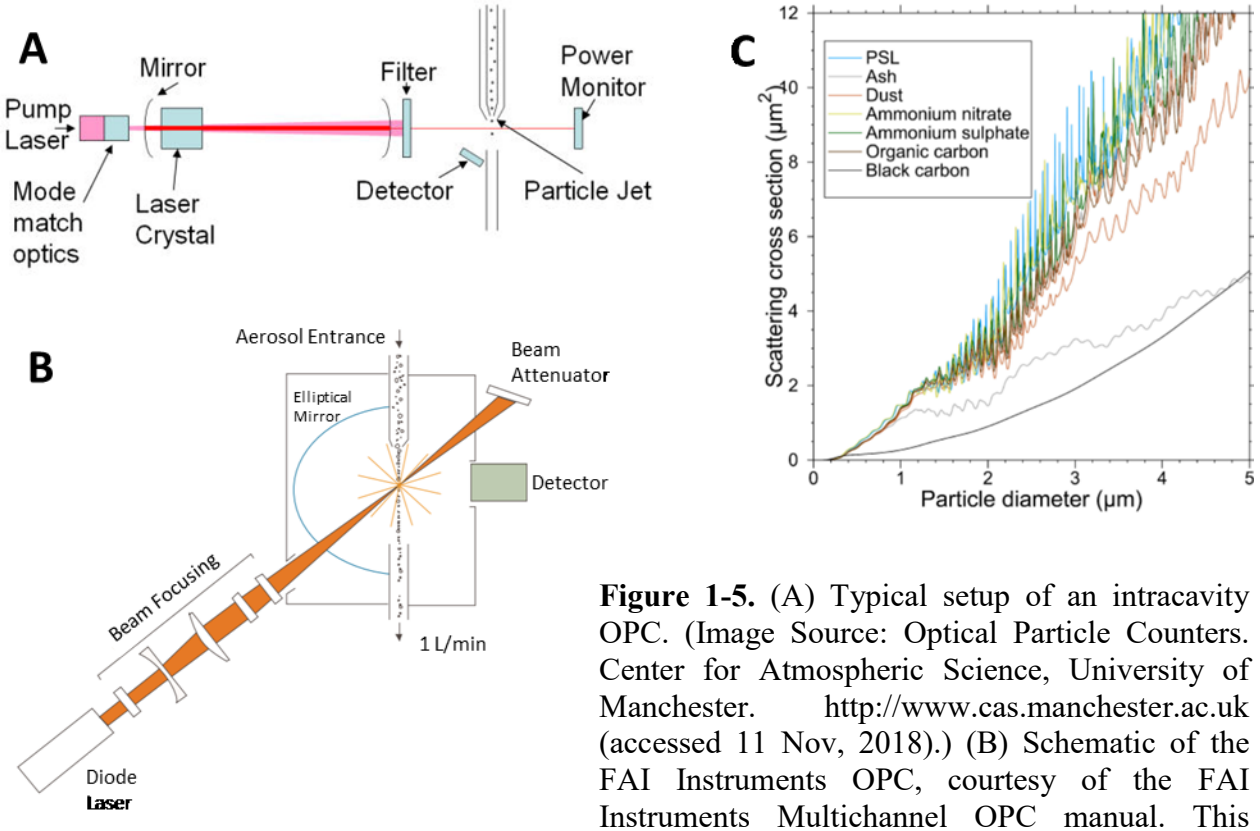

Figure 1-5. (A) Typical setup of an intracavity OPC. (Image Source: Optical Particle Counters. Center for Atmospheric Science, University of Manchester. http://www.cas.manchester.ac.uk (accessed 11 Nov, 2018).) (B) Schematic of the FAI Instruments OPC, courtesy of the FAI Instruments Multichannel OPC manual. This image has been altered from the original figure published in the OPC instrument manual – original Italian labels have been translated to English. (C) Mie theory-based relationship of light scattering to particle size for several materials. (Image Source: Rosenberg, P. D et al., *Atmos. Meas. Tech.* **2012,** *5* (5), 1147-1163.)

A common technique used for sizing atmospheric particles, an OPC calculates the diameter of a given particle from the intensity of light scattered by the particle analyzed. This calculation is based on Mie theory, and assumes sphericity of the particle and that its refractive index is known (Rosenberg et al. 2012). Because OPC size distributions are determined from the particles' optical properties, the measured output is known as the "optical diameter" to distinguish from particle sizing techniques that may rely on other physical properties of the analyzed particles.

The internal setup of an OPC is quite simple and can be found in Figure 1-5a. Ambient air is drawn through an inlet system designed to focus and dilute the aerosol stream to ensure particles will be analyzed one at a time. This stream then passes through a focused beam of

light – the most common OPC light source is a laser to maximize light intensity – which is scattered whenever a particle passes through the beam. A detector monitors the intensity of scattered light at a specific angle, and if the intensity is above a certain threshold value the instrument uses Mie theory to calculate the particle's diameter based on the measured light scattering intensity and using pre-determined assumptions of the refractive index of the particle (Hinds 2012).

There are certain limitations and sources of error in OPC particle size measurement. Firstly, there are several factors in addition to diameter that can influence a particle's ability to scatter light. Particle shape, inhomogeneity within the particle, or incorrect assumptions about its refractive index can introduce errors into the diameter calculated by the instrument (Rosenberg et al. 2012). For example, Osborne et al. found evidence that deviation of particle size from the assumed spherical shape can introduce up to 11% error to the calculated size (R. Osborne et al. 2008). Secondly, the Mie theory relationship between particle size and light scattering intensity loses sensitivity as particle size increases in the micron size range (Figure 1-5c). This is due to the complicated non-linear relationship between light scattering and particle diameter, as described by Mie theory. Thus, it becomes increasingly difficult for OPC instruments to distinguish between particles in the coarse fraction, and the size resolution decreases in the range of 1 to 10 μm in diameter as compared to the smaller size bins. The upper size limit of OPC particle sizing is typically 20 μm, and the optimal size range of study for these instruments is a diameter between 0.1 – 5 μm (Hinds 2012). Furthermore, care must be taken to ensure the air sampled by an OPC possesses a relatively low number concentration, in order to avoid coincidence errors in which two or more particles pass through the light source simultaneously (Hinds 2012).

Despite their shortcomings, OPCs are excellent tools for monitoring ambient particle concentrations. Their high time resolution allows for measurements to be taken as frequently as every second. This allows for detailed observation of changes in ambient aerosol concentrations over time, and in the case of observing HLDE, the output of an OPC can be analyzed to determine the frequency and intensity of dust production during a period of hours, days, weeks, or more. Thus, to summarize, OPCs are relatively inexpensive, robust, and easy

to deploy in the field, though care must be taken to ensure quality of the data output by these instruments.

Furthermore, it is noteworthy that modifications to the internal OPC setup can impact the accuracy and sensitivity of these instruments. According to the instrument manual, the FAI instrument employed in our study of mineral dust near Kluane Lake, YT employed an intracavity setup, in which the particle beam is passed directly through the unfiltered focused beam of the laser. The instrument's elliptical mirror is able to capture more light, allowing for increased sensitivity to smaller particles; it also collects light over a wide angle, decreasing potential errors in measurement due to variability in particle refractive index. A schematic of the FAI Instrument OPC used, obtained from the instrument manual, can be found in Figure 1-5b.

1.3.2 Aerodynamic Particle Sizer (APS)

Another technique for monitoring ambient particle size distribution is the APS, which determines the aerodynamic diameter of ambient particles. The aerodynamic diameter is defined as the diameter of a spherical particle with a density of 1 g/cm^3 whose terminal velocity is equivalent to the particle measured (DeCarlo et al. 2004). Aerodynamic diameter is useful to monitor from the perspective of aerosol behavior in the atmosphere, as it is indicative of the effective diameter of a particle in an air stream. Accurate in the range of 0.3 μm to 20 μm, these instruments can measure both the fine and coarse portions of ambient mineral dust with reasonable accuracy. However, as with the OPC, the APS is also prone to certain systemic errors that have been evaluated extensively in order to constrain this error.

An APS determines the diameter of ambient particulate matter using a time-of-flight system (Figure 1-6) (Mitchell 2014). Particles are focused into a narrow stream in a nozzle and are accelerated at a rate of 10^6 m/s^2. Due to the high rate of acceleration, particles larger than 0.3

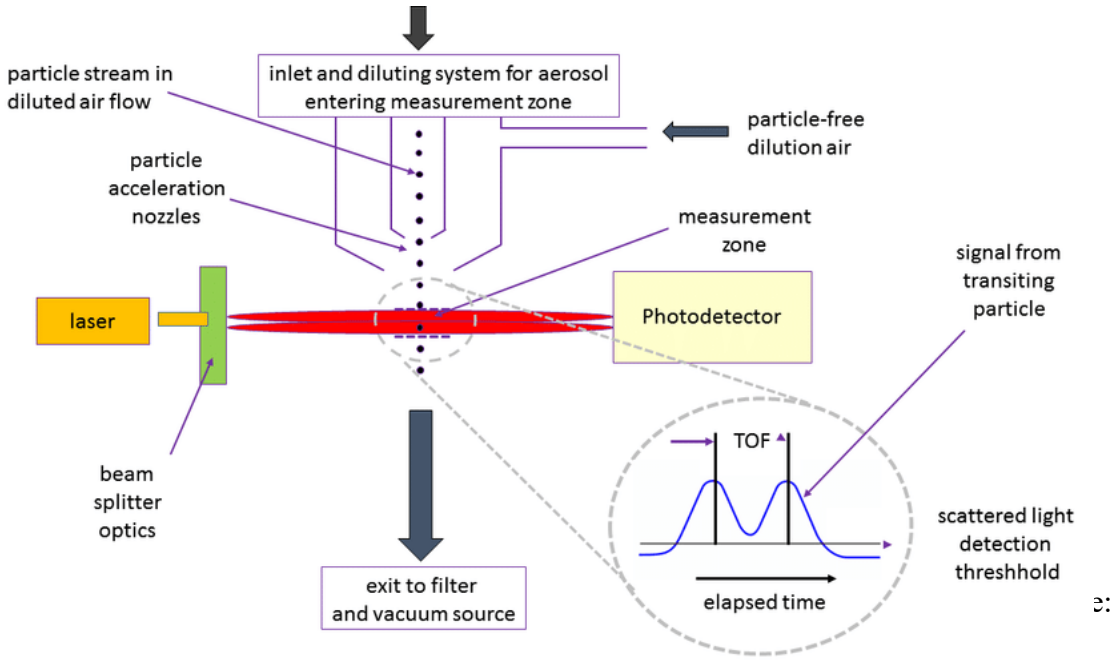

Figure 1-6. Instrument schematic of an aerodynamic particle sizer. (Image Source: Mitchell, J. *J. Aerosol Med. Pulm. Drug Deliv,* **2014**; Vol. 28.)

µm in diameter accelerate slowly relative to the air stream, and thus their velocities as they exit the acceleration zone are proportional to their aerodynamic diameter. After acceleration, the particle stream passes through the "timing region" of the instrument, which comprises two lasers placed 100 µm apart. As particles pass through the focused laser beams, they scatter the incoming light; the scattered light is detected as a pulse by the instrument, and the time between the first and second pulses produced by particles as they pass through the two consecutive lasers is related to the drag forces of the particle in the air stream. This information can then be used by the instrument to calculate the aerodynamic diameter (Hinds 2012).

Both the shape and density of particles can be sources of error in the APS determination of aerodynamic diameter (Hinds 2012). Non-spherical shape reduces the drag effects felt by particles and can lead to an underestimation of their corresponding aerodynamic diameter. Furthermore, deviations in particle density from that of calibration standard particles can also introduce error, as the particle density can also affect its drag time; particles with larger densities will have slower velocities and their sizes will be overestimated. This is more the case for mineral dust, whose density is typically 2.65 g/cm^3 (Lee et al. 2009). The overall effect of both density and shape characteristics on the APS measurement of mineral dust tends to result in a 10 – 30 % underestimation of aerodynamic particle diameter (Reid Jeffrey et al. 2008).

1.4 Elemental and mineralogical chemical composition

The chemical composition of mineral dust is related to its optical properties and environmental impact. The majority of techniques currently employed to characterize the composition of mineral dust provide a bulk analysis of either the mineralogy or element content. However, certain microscopy techniques allow for the analysis of individual particles, giving more detailed and size-resolved data on the dust composition. As the techniques available provide a wide range of sensitivity, cost-efficiency, and compositional data, the choice of technique limits the quantity and type of information able to be obtained. Thus, studies characterizing mineral dust commonly use at least two techniques, and often more, in order to provide a more comprehensive analysis of its chemical composition.

Bulk mineralogy can be determined using XRD, which allows for semi-quantitative determination of major mineral fractions (including the silica, iron oxide, and calcium oxide) present in a given sample. However, this technique requires upwards of 100 mg of sample mass which can be significant for those studying ambient mineral dust. The major element composition of mineral dust can be determined using XRF, PIXE, and INAA, while the minor and trace element content is often determined using ICP-AES, ICP-OES, ICP-AAS, and ICP-MS. Finally, there exist microanalysis techniques, such as SEM/EDS, able to probe the

mineralogical composition of individual particles; LA-ICP-MS may also be used to analyze both bulk samples and individual particles (Falkovich et al. 2001; Thevenon et al. 2009).

1.4.1 SEM/EDS

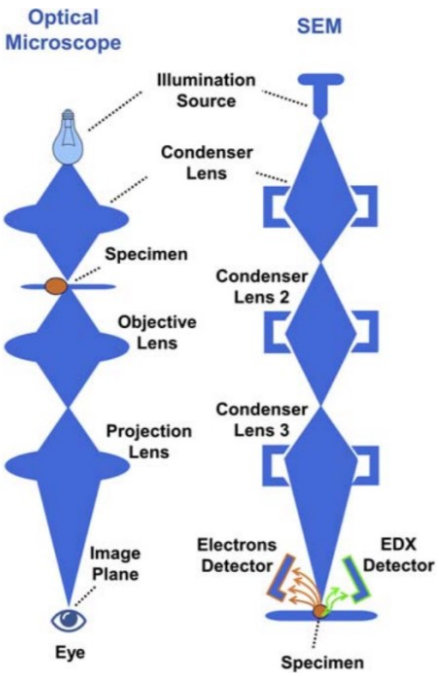

Figure 1-7. Instrument schematic of SEM/EDS, providing an overview of entire setup with comparison to optical microscopy for reference. (Image Source: Girão, A. et al., *Comp. Anal. Chem*. **2017**.)

Scanning electron microscopy (SEM), when coupled with energy dispersive x-ray spectroscopy (EDS), is a powerful tool for studying the morphology and composition of individual mineral dust particles. The instrument setup of an SEM/EDS system is shown in Figure 1-7. An electron beam is generated by an electron gun and is focused by magnetic fields (Atkins and De Paula 2009). When the incident electron beam hits the sample, the electrons in the beam are scattered, but may also interact with the electron shells of the individual atoms contained within the sample; this interaction is what allows the generation of both a microscopic image as well as compositional analysis (Atkins and De Paula 2009).

The microscopic image is typically generated by the detection of secondary electrons, which are weakly bound electrons emitted from the sample surface, or near the sample surface, with an energy corresponding to the conductivity of the atom from which they were displaced. Secondary electrons allow for the generation of images of the sample surface, provided it is a material with relatively high conductivity (Zhao); samples may be coated with a high-conductivity substance, such as Au, to increase their surface conductivity. Backscattered electron detection, which can also be used to generate an image, has the advantage that the energy of the backscattered electrons is proportional to the atomic number as larger atoms release more electrons, as larger atoms are

more effective scatters of the electron beam. In the resulting image areas of the sample with large atomic numbers are brighter (Girão et al. 2017).

In addition, the elemental and mineralogical composition of the sample can be determined using EDS analysis. The energy of the electron beam can excite and result in the ejection of electrons in the lower energy levels of the atom (Zhao). The resulting electron hole has a positive charge to which the electrons at higher energy levels are attracted; the x-ray radiation emitted when these electrons transition to a lower energy level is proportional to the atomic number of the atom, and thus detection of these x-rays allows the determination of the atomic number of the elements contained within the sample. From the elemental composition, the mineralogy can also be extracted either through analysis of element ratios or by comparison with reference spectra (Girão et al. 2017).

SEM/EDS has been used extensively to perform single-particle analysis of mineral dust mineralogy (Falkovich et al. 2001; Pachauri et al. 2013). EDS analysis of individual particles is considered semi-quantitative due to the effects of irregular particle shapes (Formenti et al. 2011; Pardess et al. 1992). In order to use unprocessed SEM/EDS to identify mineral class, the spectra obtained must be compared to known reference spectra. However, it is also possible to normalize the obtained spectra to a reference material, such as a polished Co standard reference material, in order to obtain quantitative elemental data (Falkovich et al. 2001). Moreover, the number of particles analyzed in more recent studies of mineral dust can range in the tens-of-thousands of particles, due to the advent of automated technologies (Formenti et al. 2011). While this technology has the advantage of an increased sample size, decreasing the uncertainty range of the resulting data, semi-quantitative mineralogical analysis can also be performed using manual operation and a sample size of hundreds of particles (Falkovich et al. 2001).

SEM images can also be used to examine particle shape, which may be relevant to the radiative properties of mineral dust (Pachauri et al. 2013). The aspect ratio of particles is an indicator of the overall sphericity of the sample collected. This is most commonly calculated by fitting an ellipsis to the shape of the particle analyzed and calculating the ratio between its major and minor axes (Formenti et al. 2011).

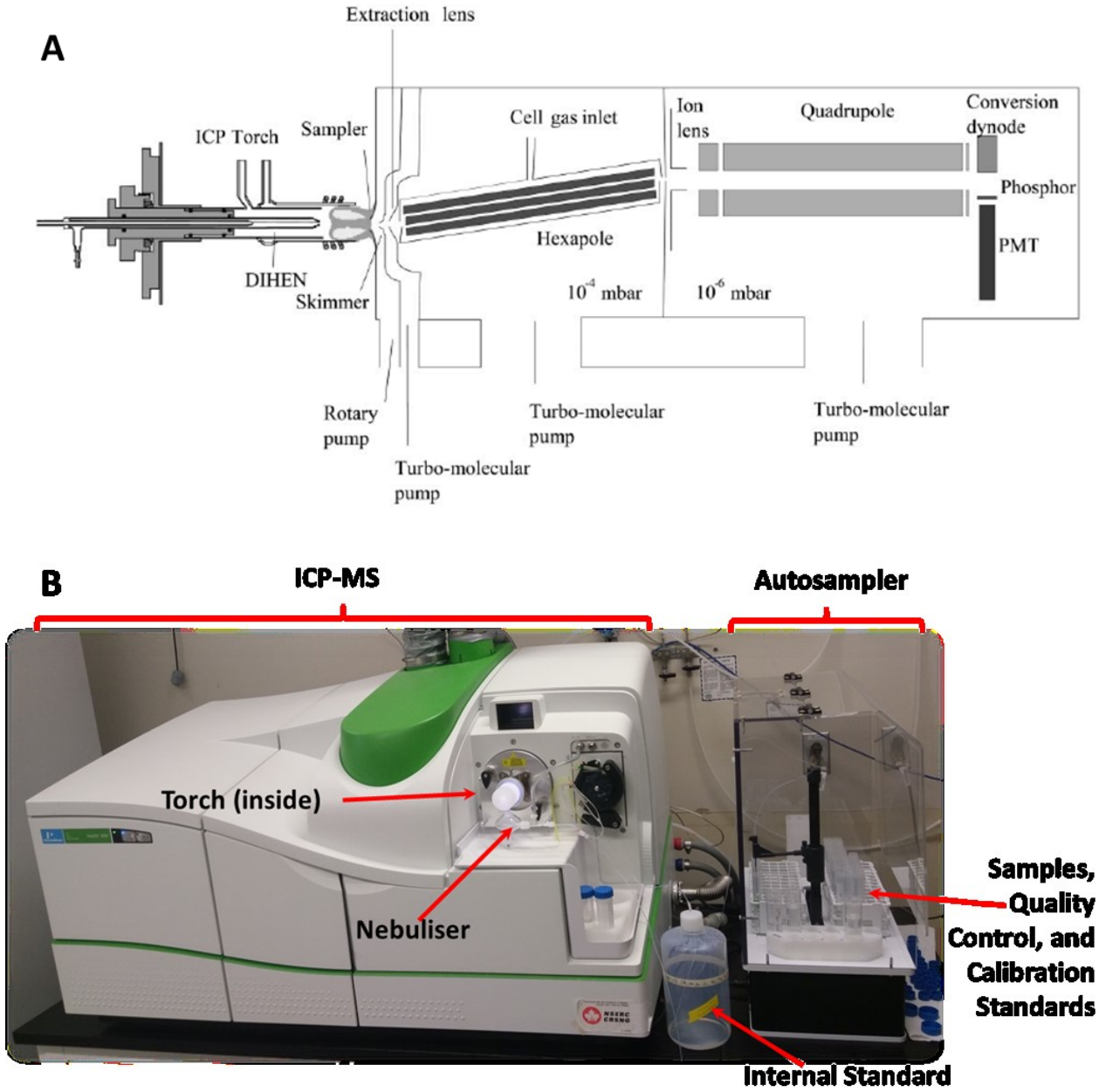

Figure 1-8. (A) Diagram of ICP-MS instrumentation. (Image Source: O'Brien, S. et al. 2003; *J. Anal. At. Spectrom.* Vol. 18.) (B) Setup of the quadrupole ICP-MS used in the current study, including the location of the samples, quality control (QC) and calibration solutions.

1.4.2 Solution-phase ICP-MS

Inductively coupled plasma – mass spectrometry (ICP-MS) is commonly used for quantitative analysis of the minor and trace element content of environmental samples. Applicable to the analysis of a variety of matrices, including seawater, oils, urine, hair, and sludge, ICP-MS can be used to obtain isotopic ratios, metal speciation, and total elemental content of a given sample. A diagram of a typical ICP-MS instrument setup is provided by Figure 1-8a, while the instrument used for analysis in this study can be found in Figure 1-8b (E. O'Brien et al. 2003).

Ions are generated in the inductively coupled plasma (ICP) torch, which consists of an induction coil located in the presence of Ar gas. The electromagnetic radiation given off by the induction coil ionizes the surrounding Ar gas. In the presence of an added spark, high energy electrons will collide with Ar atoms, resulting in an energy transfer that may, for a single Ar atom, displace an electron and form Ar^+, while also releasing an electron that may go on to ionize a further Ar atom. The result of this process is the generation of a plasma, whose temperatures typically reach 6000-8000 K. (Montaser 1998)

In solution-phase ICP-MS, samples are introduced into the ICP via a nebuliser, which converts the sample stream into a spray of small droplets. As these droplets pass through the ICP, the high temperature of the plasma evaporates all solvent, atomizes the sample, and ionizes the elements present. Typically, only positive ions are analyzed, as the plasma consists of positive ions which efficiently remove the electrons of the elements in the sample, though detection in negative ion mode is also possible. (Chtaib and Schmit 1988; Skoog et al. 2013)

As depicted in Figure 1-8a, ions are transferred from the ICP to the mass spectrometer using an interface consisting of two cones – a sampler and a skimmer – which serve as an interface for the transport of ions from the atmospheric-pressure ICP unit into the high vacuum of the mass spectrometer unit (generally operated at less than 10^{-6} torr) (Skoog et al. 2013). These cones possess an orifice approximately 1 mm in diameter and allow a representative portion of the ions generated in the ICP to enter the high-vacuum region of the mass spectrometer. The ions are then focused into an ion beam as they travel through the ion optics of the instrument, and are passed through a mass analyzer before detection (Skoog et al. 2013). Typically, ICP-

MS instruments are equipped with either a quadrupole or magnetic sector mass analyzer, depending on the sensitivity required by the analysis. Quadrupole ICP-MS instruments are widely used as they are relatively inexpensive compared to magnetic sector ICP-MS instruments and possess low limits of detection – often less than 1 ppb, (Skoog et al. 2013). However, magnetic sector ICP-MS instruments possess higher resolution and are preferable when high sensitivity elemental analysis is required, though operation at higher resolution does also lower the instrument sensitivity.

As the ICP-MS instrument is quite sensitive to the introduction of particulate matter, acid digestion of samples is commonly required prior to ICP-MS analysis. The goal of the digestion is the extraction of all elements to be analyzed from the particle phase so as to avoid injecting solid matter into the instrument, which can cause blockages in the nebulizer (Falciani et al. 2000). A variety of acid mixtures can be used to digest samples, including HNO_3 only, HNO_3/HCl, HF/HNO_3, or HNO_3/HCl/H_2O_2 (GÜVEN and Akinci 2011). HNO_3/HCl is commonly used as it effectively extracts a wide range of metals, while the addition of HCl can stabilize certain elements such as Fe to increase the analytical reproducibility and quantitation of these metals (Engelbrecht et al. 2009; EPA 2007). A mixture of HF/HNO_3 is necessary to perform total digestion of sediment samples, as the presence of HF is necessary to break apart the aluminosilicate matrix. However, this procedure renders quantitative analysis of Si content in the sample impossible, as Si reacts with HF during the processes of digestion to produce the gaseous product SiF4; moreover, this procedure involves the use of dangerous acids that can also harm the ICP-MS instrument (Falciani et al. 2000; Gaudino et al. 2007; Pekney and Davidson 2005).

The U.S. EPA provides certified methods that detail the necessary precautions, quality control tests, sample preparation, and analysis procedures required to perform an accurate, quantitative digestion of sediments. The protocol used in our analyses is a modified version of Method 3051a, which details the use of a HNO_3/HCl mixture in the microwave digestion of sediments (EPA 2007). While this procedure does not completely digest the aluminosilicate matrix, metals are extracted by the concentrated acid mixture to an acceptable degree for quantitation. The advantages of solution phase ICP-MS are vast, as this is a very robust and

sensitive technique that has been completely verified by both academic and government publications.

However, there are several sources of error that must be considered when performing ICP-MS analysis. Typically, quadrupole ICP-MS instruments do not possess enough resolution to distinguish between certain analyte and interfering species within one m/z value of one another. Thus, interference species generated during ionization within the instrument plasma, including polyatomic, doubly charged, and isobaric interferences, can greatly decrease measurement accuracy and sensitivity. Elements such as arsenic, cadmium, manganese, and nickel may possess multiple interference species (May and Wiedmeyer 1998). These sources of interference can lead to errors in either the calibration curve, sample analysis, or both, decreasing the accuracy of the measurement technique. As a result, the inductively coupled plasma must first be optimized before use of the instrument to ensure ionization is occurring efficiently and with minimal generation of polyatomic or doubly charged species. Furthermore, because there are multiple sources of interference, error, and contamination in ICP-MS analysis of geological samples, quality control must be performed during each analysis to ensure quantitative data is collected.

In addition, steps can be taken when performing quadrupole ICP-MS to minimize interferences and increase instrument sensitivity. Passing the ion beam through a collision cell, in which a colliding gas may break apart polyatomic interfering species, allows for removal of these interferences via mass discrimination (Perkin-Elmer 2001). In addition, spectral interference can be minimized using mathematical corrections applied to the analyte calibration curve (Heithmar et al. 1990). In a similar vein, isobaric interferences may be reduced or eliminated through the application of correction equations to recalculate the analyte signal intensity (Nardi et al. 2009) – for example, this is commonly performed in the analysis of ^{75}As, as $^{35}Cl^{40}Ar$ is a major interfering species that is difficult to eliminate. Matrix interferences can also be reduced through the use of an internal standard (Heithmar et al. 1990).

Finally, the choice of isotope when performing ICP-MS can also help minimize interference, as certain isotopes may possess less interfering species than others (Nardi et al. 2009). In this work, nine elements were analyzed using solution phase ICP-MS. The isotopes chosen were as follows: ^{55}Mn, ^{57}Fe, ^{59}Co, ^{60}Ni, ^{63}Cu, ^{75}As, ^{111}Cd, ^{133}Cs, and ^{208}Pb (Gaudino et al. 2007).

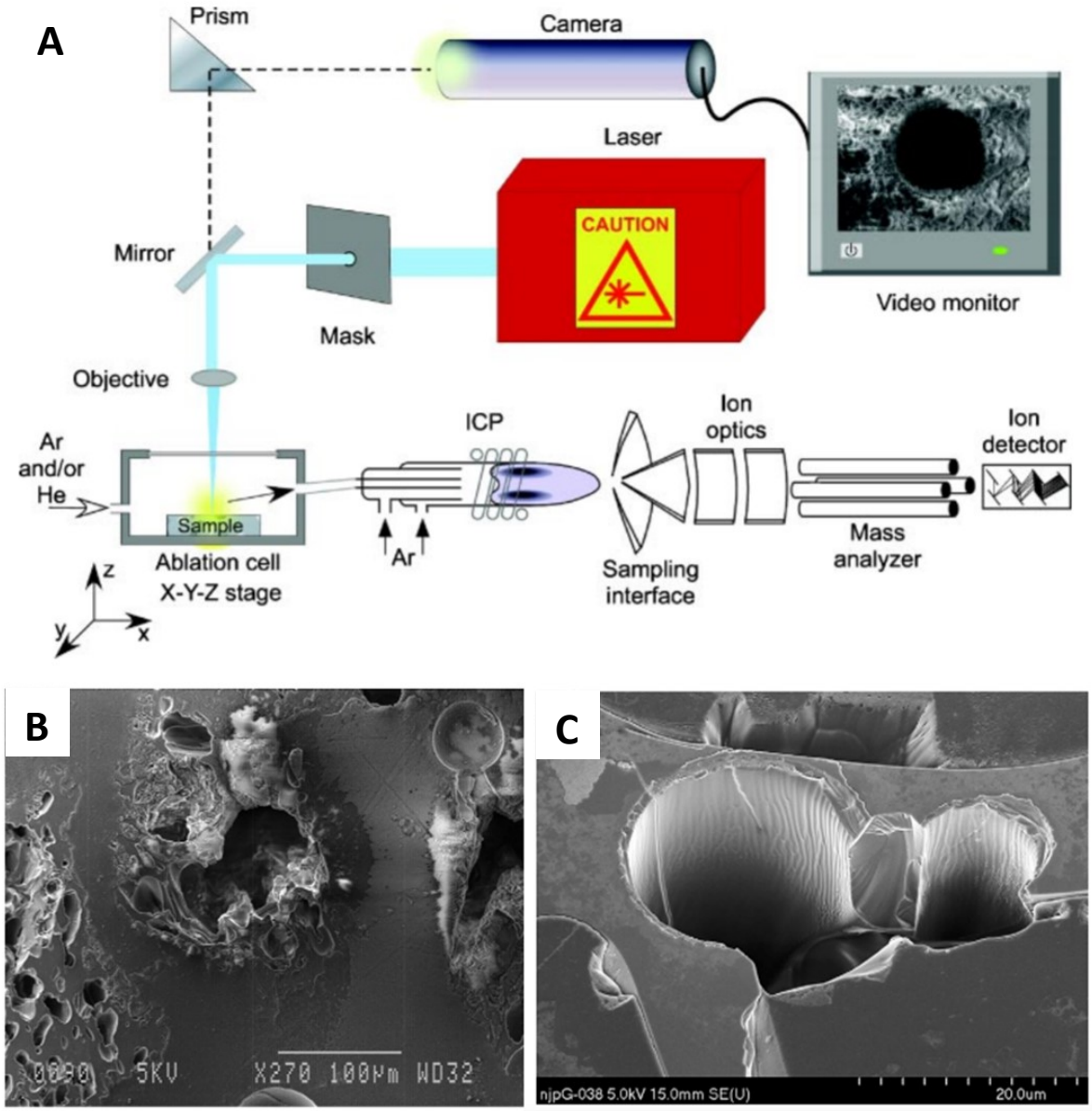

Figure 1-9. (A) Schematic for sample analysis using laser ablation ICP-MS (Image Source: Resano, M., García-Ruiz, E., Vanhaecke, F. (2010). Laser ablation-inductively coupled plasma mass spectrometry in archaeometric research. Mass Spectrometry Reviews 29:55-78.) (B and C) SEM images of ablation craters produced by (B) 266 nm and (C) 193 nm laser beams (Image Source: Pearce, N. J. G. et al. *Quaternary International* **2011**, 246 (1), 57-81.).

1.4.3 Laser Ablation ICP-MS

As solution phase ICP-MS involves time-intensive sample preparation, costly reagents, and produces a large volume of waste, there is an incentive to search for alternative methods of analysis. Laser ablation ICP-MS (LA-ICP-MS) attempts to fill this need by incorporating a high-energy laser beam whose ablation of the sample generates the aerosols analyzed by the ICP-MS, thus eliminating the need for acid digestion of samples and the generation of solution waste. However, LA-ICP-MS analysis poses significant challenges to the analysis of environmental samples, due to its sensitivity to matrix effects. Furthermore, as it is a more recently developed technique, the robust and consistent protocols for analysis that accompany solution phase ICP-MS have yet to be produced.

A schematic of LA-ICP-MS is provided in Figure 1-10a (Resano et al. 2010). Laser ablation occurs in a separate chamber, in which a focused laser beam is fired at the surface of the sample to produce a laser-induced plasma that generates vapors and fine aerosols that are transported to the ICP-MS. Mineral dust samples are typically mounted in an epoxy resin or on a piece of tape in order to analyze the composition of individual particles, though homogenization techniques such as grinding followed by pelleterization can also be used (Limbeck et al. 2015; Pearce et al. 2014). There are many factors that influence the performance of LA-ICP-MS, including the laser energy, beam width, ablation time, and carrier gas setup (Pearce et al. 2011).

The primary source of error in LA-ICP-MS analysis is elemental fractionation, which results in the nonstoichiometric analysis of the elements contained within a sample (Limbeck et al. 2015). This phenomenon stems from differences in elemental volatility, as incomplete vaporization of particles within the laser-induced plasma or the ICP may result in preferential analysis of more volatile elements. Deposition of vapors on instrument tubing can further exacerbate fractionation. It is important to note that elemental fractionation can limit the use of non-matrix-matched calibration standards in LA-ICP-MS analysis, as the degree to which elemental fractionation can occur depends on the sample matrix. Elemental fractionation has been extensively documented; for example, Kuhn and Gunther (2003) found that LA-ICP-MS

analysis of brass samples using a 266 nm Nd:YAG laser, the system used by our work as well, gave higher Cu/Zn values as compared to certified reference values. Furthermore, the radiation-absorbing properties of different materials are not consistent, resulting in varying amounts of material that may be liberated during a set period of ablation (Becker and Tenzler 2001). Thus, certain steps are necessary to ensure that elemental fractionation has not significantly affected the analysis. This can include analysis of a matrix-matched certified reference material, or comparison of the composition determined using LA-ICP-MS with that determined using solution phase ICP-MS.

Several steps may be taken to improve the sensitivity of LA-ICP-MS analysis and to minimize the influence of matrix effects and elemental fractionation. The use of an internal standard, often Si, is commonly recommended in the analysis of geological samples as it is naturally occurring within the sample and can be either quantified using another technique or estimated using knowledge of the sample mineralogy; the use of this internal standard should balance out the errors introduced by matrix effects (Liu et al. 2013). However, there may still be an error present in the analysis of elements that are not ionized and analyzed according to the stoichiometric ratios of their abundance in the sample (that is, if elemental fractionation has occurred). The use of matrix-matched calibration standards may eliminate the effects of elemental fractionation, as similar matrices should experience similar degrees of fractionation (Günther and Heinrich 1999). However, there is limited availability of calibration standards suitable for LA-ICP-MS analysis, and so this approach may not be feasible depending on the sample. Thus, an effective way of decreasing the impact of elemental fractionation on sample analysis is the transition to higher energy laser ablation systems. When first developed, LA-ICP-MS employed 1063 nm infrared lasers; however, it was later found systems that employ 266 nm, or even 193 nm, laser systems minimize elemental fractionation in the laser-induced plasma and allow for the generation of smaller particles that are more completely ionized within the ICP (Liu et al. 2013).

The use of LA-ICP-MS as a microanalysis technique to analyze individual particles faces significant challenges, one reason being that the effects of elemental fractionation increase as the size of the ablation crater decreases. Pearce et al. (2011) found that the use of a 193 nm ArF laser was preferable to the use of a 266 nm Nd:YAG laser in the microanalysis of tephra –

particles of rocks emitted into the atmosphere as a result of volcanic activity – with limits of detection improved by an order of magnitude for certain elements, such as yttrium. The difference in the quality of the ablation craters generated using both 266 nm and 193 nm laser wavelengths can be found in Figures 1-10b and 1-10c respectively, with increased melting of the sample matrix evident in Figure 1-10b. The study further demonstrated that the use of a magnetic sector mass analyzer, as compared to a quadrupole system, can improve sensitivity by 2 to 5 times. However, because the amount of sample ablated during microanalysis is quite low, low-resolution mode was found to be preferable when using a magnetic sector mass analyzer to maximize the signal intensity measured by the instrument.

1.4.4 Single particle ICP-MS

Single particle ICP-MS (SP-ICP-MS) is a powerful technique that has previously been used to measure engineered nanoparticles with extremely low detection limits. An important application of SP-ICP-MS is the detection of engineered nanoparticles in environmental samples, such as from snow or lake water, as this technique is highly sensitive and able to achieve the low detection limits required for analysis of environmental samples (Mitrano et al. 2012). The key component of the technique is the use of single-particle detection mode, in which one element is monitored at a very fast rate, with dwell times in the microsecond range. A solution of nanoparticles suspended in solution is introduced into the ICP-MS. Individual nanoparticles are ionized completely in the ICP, and when these ions pass through the mass analyzer and are detected, they produce a spike in the signal. SP-ICP-MS is also able to perform particle sizing, based on the signal intensity from the analysis of individual nanoparticles. A part of this study explored the feasibility of SP-ICP-MS to accurately size particles in the micron size range, much larger than is typical for the application of this technique (Fréchette-Viens et al. 2017).

1.5 Our approach

In this study, we hope to complete a thorough characterization of key physical and chemical characteristics of the mineral dust emitted from the Ä'äy Chù Valley in Yukon, Canada. This includes an analysis of the ambient concentration and particle size distribution of particles emitted from this dust source as well as the measurement of ambient dust concentrations at locations near the source, in order to evaluate the size and direction of the dust plume and the spatial and temporal variation in the dust emitted from this location. As a result, we have chosen to employ OPC, APS, and gravimetric analysis for determining particle size distributions and ambient mass concentration. We also hope to gain insight into the impact of the emitted dust on local air quality, and have thus also compared the results of our analysis of ambient mass concentration with the air quality guidelines of the WHO.

In addition, the particle morphology and mineralogy are crucial to the physico-chemical characterization of the dust emitted from this site, as these can have implications for the optical properties of the emitted dust (which may in turn shed light on the potential impact of these dust emissions on the radiative balance of the atmosphere both locally and regionally). These data may also allow more information to be gained concerning the dust emission mechanisms that take place at the Ä'äy Chù Valley (i.e., whether clay coatings are present on soil or dust particles). We have employed SEM imaging to analyse the mineralogical composition and the morphology of dust particles collected from this site, as well as to evaluate whether clay coatings were present on soil particles sampled from the dust source.

An equally important goal in our characterization of dust emissions from the Ä'äy Chù Valley is the analysis of the trace element content of dust emitted from this site, as this provides insight into the potential health hazard and nutritive content of the dust; it also sheds light on whether the composition of the dust changes spatially or temporally, and provides a point of comparison for PM_{10}, dust deposition, and soils collected from the dust source. We have chosen to perform a detailed characterization of nine elements (Mn, Fe, Co, Ni, Cu, As, Cd, Cs, Pb) in the ambient PM_{10} collected at and near the dust source, in dust deposition, and in both the bulk and fine fraction (diameters of 53 μm or less) of select soil samples. Analysis of the chemical composition of these samples was performed using ICP-MS. Attempts to use

LA-ICP-MS as a microanalysis technique were ultimately unsuccessful, though the resulting data is included in this document to demonstrate the method used and results that were obtained (Chapter 3). Similarly, the results of our unsuccessful attempts to evaluate the use of SP-ICP-MS in sizing particles as large as 1 μm, in order to determine whether the technique could be used for the analysis of mineral dust particles, are also included in Chapter 3.

The final goal of this work is to synthesize the information gained from the particle sizing, morphology, mineralogy, and elemental composition analyses of the PM_{10} emitted from the dust source, as well as the analysis of morphology and elemental composition of dust deposition and both fine and bulk soil fractions, to draw conclusions about the mechanism and impact of the dust emitted from the Ä'äy Chù Valley. We have used the measured mass concentrations and our meteorological data at the dust source to calculate the vertical flux of particles from the source into the atmosphere, and relate factors such as wind speed, shear velocity, saltation, and soil moisture to the dust emissions observed at this site. Moreover, we have used the results of our elemental composition analysis as a chemical signature to compare the emitted dust with the source soils, in order to gain insight into the mechanism of dust emissions that dominate in the valley. In this way, we employ the results of the wide range of analyses we have performed to draw important conclusions describing the emission of dust from the Ä'äy Chù Valley.

Chapter 2 – Article

Chemical and microphysical properties of wind-blown dust near an actively retreating glacier in Yukon, Canada

Jill Bachelder[1], Marie Cadieux[2], Carolyn Liu-Kang[1], Pérrine Lambert[1], Alexane Filoche[1], Juliana Galhardi[1], Madjid Hadioui[1], Amélie Chaput[2], Marie-Pierre Bastien-Thibault[2], Kevin J. Wilkinson[1], James King[2], and Patrick L. Hayes[1]

Departments of Chemistry[1] and Geography[2], Université de Montréal, Montréal, Canada

Submitted to *Aerosol Science and Technology*.

2.1 Preface

The following is the text of a manuscript submitted to the journal *Aerosol Science and Technology.* As the first author, I wrote the body of the text and created all figures and tables. I also made corrections to both the text and the graphics in response to comments from the article's co-authors. I participated in both the 2017 and 2018 dust measurement campaigns whose data are presented in this body, and was highly instrumental in the collection of air samples and setting up the sampling instruments. Supervised by my professor, Dr. Patrick L. Hayes, I completed all OPC data analysis, as well as the gravimetric analysis and ICP-MS analysis. In addition, I also performed the calculations relevant to the dust emission mechanisms, including determination of the vertical aerosol flux and the size-resolved threshold velocity. While I did not perform the SEM/EDS analysis myself – that was performed by Pérrine Lambert, during her internship in the Hayes group in the summer of 2018 – I did help guide Pérrine in her work and I performed the subsequent data analysis that allowed us to determine the mineralogy of the particles Pérrine had analyzed.

2.2 Abstract

Airborne mineral aerosols emitted in high-latitude regions can impact radiative forcing, biogeochemical cycling of metals, and local air quality. The impact of dust emissions in these regions on the atmosphere and environment may change rapidly, as warming temperatures can increase mineral dust production and source regions. As there exists little research on mineral

dust emissions in high-latitude regions, we have performed the first study of the physico-chemical properties of mineral dust emitted from a sub-Arctic proglacial dust source. Soil and aerosol samples (PM_{10} and deposited mineral dust) were collected in May 2018 near the Ä'äy Chù (Slims River), a site that has exhibited strong dust emissions. WHO air quality thresholds were exceeded at several receptor sites near the dust source, indicating a negative impact on local air quality. Notably, temporally averaged particle size distributions of PM_{10} were very fine as compared to those measured at more well-characterized, low-latitude dust sources. Mineralogy of ambient PM_{10} comprised primarily clay mineral aggregates, while PM_{10} elemental composition was enriched in trace elements as compared to dust deposition, bulk soil samples, and the fine soil fractions ($d < 53$ μm). Finally, through comparison of the elemental composition PM_{10}, dust deposition, and both fine and bulk soil fractions, as well as meteorological factors measured during our sampling campaign, we propose that the primary mechanisms for dust emissions from the Ä'äy Chù Valley are the rupture of clay coatings on particles and/or the release of resident fine particulate matter.

2.3 Introduction

Mineral dust plays an important role in many atmospheric and environmental processes (Formenti et al. 2003), as it can interact with atmospheric radiation both directly, by scattering and absorbing radiation, and indirectly, by acting as cloud condensation nuclei or ice nuclei (Huang et al. 2006; Lohmann and Diehl 2006; Sokolik and Toon 1996). Furthermore, mineral dust influences the biogeochemical cycling of metals by transporting nutrients to marine and terrestrial environments. It can also take part in heterogeneous chemical reactions that can alter the composition of the atmosphere, and can negatively impact air quality and public health (Avila et al. 1998; Phalen et al. 1991; Prospero 1999b; Usher et al. 2002).

The size distribution, morphology, and chemical composition of mineral dust ultimately determine the impact it will have on the atmosphere and environment (Formenti et al. 2011). Particle size is inversely proportional to atmospheric lifetime, as larger particles are more prone to deposition due to their larger mass, with particles equal to or less than 10 μm in diameter (PM_{10}) better able to undergo long-range transport in the atmosphere (Prospero 1999c). In addition, PM_{10} can have deleterious effects on air quality and public health, as

inhalation of particles in this size fraction can negatively affect lungs and cardiac health (Kappos et al. 2004). The shape of mineral dust particles is highly variable and rarely spherical, and this non-sphericity can influence its optical properties (Kalashnikova and Sokolik 2004; Mishchenko et al. 1999). Chemical composition is another important factor to consider, as the optical properties of the dust are related to its mineralogy while the elemental composition of dust can indicate how it will impact local biogeochemical cycling of minerals (Atkinson et al. 2013; Dubovik et al. 2002; Haywood and Boucher 2000; Richon et al. 2018).

Mineral dust emissions from high-latitude regions, defined as north of 50°N and south of 40°S, has recently been identified as an important yet overlooked area of research (Bullard et al. 2016). This is because the emission of dust at high latitudes has a unique effect locally as compared to in lower latitude regions. First of all, the radiative effects of the additional particulate matter are more pronounced in the pristine air and shallow atmospheric boundary layer of these regions (Barrie 1986). In addition, the proportion of mineral deposition within high latitudes has been shown to be 90% from the dust emitted from high latitude regions, and thus likely plays a much larger role in provision of minerals to local ecosystems as compared to dust transported from mid-latitude sources (Groot Zwaaftink et al. 2016). Deposition of mineral dust onto snow and ice can decrease the albedo of snow and ice surfaces, increasing the energy-absorbing capacity of these surfaces; this can, in turn, lead to increased rates of glacier ablation and earlier melting of snow during the spring season (Miller et al. 2016; Qian et al. 2015).

Moreover, there are significant differences in the dust production in high-latitude regions as compared to at lower latitudes. Glacier activity results in the production of fine glacial flour sediment, which can be transported and deposited via meltwaters; when dried, these fine particles are susceptible to wind erosion (Bullard et al. 2016; Crusius et al. 2011). Katabatic winds differ from wind systems that lead to the production of wind-blown dust in dry, arid regions in their frequency – this is because they are decoupled from the synoptic meteorology, as they are the result of radiatively driven gradients originating from the cold, dense air masses above high-elevation glaciers and mountains (and, thus, are more diurnally relevant). The strong katabatic winds originating from glaciers and surrounding mountains can then drive high winds that emit mineral dust particulate matter from the fine glacial flour sediments. In

addition, the rapid warming of Arctic and sub-Arctic regions can induce topographical changes resulting from glacier ablation. These changes may potentially lead to the creation of new dust sources, such as through the exposure of erodible sediment as a result of glacier retreat; they may also alter the emissions of existing sources, such as through changes to the local hydrology which can impact soil moisture, and subsequently soil erodibility (Bullard et al. 2016).

However, despite its significance, there are very few scientific studies that characterize the composition and microphysical properties of mineral dust based on ground samples collected from aerosols emitted from high-latitude regions. Sampling dust directly from any dust source is difficult, as source locations are often remote and the high concentrations of ambient dust coupled with the harsh environment can lead to instrument damage (Formenti et al. 2011). Remote sensing can be used to observe dust emission events (Crusius et al. 2011), but the effectiveness of this technique is limited when studying Arctic and sub-Arctic regions due to the fact that dust events often occur during periods of limited visibility, such as cloudy days or during the night, and these events are thus not easily observed via satellite imagery.

We have chosen to sample dust from the Ä'äy Chù (Slims River) Valley in the Kluane Lake region of Yukon, Canada. The erodible soils of the Ä'äy Chù River Delta comprise primarily glacial flour, and dust storms are regularly observed during the spring and summer (Nickling 1978). Cold air drainage occurs from the substantial glacier mass of the Kaskawulsh and the surrounding St. Elias mountain range, while smaller surrounding steep valleys also play a role in providing drainage to prolong and intensify katabatic winds. These strong winds, coupled with the presence of highly erodible sediment, result in frequent and intense dust emissions from this site. In addition, the Ä'äy Chù Valley has been directly impacted by climate change, with the rapid retreat of the Kaskawulsh glacier recently routing waters away from the river valley (Shugar et al. 2017), leaving the riverbed exposed over the summer season and thus potentially increasing its dust-producing erodible surface area. This location is significant as it may also serve as a point of reference for other proglacial dust sources at high latitudes.

Ours is the first study to characterize the chemical and microphysical properties of dust emissions from a source in the Canadian North. We provide results on several characteristics of the PM_{10} mineral dust collected, including its concentration, chemical composition,

morphology, and particle size distribution. We have also analyzed the chemical composition of dust deposited throughout the lower proglacial valley and soil samples collected from the exposed sediment of the river to understand variations in composition from emission to deposition, including during transport.

Lastly, we provide detailed information on the methods used to perform air sampling and meteorological monitoring directly at a high-latitude dust emissions source. The low-cost, efficient methods we have developed are tailored to the limitations of a remote location, as well as the harsh conditions of high-latitude dust sources; indeed, our reported sampling setup and instrumentation was successfully used to record weather data, perform air sampling and characterize particle size distributions without a nearby power source, functioning even during high dust concentration periods. The methods we have employed may be used by future researchers interested in conducting similar studies of high-latitude dust emissions directly at the source, in order to increase our understanding of the mechanisms involved in dust production at remote high-latitude sources.

Figure 2-1. Photos taken at the Island dust monitoring station at (left) 17:10 and (right) 18:10 PST during a dust event that occurred July 2, 2017.

2.4 Experimental

2.4.1 Field Site

The Ä'äy Chù river delta is 25 km from the 7 km-wide Kaskawulsh Glacier, in a 1 km-deep and 8 km-wide valley; the average slope of the valley is only 1:200. Examples of photos depicting dust emissions from the exposed river sediment can be found in Figure 2-1. Data collection was performed at this location from May 4 to June 2, 2018, as photographic images taken by automatic cameras in 2016 and 2017 indicated that the late spring/early summer is a period during which substantial dust production occurs. This is due to local geographical factors, as it is during this period that the snow has melted and the ground has thawed, but it is not yet so warm that glacier and snow-melt has flowed into the valley and moistened or covered the soils, decreasing their erodibility.

The sites at which atmospheric measurements were taken are shown in Figure 2-2a, while the locations of soil samples can be found in the Supplemental Information section (Figure 2-S1). The overall objective of the sampling scheme was to collect samples in the river delta, where significant dust emissions were observed, and monitor how the chemical composition changed as the dust plume travelled towards Kluane Lake. Strong winds originating from the glacier and the surrounding mountain ranges often blow down the valley towards Kluane Lake; thus, the sampling scheme was created based on the observation that dust often travelled from the river delta towards the lake, as shown by satellite imagery in Figure 2-2b, though there were times when the reverse did occur.

Details regarding the instrumentation, elevation, and GPS coordinates of the various sites sampled are given in Table 2-1. A main instrumentational site, the Down Valley site was installed in the Ä'äy Chù Valley within the dust source region, as frequent dust storms were produced from the surrounding soils. Its primary function was aerosol sampling and to serve as an extensively equipped meteorology station.

A mobile air sampling station was moved between three sites: the Ä'äy Chù East site (May 4 to 14), the Visitor's Center (May 15 to 28), and the Island site (May 29 to 31). The mobile station sampling locations are depicted in Figure 2-2a. Broadly, the goal of sampling at these

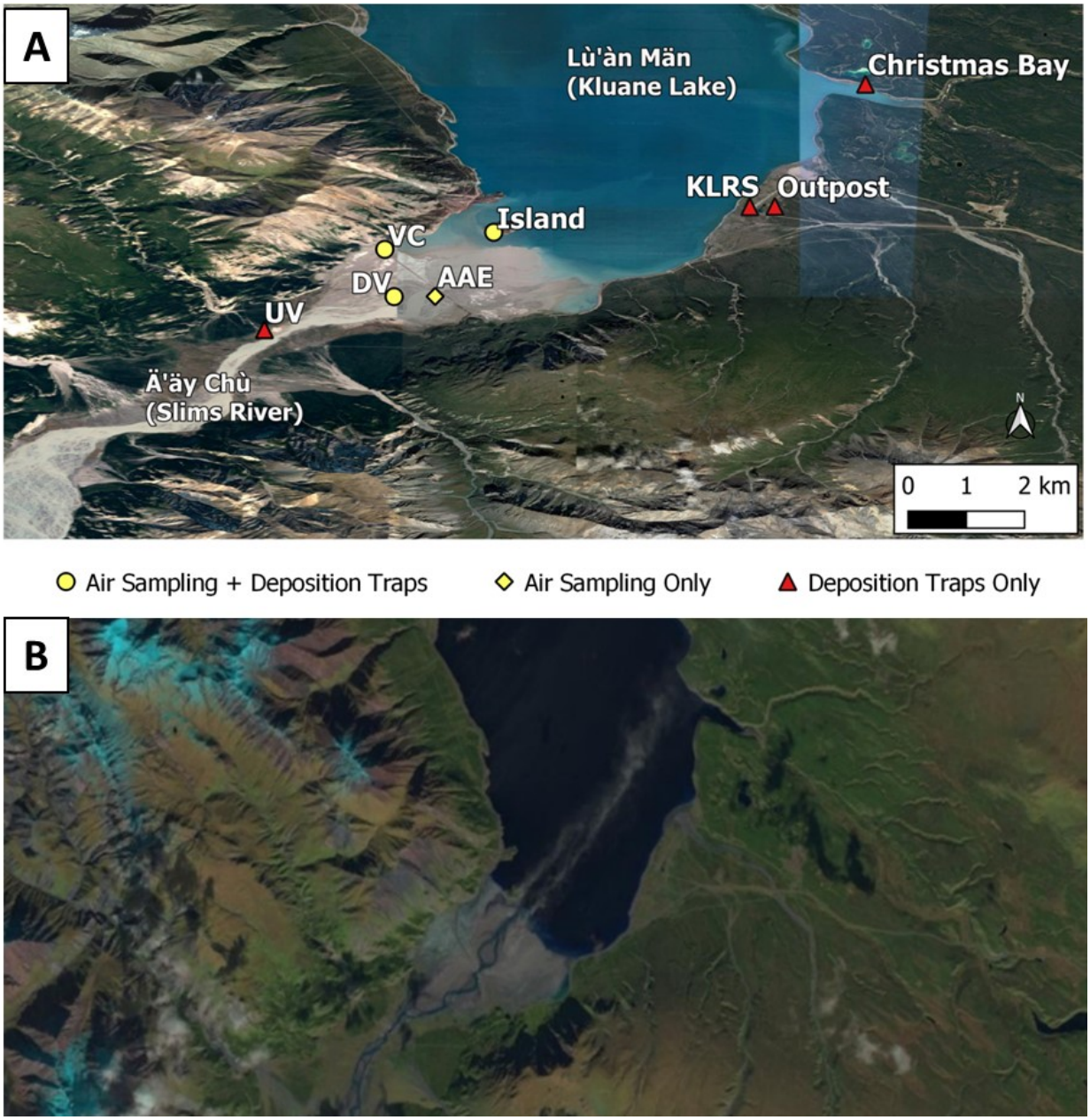

Figure 2-2. (A) Map of air sampling locations; site details provided in Table 2-1. (B) Satellite image of dust plume rising from the delta of the Ä'äy Chù (Slims River).

transient sites was to inform the spatial variation in the concentration and chemical composition of PM_{10} mineral dust within and near the valley, and to gain a sense of local air quality. One of the sites at which mobile ambient PM_{10} measurements were collected was the Kluane National Park and Reserve Thachäl Dhäl Visitor's Center, which serves as main tourist attraction and is managed by local employees during the spring and summer. Similarly, the

Island site is a scenic overlook adjacent to Kluane Lake; it is now a destination for tourists and local hikers, as the diversion of the Ä'äy Chù has rendered the island accessible by foot. The Island Site receives large amounts of mineral dust from plumes travelling down the Ä'äy Chù Valley.

Additionally, four sites solely monitoring dust deposition were placed as indicated in Figure 2-2a. This included three sites on the side of Kluane Lake opposite the dust source: the Kluane Lake Research Station, the Outpost Research Station, and the Shakat Tun Wilderness Camp in Christmas Bay. An Upper Valley site was also installed in the river valley, located 2 km closer to the Kaskawulsh glacier than the Down Valley site. The locations of these sites were selected to evaluate the spatial variation in the chemical composition of dust deposited in the lake region.

	Site Name (Abbreviation)	Sampling Equipment	Sampling Date	GPS Location (Latitude, Longitude)	Elevation (m)	Brief Description
Air Sampling	Down Valley (DV)	Filter samplers Optical Particle Counter Deposition trap Meteorological Station	May 9 to May 31 May 17 to May 31 June 1 to Oct 18 May 9 to May 31	60.9980, -138.5227	779.66	Located in the dust source. Main site for air sampling and meteorological data collection. Detailed information can be found in Table 2.
	Ä'äy Chù East (AAE)	Filter sampler, Meteorological station	May 4 to 14	60.9984, -138.5098	851.76	Near the Alaska Highway; PM_{10} concentrations, T, P, RH, WS, WD measured.
	Thachäl Dhäl Visitor's Center (VC)	Filter sampler, Meteorological station Deposition trap	May 15 to 27 May 15 to Oct 20	61.0133, -138.5259	779.57	Parks Canada visitor's center open during the summer and early fall. PM_{10} concentrations, T, P, RH, WS, WD measured.
	Fish Heart Island (Island)	Filter sampler, Deposition trap, Meteorological station	May 28 to 31	61.0189, -138.4909	814.19	(Former) island that is now accessible by foot, due to the drying of the A'ay Chu. PM_{10} concentrations, T, P, RH, WS, WD measured.
Deposition Only	Upper Valley (UV)	Deposition trap, Meteorological Station	May 14 to Oct 17	60.9871, -138.5638	787.32	Adjacent to the exposed riverbed, but located closer to the Kaskawulsh glacier. T, P, RH, WS, WD measured.
	Kluane Lake Research Station (KLRS)	Deposition trap	June 2 to Oct 20	61.0266, -138.4109		Research station.
	Outpost Research Station (Outpost)	Deposition trap	to Oct 20	61.0269, -138.4027		Research station.
	Christmas Bay	Deposition trap	May 29 to Oct 19	61.0663, -138.3742		Located on the opposite side of Kluane Lake, across from the river delta.

Table 2-1. Site characteristics and details on dust and meteorological monitoring equipment used from May 4 to June 1, 2018. Sites where 24-hour PM_{10} ambient mass concentrations (PM_{10} concentrations), temperature (T), pressure (P), and relative humidity (RH) is also included.

2.4.2 Meteorological measurements

The primary location of the meteorological measurements was the Down Valley site. A wide array of meteorological equipment was deployed at this site, the details of which can be found in the Supplemental Information section (Table 2-S1). All meteorological data was sampled and recorded by a datalogger (CSI Inc., Model CR3000) at several intervals depending on the instrument, and with summary statistics at 1 second, 1 minute, and 10-minute intervals.

The Upper Valley site served primarily as a meteorological station to monitor wind speed and direction upwind of the Down Valley site and to examine the behavior of incoming katabatic winds before they arrived at the source region. A propeller anemometer (RM Young, Model 05103) was installed at this site to measure wind speed and direction. Temperature, relative humidity, and barometric pressure (Vaisala, Models HMP35C and PTB 100A) were also monitored at this site; all data was recorded by a datalogger (CSI Inc., Model CR800).

The Island site was equipped with an identical set of meteorological monitoring equipment recording air temperature, relative humidity, and barometric pressure as the Upper Valley site. It was also equipped with a camera (Canon T2i with 24mm f/2.8 lens) in a custom-made weatherproof enclosure overlooking the valley, which took photos at 10-min intervals, controlled by the datalogger, during the period from May – October 2018. All meteorological data were processed to ensure their quality, excluding any time periods during which maintenance was performed on the towers from the final dataset to avoid reporting interferences induced by the presence of researchers at the sites. After data collection, all meteorological data were resampled to a timescale of five-minute intervals.

2.4.3 Sample collection and *in situ* instrumentation

An optical particle counter (OPC; Fast-Response Multichannel Monitor, FAI Instruments) was used to measure the number concentration of particles between 0.28 and 10 μm in diameter. This instrument includes 22 optical channels and provided particle size distribution measurements at 2 – 4 Hz. The OPC was operated at a sample flow rate of 1 LPM. As the instrument was located directly in the dust source, all air samples were diluted by a factor of six before analysis to avoid overwhelming the internal optics setup of the instrument. The

OPC was installed at the Down Valley station and placed so that its inlet was located at a height of 3.5 m above the ground in a weatherproof enclosure. Continuous 24-hour sampling began on May 17 at 00:00 and ended May 30 at 00:00. Information on quality control and data analyses performed to validate the OPC and gravimetric analysis can be found in the Supplemental Information section, including Figures 2-S2 and 2-S3, which present data validation calculations that utilize the method of Gillies and Berkofsky (Gillies and Berkofsky 2004).

Aerosol filter sample collection was performed using four mini-vol samplers (ARA Near-Federal Reference Method Samplers). Three of these samplers were equipped with quartz filters (Whatman, QM-A, 47 mm, 2.5 μm pore size), of which two were placed at the Down Valley site – one at 2.6 m and the other at 5.9 m. For brevity, in this text these samplers will be referred to as the 2 m and 6 m samplers, respectively. The third sampler, known as the "mobile station," was placed on a 2 m-tall stainless-steel tripod (Davis 7716, Mounting Tripod for Weather Stations) and deployed to the mobile station sites: Ä'äy Chù East, Visitor's Center, and the Island. The sampler was located at each station for several days before being moved to the next. All three of these mini-vol samplers were operated using a PM_{10} impactor and 24-hour sampling periods at a flow rate of 16.7 L min-1 (1 m3/hr). Samples collected on quartz filters were used for ICP-MS analysis of total concentrations of select minor and trace elements.

The fourth mini-vol sampler was equipped with a Nuclepore filter (Whatman® Nuclepore™ Track-Etched Membranes, 47 mm diameter, 0.4 μm pore size) and stationed at the Down Valley site, at a height of 6.1 m. The filters from this sampler were used for SEM/EDS analysis. The sampler was operated using 24-hour sampling periods; the inlet of the PM_{10} impactor was modified to allow the instrument to be operated at a lower flow rate of 10 L min-1, to accommodate the greater resistance to air flow through the Nuclepore filter.

Gravimetric analysis was performed on all filter samples in order to determine the dry mass of the particulate matter collected, from which a 24-hour average PM_{10} mass concentration was calculated. All samples were weighed both before and after sampling. Before being weighed, quartz filters were dried at 250°C for 2 hr and then placed in a clean silica-filled dessicator for 1 hr, both before and after sample collection. Nuclepore filters were dried in the desiccator for

24 hr prior to being weighted. Filters were stored in EMD Millipore PetriSlide™ containers at a temperature of –20°C before analysis.

Due to the remote locations of the various sampling sites, filter exchanges were performed in the field while taking precautions to decrease contamination before or after sampling. In general, samplers were serviced in the morning between 5:00 and 10:30 PST, when dust storms were less frequent and less intense. The used filter was carefully transferred to a protective case and subsequently replaced by an unused filter in as short a time as possible. Field blanks were regularly obtained by transferring a clean, unused filter into the air sampler followed by immediate removal, in order to gauge the level of contamination introduced during this procedure. Upon return from the field, ICP-MS and gravimetric analysis demonstrated negligible contamination for the field blank filters, as discussed in the Supplemental Information section.

Several dry-foam passive deposition traps (Hanby Company), were placed at sites in and near the delta of the Ä'äy Chù including at the Down Valley, Island, Upper Valley, and Visitor's Center sites. Deposition traps were also placed on the lakeshore opposite the delta at the Kluane Lake Research Station, Outpost, and Christmas Bay sites. These samples were used to evaluate the spatial distribution of deposited dust, including the spatial variation in the chemical composition.

Lastly, 14 soil samples were collected from the exposed sediments of the Ä'äy Chù by removing the top 1 cm of a 20 cm x 20 cm patch of soil. Only the surface of the soil was sampled, as this is the portion most likely to contribute to dust production. The locations at which the soil samples were taken are shown in Figure 2-S1 (Supplemental Information section).

2.4.4 Vertical aerosol flux calculations

The vertical aerosol mass flux of PM_{10} particles was calculated using the gradient method of Gillette et al. (1972). The parameterization is provided by Equation (2-1), where ρ is air density, u_1 and u_2 are windspeeds at heights z_1 and z_2, and n_1 and n_2 are mineral dust concentrations at heights z_1 and z_2, respectively. Calculation of C, the drag coefficient, is provided by Equation (2-2).

$$F_A = \frac{-\rho C u_1^2 (n_2 - n_1)}{u_2 - u_1} \quad (2\text{-}1)$$

$$C = \frac{(0.4)^2}{\left[\ln\left(z_2/z_1\right)\right]^2}\left[\left(\frac{u_2}{u_1}\right)^2 - 2\left(\frac{u_2}{u_1}\right) + 1\right] \quad (2\text{-}2)$$

Using (2-1) and (2-2), the vertical flux was calculated using the windspeed and gravimetric data at 5.9 m and 2.6 m at the Down Valley site. This simple flux model allowed us to evaluate, semi-quantitatively, dust emissions that occurred at the Down Valley site location.

2.4.5 Techniques for chemical composition analysis

2.4.5.1 SEM/EDS

Analysis via scanning electron microscopy coupled with energy-dispersive x-ray spectroscopy (SEM/EDS) was used to determine the mineralogy, size, and aspect ratio of particles collected on a Nuclepore filter. The sample were analyzed using a JEOL JSM 7600F instrument under high vacuum, at a voltage of 10 kV and a working distance of 15 mm. An LEI detector was employed for all EDS measurements. A total of 113 particles were analyzed in this manner.

Particles collected May 27 10:15 to May 28 8:15 (PST) at the Down Valley site were analyzed using SEM/EDS. Before analysis, a 1 cm x 1 cm piece of filter was carefully cut and attached to the sample mount using double-sided carbon tape. The sample was coated with approximately 40 nm of gold in order to render it conductive.

The nominal geometric diameter of each particle analyzed was measured along the length of the longest axis of the particle. The aspect ratio of particles was also determined, by dividing the geometric diameter by the length along the axis perpendicular to the particle's longest axis. Particle mineralogical classification was obtained by comparing EDS spectra to known mineral reference spectra (Falkovich et al. 2001). As determination of particle mineralogy was the sole goal of this method, it was assumed that the semi-quantitative elemental composition output of the EDS analysis was sufficient for our purposes, and no steps were taken to ensure the elemental composition results were quantitative. Pure minerals were defined as those containing only Si (quartz), only Ca (calcite), only Ca and S at a 1:1 ratio (gypsum), or only

Ca and Mg (dolomite). Clay minerals were defined as containing Si accompanied by either Al, alkali metals, alkali earth metals, or a combination thereof.

2.4.5.2 ICP-MS

A modified version of EPA method 3051a (EPA 2007) was used to analyze trace and minor element concentrations in both soils, PM_{10}, and deposited aerosol samples using inductively coupled plasma-mass spectrometry (ICP-MS).The method was scaled down in order to work with the small sample sizes (20-40 mg) that were available due to the use of mini-vol samplers. In addition, a mixture of ultrapure HNO_3 (67-70%, BDH ARISTAR ULTRA, supplied by VWR International) and HCl (TraceMetal Grade, Fischer Chemical) were used for the digestion of samples, due to the infeasibility of using HF at our facilities.

Filter samples were digested by cutting filters into small pieces and placing them in microwave digestion tubes. The mass obtained from gravimetric analysis was used as the sample mass for the analyses of the filter samples; this number was typically 20-40 mg, depending on how much PM_{10} had been collected during the 24-hr sampling period. For the soils, digestions were performed by measuring 25 mg of each sample analyzed into the Teflon tubes. Deposition trap samples were analyzed in exactly the same manner as soil samples. A more detailed description of the digestion process employed can be found in the Supplemental Information section.

Samples were pre-digested for 4 hrs in a fume hood to avoid violent reactions upon heating. Tubes were then placed in a Mars-Xpress CEM Digestion Microwave and subjected to an initial temperature ramp to 140°C that lasted 5.5 min with a subsequent holding period of 4.5 min. After a 5-min cooling period, samples were removed from the apparatus; transferred to clean, pre-weighed 50-mL polypropylene tubes; diluted by a factor of 7 for soil samples and 8 for PM_{10} samples; and filtered using a syringe filter (Fisherbrand 25 mm nylon syringe filters, 0.45 μm pore size, sterile). Three standard reference soils – NIST 2710a, NIST 2711a, and NIST 8704 – as well as acid blanks were digested alongside soil and aerosol samples in order to confirm the quantitative recovery of metals contained in the samples and to verify that no contamination was introduced during the digestion process.

Samples were then analyzed via ICP-MS (Perkin Elmer, NexION 300x) using calibration standard IV-71a and quality control standard QCS-27 (Inorganic Ventures). Standard solutions of 0.5 – 200 µg/L prepared from IV-71a were used for calibration, and a 50 µg/L quality control solution prepared from QCS-27 was also used. Data for a given metal were accepted as quantitative if NIST SRM recovery was 80 – 110 %, the calibration curve R2 was greater than 0.999, and the solution-phase quality control analysis was within 10 % of the known concentration of QCS-27.

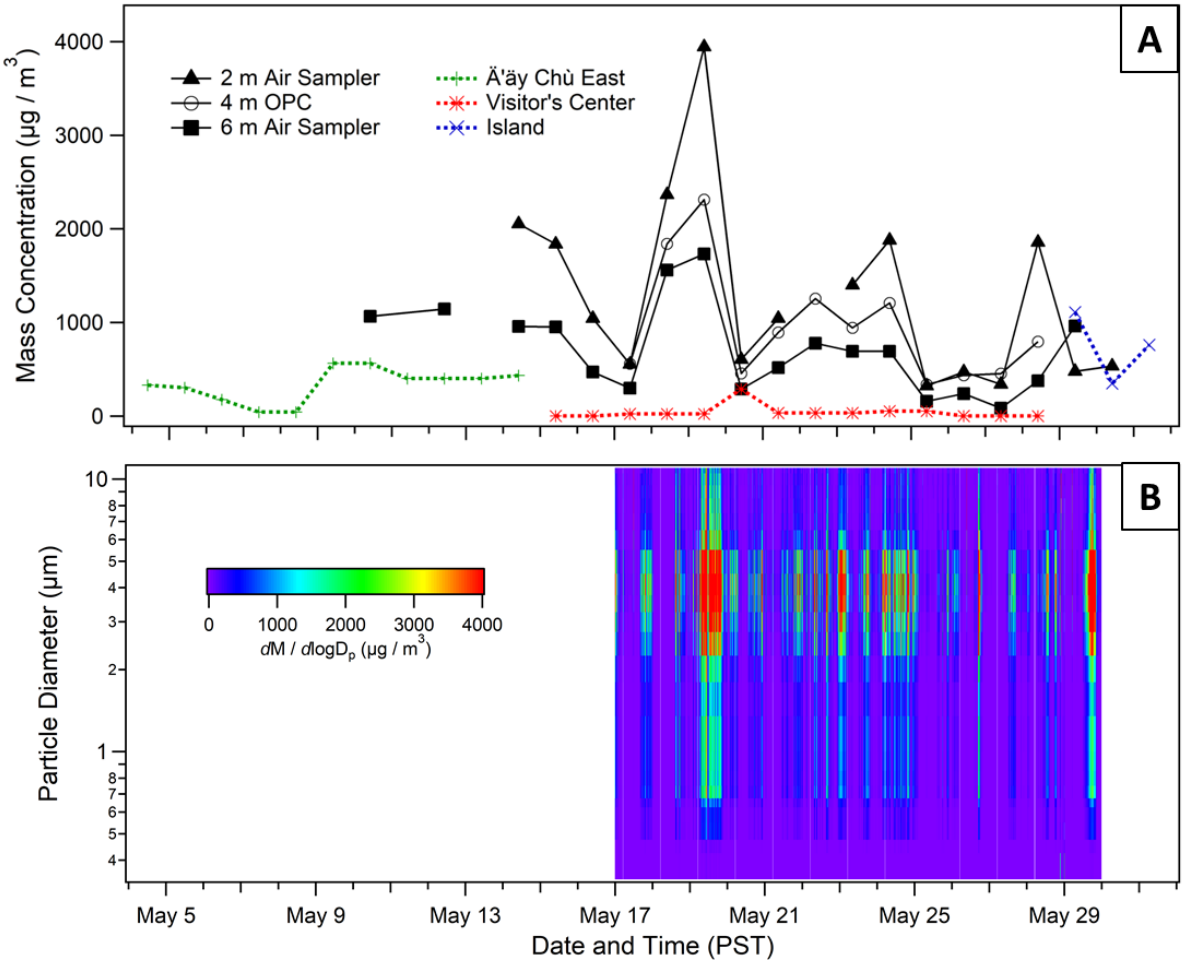

Figure 2-3. Time series of (A) 24-hour averaged PM_{10} mass concentrations at all sites, determined using gravimetric analysis of filter samples. The size-resolved particle number concentrations output by the OPC was also used to calculate the 24-hour averaged PM_{10} mass concentrations at 4 m. (B) Five-minute resolution OPC data.

2.5 Results and Discussion

2.5.1 Particle sizing and ambient mass concentrations

2.5.1.1 Time series data

The measured particle size distribution (dM/dlogDp) from the Down Valley site and the 24-hour averaged PM_{10} concentrations from the Down Valley, Ä'äy Chù East, Visitor's Center, and Island sites are depicted in Figure 2-3. Given that the Down Valley site was located directly in the exposed delta of the Ä'äy Chù and that the PM_{10} concentrations were substantially higher at this site compared to the other sites, the particle sizing and gravimetric analysis of samples from the Down Valley site were taken to be indicative of dust emissions from the Ä'äy Chù Valley. The 24-hour data from the filter samples shows a significant event occurred within the filter sampling period of May 19 at 11:00 to May 20 at 9:00 (PST), with the OPC data indicating the event took place on May 19 between 6:00 and 21:00 (PST). Based on our time series data, this period exhibited the highest ambient concentrations of PM_{10} observed at the Down Valley site. The period between May 20 and May 25 is marked by multiple periods of elevated mineral dust concentration per day, followed by a less-dusty period between May 25 and May 27. Both the gravimetric and OPC data show increased dust emissions on May 29. Gravimetric analysis indicates that dust events occurred May 14 and 15, though no OPC data is available for these dates and thus fast time-resolution measurements of these events are unavailable. The particle size distribution showed little variation with time, as is evident in Figure 2-4.

In addition, Figure 2-4 shows the particles in the PM_{10} size range to be quite fine, with a maximum in the mass size distribution of 3.25 μm. This is a key result, as the PM_{10} size distribution recorded in this study is very fine as compared to those previously found by studies of more well-characterized dust sources, such as Northern Africa, the Sahara, China, and Australia; results compiled by Huang et al. (2019) found the maximum of the volume size distribution for PM_{10} collected from these low-latitude dust sources to be closer to 10 μm. Huang et al. presented their results as the geometric diameter, while our OPC measurements report the optical diameter; however, we have confirmed the size distribution measured by our

OPC with the particle size distribution measured by an aerodynamic particle sizer (APS) that also sampled ambient PM_{10} in the Ä'äy Chù Valley (Figure 2-S4). This confirmation, as well as the quality control analysis previously described in the experimental section that confirm the OPC measurements, indicate that there is a negligible difference between the OPC measured optical diameter provided in Figure 2-4 and the geometric diameter of particles. Further discussion of the dust emission mechanisms that may have resulted in the fine PM_{10} size distribution measured can be found in the dust emission mechanism section of this discussion.

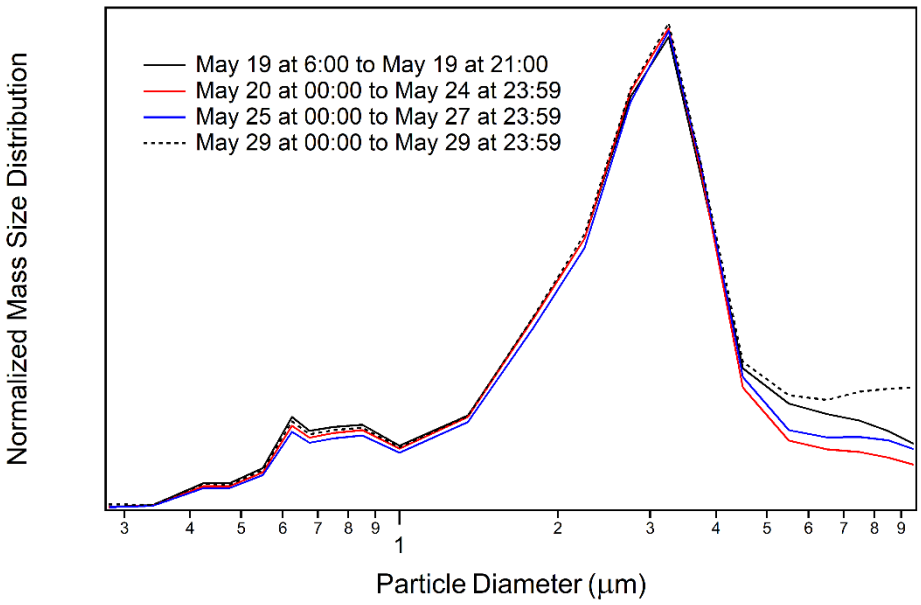

Figure 2-4. Normalized particle mass size distribution from the OPC data averaged over four time periods. Maximum at a particle diameter of 3.25 µm.

2.5.1.2 Diurnal Trends in Ambient PM_{10}

The diurnal variation of the ambient PM_{10} mass concentration, as calculated from the OPC data, is depicted in Figure 2-5. While ambient dust concentrations are highly variable from day to day, ambient PM_{10} concentrations are generally highest in the afternoon and evening, between 13:00 and midnight (PST) and the early morning hours of 5:00 to 10:00 (PST) correspond to the lowest PM_{10} concentrations. The magnitude of net radiation measured by the net radiometer is generally close to zero at hours of the day when significant PM_{10} concentrations were observed, demonstrating that dust activity was not restricted to daylight hours. Even though it is true that ambient dust may alter the net surface radiation budget, we use the net radiometer data here as a more general indicator of daytime versus nighttime over the course of our sampling campaign. This finding demonstrates that passive remote sensing of mineral dust emissions in the Arctic that is limited to daytime hours may miss dust production that occurs at night.

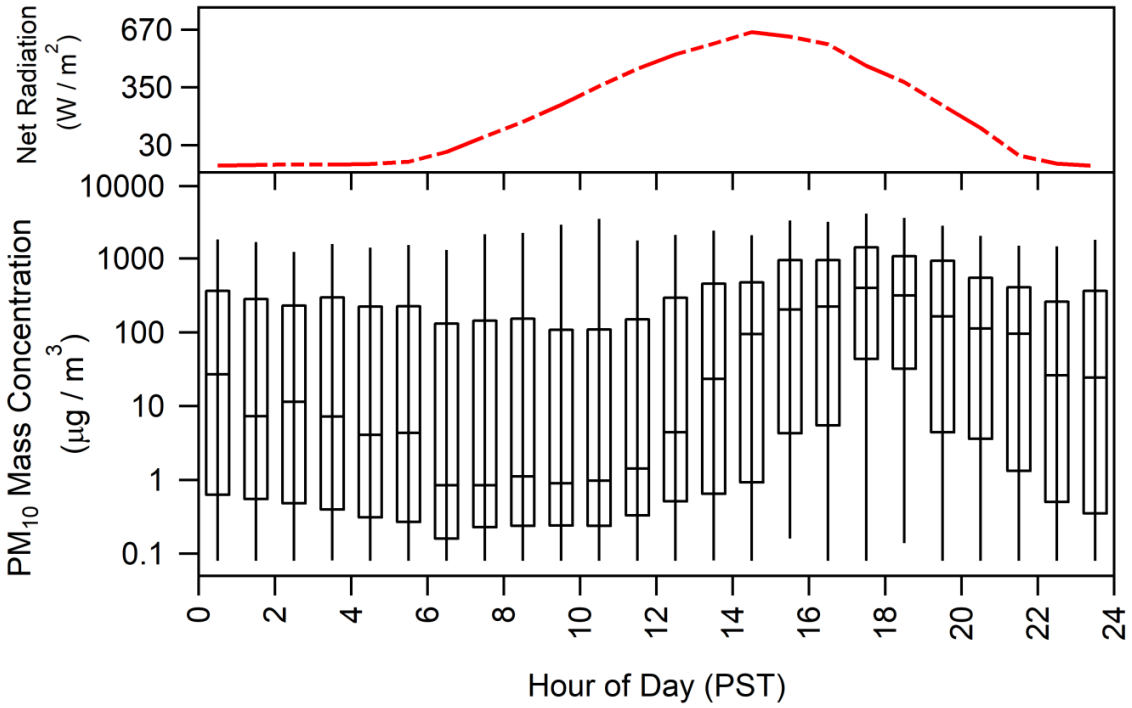

Figure 2-5. Diurnal trends in ambient PM_{10} concentrations at the Down Valley site, as determined from the OPC data. Box-and-whisker plots show the minimum, 25 % quartile, median, 75 % quartile, and maximum of the data obtained continuously between May 17 and May 29, 2018. The upper panel indicates the mean net radiation at the Down Valley site between May 4 and June 2, indicating the approximate range of daylight hours during this period.

2.5.1.3 Correlation between PM_{10} and $PM_{2.5}$ and comparison with air quality standards

While no $PM_{2.5}$ filter samples were collected during the campaign, the $PM_{2.5}$ concentration was calculated using the OPC data. Furthermore, the OPC data showed a strong correlation between the calculated mass concentrations of PM_{10} and $PM_{2.5}$. The 5-minute resolution data gave an R^2 value 0.88. However, when a single data point (May 28 at 9:50 P.M.) was removed, the coefficient increased to 0.95.

$$PM_{2.5} = 11.911 + 0.2156 * PM_{10} \qquad (2\text{-}3)$$

Given the exceptional correlation between PM_{10} and $PM_{2.5}$, we applied equation (2-3) – the interpolation equation relating the ambient mass concentrations of PM_{10} and $PM_{2.5}$ at the Down Valley site – to the 24-hr PM_{10} concentration data obtained from the Mobile Station Sites (Ä'äy Chù East, Visitor's Center, and Island), in order to estimate $PM_{2.5}$ concentrations at these sites. The mobile station site $PM_{2.5}$ concentrations estimated using this method are likely a lower-bound of the $PM_{2.5}$, as the settling mechanisms of mineral dust result in larger particles being deposited at a faster rate. Thus, $PM_{2.5}$ could potentially make up a slightly larger percentage of the PM_{10} size fraction at the mobile station sites than it does at the Down Valley site located directly in the dust source.

2.5.1.4 Comparison of PM_{10} and $PM_{2.5}$ concentrations with air quality standards

The measured 24-hour average PM_{10} and estimated $PM_{2.5}$ concentrations at the various mobile station sites (Ä'äy Chù East, Visitor's Center, and Island) were then compared to air quality thresholds provided by the WHO (2006). The results of this comparison is shown in Figure 2-6. The 24-hr air quality standard for ambient PM_{10} concentrations provided by the WHO is 50 $\mu g/m^3$, which is a target value for limiting risks to public health; the corresponding limit for $PM_{2.5}$ concentrations is 25 $\mu g/m^3$ (WHO 2006). Based on these air quality guidelines, it is evident that both the PM_{10} and $PM_{2.5}$ limits of the WHO were surpassed at all three sites during our sampling campaign. Moreover, the estimated $PM_{2.5}$ surpassed the WHO $PM_{2.5}$ limits on all days when the WHO PM_{10} limits were surpassed. Despite the short duration of

the measurement campaign, the results indicate that the emitted mineral dust negatively impacts air quality in locations near the Ä'äy Chù that are frequently visited by tourists.

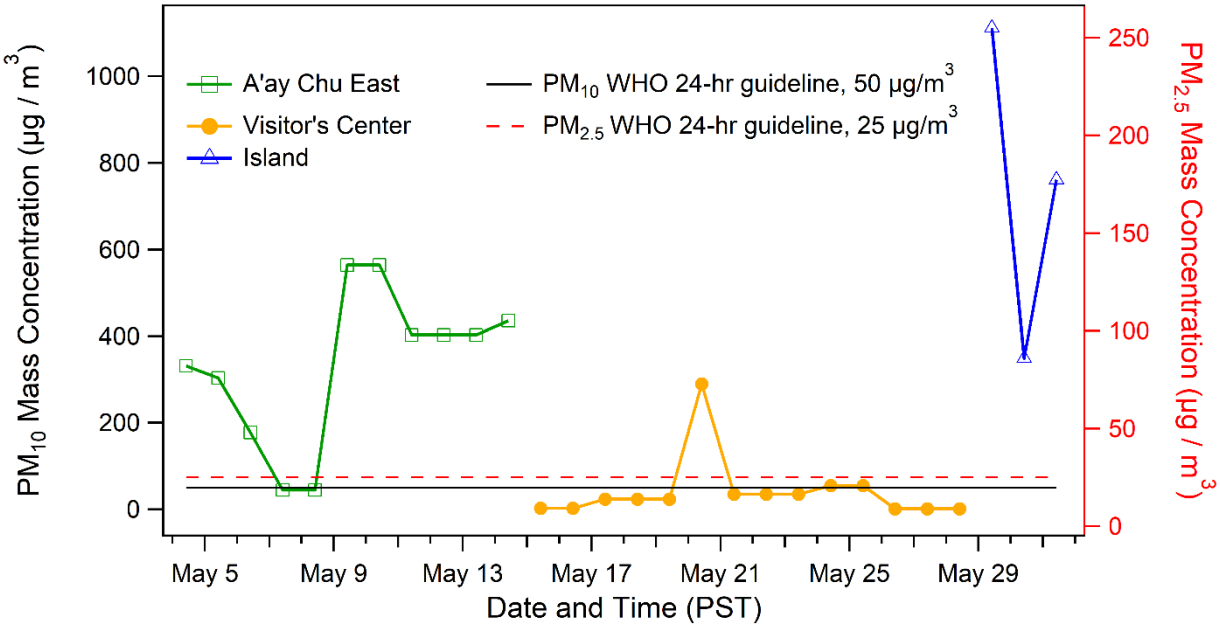

Figure 2-6. Comparison of 24-hour ambient PM_{10} (right axis) and $PM_{2.5}$ (left axis) mass concentrations observed at mobile station sites with the air quality guidelines of the World Health Organization (WHO). The WHO guidelines are 50 µg/m^3 and 25 µg/m^3

2.5.2 SEM/EDS analysis of ambient PM_{10}

The mineralogical composition of individual dust particles collected on May 27 at 10:15 to May 28 at 8:15 at a height of 6 m at the Down Valley site was determined based on the work of Falkovich et al,(Falkovich et al. 2001) and is shown in Table 2-2. The elements Si, Ca, Al, Mg, Fe, K, Na, and S were detected in the course of our analysis. It was found that the analyzed sample consisted of both pure minerals – quartz, calcite, gypsum, and dolomite – and aluminosilicate aggregates. These aggregates, which made up 75.7 % of all particles analyzed, were primarily clay minerals; through analysis of element ratios, certain clay minerals were

identified as being aggregated with pure minerals. For example, all clay minerals containing 1:1 of Ca and S were classified as aggregates of clay with gypsum. Examples of EDS spectra of particles and their corresponding mineralogical classification can be found in the Supplemental Information section (Figure 2-S5).

Mineral Class		% Frequency (n = 115)
Pure Minerals	Quartz (Si)	7.8
	Calcite (Ca)	7.0
	Gypsum (Ca and S)	5.2
	Dolomite (Ca and Mg)	4.3
Clay Minerals		75.7

Table 2-2. Mineralogical classification of PM_{10} particles (d < 10 μm) collected at the Down Valley site (h = 6 m) on May 27, 2018.

Of all the particles sampled, 63.5 % contained Al, 22.6 % contained Fe, and 13.0 % contained Na; these elements were present in particles all classified as clay minerals. Calcium was present in 42.6 % of all particles, with 26.1 % of all particles being clay minerals with calcium and 16.5 % of all particles classified as either calcite, gypsum, or dolomite. It is important to note that the mineralogical data obtained through this analysis is semi-quantitative due to the small sample size in terms of the number of particles analyzed (n = 113); however, the SEM/EDS results nevertheless provide information regarding the major element content of the PM_{10} collected, and the data indicate a large presence of aluminosilicate and calcium-containing minerals. Finally, the particle aspect ratios were also measured giving a mean value of 1.60 ± 0.53, where the error provided is the standard deviation. The aspect ratio analysis indicated that the majority of particles (88 %) were non-spherical, with certain particles possessing aspect ratios exceeding 3.0 (Figure 2-S6).

2.5.3 Minor and trace element content

2.5.3.1 Method evaluation results

Our results indicate that the modified version of EPA 3051a we employed for our sample digestions quantitatively extracts the following nine metals from both PM_{10} and soil samples for ICP-MS analysis: Mn, Fe, Co, Ni, Cu, As, Cd, Cs, and Pb. The results of our validation tests are discussed in the Supplemental Information section, while the elemental recoveries and limits of detection of our analyses can be found in Tables 2-S2 and 2-S3.

2.5.3.2 Elemental Composition of Soil, PM_{10}, and Deposited Mineral Dust Samples

ICP-MS results are provided in Table 2-3 for all analyzed ambient PM_{10}, dust deposition, and soil samples. Due to the quantity of samples analyzed, we have also condensed the data into a summary of compositions by sample type in Table 2-4. It is noteworthy that due to the low sample mass, elemental analysis of dust deposition collected from the Visitor's Center was not possible.

The analyzed elemental composition of PM_{10} is quite consistent between the Down Valley and mobile station sites and varies very little from day-to-day. This can be seen in the low relative standard errors (RSE) of the averaged PM_{10} composition in Table 2-4, which do not exceed 5 % for any metal except Cd. Thus, the ambient PM_{10} samples analyzed showed little spatial or temporal variation in their chemical composition, with Cd being the most variable elements and Fe and Mn content showing the least spatial and temporal variation. Fine soil samples demonstrated increased variability in As (RSE of 28.9 %) and Pb (RSE of 28.6 %) as compared to the other analyzed metals. The As content was generally higher in the most up-valley soil samples (B and C, both fine and bulk soil samples), as well as those closest to Kluane Lake (J, K, M, N, both fine and bulk soil samples where applicable). This subset of soil sample sites where As was found to be higher were also higher in Pb contentanalysed.

More spatial variation was observed in the composition of the dust deposition samples than the PM_{10} air samples. Trends in dust deposition composition are in Table 2-3, as samples are listed in order of their proximity to the Kaskawulsh glacier, with the Upper Valley site being

the closest and Christmas Bay being the furthest site. At sites more removed from the river delta, such as Kluane Lake Research Station, Outpost Research Station, and Christmas Bay, it is not certain whether all the dust deposition collected originated from the exposed sediment of the Ä'äy Chù, as it is possible that a portion of the dust collected originated from other sources as well (such as road dust or natural dust sources nearby). The sample collected from Christmas Bay is of note in its deviation from the other samples. It comprised the lowest content of As and Mn, as well as the highest content of Ni, Cd, and Pb, as compared to the other analyzed dust deposition samples. The elevated lead content of the Outpost and Christmas Bay samples could likely be due to the increased proximity of these sites to areas of human habitation. The composition data for the deposition samples indicates that the impact of the dust plumes in terms of the deposition of metals extends at least a distance of approximately 5 km across the southern portion of Kluane Lake.

Sample Label		Mn (mg/kg)	Fe (%)	Co (mg/kg)	Ni (mg/kg)	Cu (mg/kg)	As (mg/kg)	Cd (mg/kg)	Cs (mg/kg)	Pb (mg/kg)
Soils (Bulk)										
	A	524.04	2.59	11.87	44.00	50.03	7.24	0.63	0.82	8.65
	B	423.07	2.42	9.57	35.53	44.74	10.01	0.40	0.68	5.58
	C	537.51	2.60	11.91	48.10	40.13	8.69	0.83	1.09	6.66
	D	552.26	3.43	15.18	56.81	47.11	5.35	0.34	1.06	8.17
	F	443.13	2.59	9.65	25.66	28.79	< LOD	0.65	0.79	4.03
	G	469.17	2.25	10.51	32.72	41.26	3.76	0.44	0.65	6.60
	H	536.98	3.19	14.60	57.18	50.86	9.80	0.78	1.59	8.16
	L	453.31	2.26	9.77	31.21	27.36	0.00	0.41	0.67	5.62
	M	444.44	2.20	9.07	29.75	31.59	3.30	0.23	0.80	5.07
	Average ± SE (%RSE)	487.1 ± 16.65 (3.42 %)	2.62 ± 0.14 (5.46 %)	11.35 ± 0.75 (6.6 %)	40.11 ± 3.95 (9.84 %)	40.21 ± 3 (7.47 %)	5.35 ± 1.29 (24.15 %)	0.52 ± 0.07 (13.25 %)	0.9 ± 0.1 (11.17 %)	6.5 ± 0.53 (8.09 %)
Soils (Fine, d < 53 µm)										
	A	564.66	3.39	12.19	35.54	74.53	< LOD	1.06	0.80	6.08
	B	595.84	3.70	18.46	56.13	86.53	47.31	1.00	0.81	14.71
	C	767.47	3.93	18.80	75.66	80.94	10.22	0.75	1.68	11.59
	D	571.53	3.65	16.25	61.87	69.14	3.03	0.58	1.09	8.66
	E	490.78	2.24	9.78	36.28	94.96	2.98	0.31	0.72	7.22
	F	528.66	3.26	12.72	37.94	84.78	2.51	1.12	0.60	6.17
	G	495.01	2.30	11.49	33.87	52.44	8.40	0.44	0.60	7.09
	H	553.54	3.21	14.48	59.10	72.93	8.01	0.85	1.53	8.43
	I	517.52	2.53	11.37	39.81	66.48	7.59	0.22	0.48	7.37
	J	642.36	3.10	15.15	47.22	107.38	11.68	0.99	0.65	9.09
	K	640.04	3.25	17.61	57.89	97.05	14.95	0.66	0.66	9.51
	L	604.69	2.87	13.60	46.91	78.70	9.67	0.67	0.71	8.71
	M	665.32	3.55	17.90	55.59	119.90	28.76	0.74	0.70	10.25
	N	551.62	2.54	11.09	37.79	96.07	19.38	0.49	0.80	53.57
	*R1***	*418.95*	*2.25*	*8.56*	*43.89*	199.85	*4.36*	*<LOD*	*0.74*	*5.97*
	*R2***	*468.74*	*2.53*	*12.21*	*45.39*	*114.91*	*6.74*	*<LOD*	*0.87*	*7.37*
	Average ± SE (%RSE)	567.3 ± 20.16 (3.55 %)	3.02 ± 0.14 (4.77 %)	13.86 ± 0.81 (5.88 %)	48.18 ± 3.37 (6.99 %)	93.54 ± 4.72 (5.04 %)	11.6 ± 3.35 (28.87 %)	0.62 ± 0.07 (12.01 %)	0.84 ± 0.09 (11.28 %)	11.36 ± 3.25 (28.63 %)
Dust Deposition										
	Upper Valley (May to Oct)	418.11	2.84	14.49	48.05	51.07	10.24	1.08	0.84	8.50
	Down Valley (May)	465.45	2.51	17.72	38.20	49.23	7.69	1.11	0.76	6.14
	Down Valley (June to Oct)	442.78	2.37	14.68	34.09	41.87	9.75	0.74	0.60	7.21
	Island Site (May)	506.16	2.82	12.68	49.20	49.10	6.97	0.59	1.04	6.30
	KLRS (May to Oct)	423.43	2.20	9.97	36.26	34.60	8.68	0.78	0.36	7.38
	Outpost (May to Oct)	557.63	3.17	14.78	56.97	45.87	10.61	1.14	0.52	9.55
	Christmas Bay (May to Oct)	318.00	3.05	13.84	75.44	49.55	6.74	1.27	0.20	9.85
	Average ± SE (%RSE)	444.4 ± 33.5 (7.5 %)	2.74 ± 0.16 (7.5 %)	13.4 ± 0.8 (5.6 %)	50 ± 6.2 (12.3 %)	45.3 ± 2.5 (5.6 %)	8.8 ± 0.7 (7.7 %)	0.9 ± 0.1 (11.7 %)	0.6 ± 0.1 (21.2 %)	8.1 ± 0.6 (7 %)

Table 2-3. Elemental composition of all samples analyzed via ICP-MS. Sample label corresponds to the sample name in Figure 2-S1, with both the bulk and the fine fraction (d < 53 µm) analyzed. Analyses where the elemental content was below the limit of detection (LOD) are also indicated. ** Indicates samples not included in total average.

Sample Label		Mn (mg/kg)	Fe (%)	Co (mg/kg)	Ni (mg/kg)	Cu (mg/kg)	As (mg/kg)	Cd (mg/kg)	Cs (mg/kg)	Pb (mg/kg)
Ambient PM10 (Down Valley, h = 2m)										
	May 14 10:00 to May 15 9:00	662.22	5.10	23.11	76.80	75.04	21.55	0.99	1.43	15.81
	May 15 9:15 to May 16 7:00	714.15	4.89	23.61	77.53	75.81	18.67	0.60	1.69	16.02
	May 23 10:10 to May 24 9:20	636.06	4.41	21.58	70.30	68.31	19.44	1.04	1.34	13.46
	May 29 9:15 to May 30 9:25	711.02	4.76	25.08	70.63	70.17	21.01	1.74	1.54	16.44
	Average ± SE (%RSE)	680.9 ± 19.1 (2.8 %)	4.79 ± 0.15 (2.8 %)	23.3 ± 0.7 (3.1 %)	73.8 ± 1.9 (2.6 %)	72.3 ± 1.8 (2.5 %)	20.2 ± 0.7 (3.3 %)	1.1 ± 0.2 (21.7 %)	1.5 ± 0.1 (5.1 %)	15.4 ± 0.7 (4.3 %)
Ambient PM10 (Down Valley, h = 6m)										
	May 14 10:20 to May 15 9:20	642.58	4.52	22.46	70.54	66.72	18.23	1.08	1.50	14.53
	May 15 9:45 to May 16 7:15	741.94	5.06	25.38	82.82	82.69	17.40	0.44	1.61	16.70
	May 22 9:20 to May 23 9:15	661.92	4.63	22.41	73.06	70.12	19.38	1.11	1.57	14.48
	May 23 10:30 to May 24 9:25	670.56	4.53	23.06	74.59	75.62	20.91	1.07	1.59	14.00
	May 29 9:30 to May 30 9:40	661.15	4.41	22.84	73.07	72.85	20.13	1.46	1.32	16.10
	Average ± SE (%RSE)	675.6 ± 17.2 (2.5 %)	4.63 ± 0.11 (2.5 %)	23.2 ± 0.6 (2.4 %)	74.8 ± 2.1 (2.8 %)	73.6 ± 2.7 (3.7 %)	19.2 ± 0.6 (3.3 %)	1 ± 0.2 (16 %)	1.5 ± 0.1 (3.5 %)	15.2 ± 0.5 (3.5 %)
Ambient PM10 (Mobile Station)										
A'ay Chu East	May 11 10:50 to May 12 20:00	714.11	4.59	23.05	79.22	78.78	18.39	1.00	1.57	15.86
A'ay Chu East	May 14 12:05 to May 15 11:45	729.96	4.53	25.85	67.89	61.56	20.18	1.70	1.74	14.78
Visitor's Cent	May 20 9:55 to May 21 10:15	640.28	4.28	27.88	63.74	59.03	14.48	1.66	1.96	20.70
Island	May 29 13:05 to May 30 10:40	633.74	4.31	18.66	72.60	62.44	17.03	0.93	1.64	12.09
Island	May 30 10:44 to May 31 13:55	658.60	4.29	22.89	68.89	57.68	14.97	1.86	1.28	12.87
	Average ± SE (%RSE)	675.3 ± 19.7 (2.9 %)	4.4 ± 0.07 (2.9 %)	23.7 ± 1.6 (6.6 %)	70.5 ± 2.6 (3.7 %)	63.9 ± 3.8 (6 %)	17 ± 1.1 (6.2 %)	1.4 ± 0.2 (13.5 %)	1.6 ± 0.1 (6.7 %)	15.3 ± 1.5 (9.9 %)

Table 2-3 (continued). Elemental composition of all samples analyzed via ICP-MS.

	Soils, Bulk (n = 9)	Soils, d < 53 µm (n = 14)	Dust Deposition¥ (n = 6)	Ambient PM_{10} (Down Valley** and Mobile)
Mn (mg/kg)	487.1 ± 16.65 (3.42 %)	567.3 ± 20.16 (3.55 %)	444.4 ± 33.5 (7.5 %)	675.48 ± 12.31 (1.82 %)
Fe (%)	2.62 ± 0.14 (5.46 %)	3.02 ± 0.14 (4.77 %)	2.74 ± 0.16 (7.5 %)	4.52 ± 0.72 (1.6 %)
Co (mg/kg)	11.35 ± 0.75 (6.6 %)	13.86 ± 0.81 (5.88 %)	13.4 ± 0.8 (5.6 %)	23.45 ± 0.78 (3.34 %)
Ni (mg/kg)	40.11 ± 3.95 (9.84 %)	48.18 ± 3.37 (6.99 %)	50 ± 6.2 (12.3 %)	72.64 ± 1.74 (2.39 %)
Cu (mg/kg)	40.21 ± 3 (7.47 %)	93.54 ± 4.72 (5.04 %)	45.3 ± 2.5 (5.6 %)	68.75 ± 2.74 (3.98 %)
As (mg/kg)	5.35 ± 1.29 (24.15 %)	11.6 ± 3.35 (28.87 %)	8.8 ± 0.7 (7.7 %)	18.11 ± 0.69 (3.8 %)
Cd (mg/kg)	0.52 ± 0.07 (13.25 %)	0.62 ± 0.07 (12.01 %)	0.9 ± 0.1 (11.7 %)	1.23 ± 0.14 (11.13 %)
Cs (mg/kg)	0.9 ± 0.1 (11.17 %)	0.84 ± 0.09 (11.28 %)	0.6 ± 0.1 (21.2 %)	1.58 ± 0.06 (3.85 %)
Pb (mg/kg)	6.5 ± 0.53 (8.09 %)	11.36 ± 3.25 (28.63 %)	8.1 ± 0.6 (7 %)	15.21 ± 0.76 (4.97 %)

Table 2-4. Average elemental composition per sample type – bulk soils, fine soil fraction (d < 53 µm), dust deposition, and ambient PM_{10} – as determined via ICP-MS. Standard error and relative standard error are also provided.

¥Data from Down Valley Site (May Only) excluded from average. ** Data from sampler at 6 m height used only.

Site	Mn (ng/m³)		Fe (µg/m³)		Co (ng/m³)		Ni (ng/m³)		Cu (ng/m³)		As (ng/m³)		Cd (ng/m³)		Cs (ng/m³)		Pb (ng/m³)	
Downvalley	*2m*	*6m*	*2m*	*6m*	*2m*	*6m*	*2m*	*6m*	*2m*	*6m*	*2m*	*6m*	*2m*	*6m*	*2m*	*6m*	*2m*	*6m*
May 14	1361.06	615.22	10.48	4.33	47.50	21.50	157.85	67.54	154.23	63.88	44.29	17.45	2.03	1.03	2.94	1.44	32.49	13.91
May 15	1313.47	708.46	8.99	4.83	43.42	24.23	142.59	79.08	139.43	78.96	34.34	16.61	1.10	0.42	3.11	1.54	29.46	15.95
May 22		515.89		3.61		17.47		56.94		54.65		15.10		0.87		1.22		11.29
May 23	891.15	464.60	6.18	3.14	30.23	15.98	98.49	51.68	95.71	52.39	27.24	14.49	1.46	0.74	1.88	1.10	18.86	9.70
May 29	340.02	636.69	2.28	4.25	11.99	22.00	33.78	70.37	33.56	70.15	10.05	19.39	0.83	1.41	0.74	1.27	7.86	15.50
Ä'äy Chù Eas	*3m*		*3m*		*3m*		*3m*		*3m*		*3m*		*3m*		*3m*		*3m*	
May 14	287.68		1.85		9.29		31.91		31.74		7.41		0.40		0.63		6.39	
May 15	318.14		1.97		11.27		29.59		26.83		8.79		0.74		0.76		6.44	
Visitor's Cen																		
May 20	185.73		1.24		8.09		18.49		17.12		4.20		0.48		0.57		6.00	
Island																		
May 23	704.80		4.79		20.75		80.74		69.44		18.94		1.03		1.82		13.45	
May 29	229.81		1.50		7.99		24.04		20.13		5.22		0.65		0.45		4.49	

Table 2-5. 24-hour averaged ambient concentrations of the measured trace elements in the ambient PM_{10} at the Down Valley and mobile station sites.

2.5.3.3 Ambient concentrations of minor and trace elements in PM_{10}

We have calculated the total concentration of each analyzed trace element in the aerosol samples in ng/m^3 and provided this data in Table 2-5. As the composition of the collected PM_{10} air samples did not show significant day-to-day or site-to-site variation, we find that the ambient concentrations of each metal follow the trends of the gravimetric analysis, with lower ambient minor and trace element concentrations at 6 m as compared to 2 m at the Down Valley site, and higher concentrations at the Island and Ä'äy Chù East sites than at the Visitor's Center. However, there are some instances when the concentrations observed at the Visitor's Center equalled or even slightly surpassed those of the other two mobile station sites, such as in the case of Co, Cd, Cs, and Pb. This may be due to the proximity of the Visitor's Center site to human activity, slight differences in the composition of the dust at this site, or the differences in aerosol concentration since the days the measurements were taken at the visitor center and the other mobile station sites were not the same.

2.5.3.4 Comparison of ambient PM_{10}, dust deposition, and soil samples

In order to compare the elemental compositions of our samples, we have compared the enrichment factor of the Down Valley site ambient PM_{10} elemental composition with the other sample types. This factor was calculated for each element analyzed by determining the ratio between the mass fraction in the Down Valley site PM_{10} at a height of 6 m and the mass fraction of the element in each of the other sample types (mobile sites, deposition, fine soils, and bulk soils). The results of our comparison can be found in Figure 2-7.

There are distinct trends in the elemental composition when comparing between sample types. Firstly, the enrichment factor of the Down Valley site ambient PM_{10} composition relative to that of the mobile station sites hovers near 1, indicating a similar composition between the PM_{10} samples collected at our air sampling sites throughout the river delta and at the Island site. Cd is an exception to this rule, likely because it has the lowest concentrations out of the metals we have quantified, and thus might be more influenced by contamination and measurement interferences. Figure 2-7 also demonstrates an overall elemental enrichment in the ambient PM_{10} samples as compared to the bulk soils. This trend is still apparent, but less

pronounced, when comparing the Down Valley site PM_{10} with the fine fraction of the soils and dust deposition. In this case, there are certain exceptions to the overall trend of PM_{10} enrichment, such as for Cd (for which the concentration is statistically equivalent between Down Valley PM_{10} and deposition samples) and Cu (for which the concentration is statistically equivalent in the fine fraction of soils and PM_{10}). Moreover, the elemental composition of the deposition samples is relatively similar to that of the fine fraction of the soils; the difference is much less pronounced than the difference between PM_{10} and fine soil samples.

As these trends in sample composition were observed, an ANOVA test was performed to more quantitatively compare the observed trends described above. The results of the ANOVA can be found in Table 2-S4. Overall, the ANOVA analysis indicated a significant difference between the elemental composition of PM_{10} samples as compared to either dust deposition, bulk soils, and the fine fraction of soils, for all elements analyzed except for Pb.

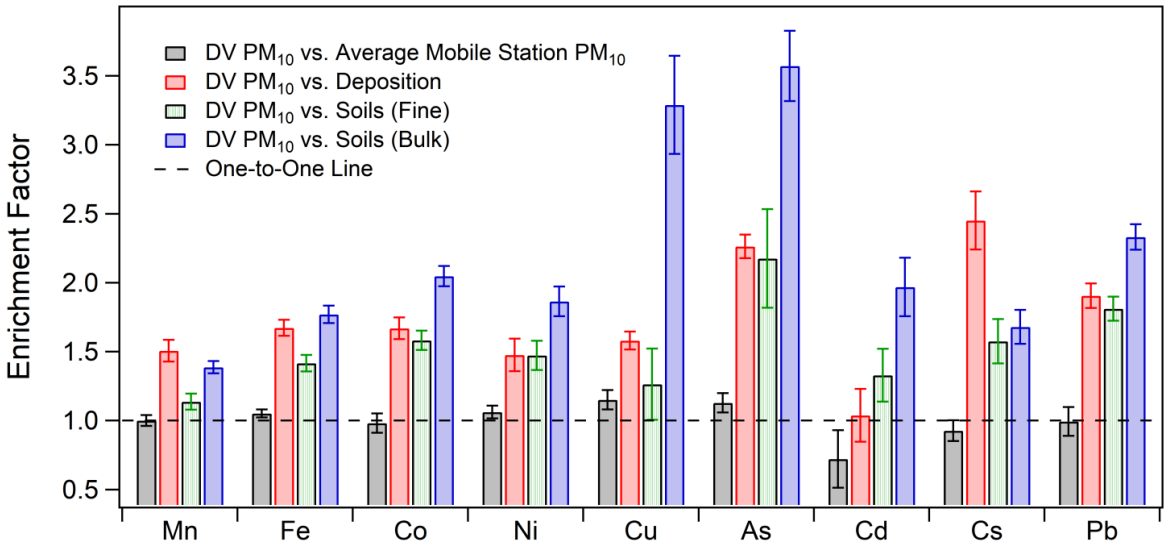

Figure 2-7. Bar graph of Down Valley site (DV) PM_{10} enrichment of trace elements as compared to Mobile Station PM_{10}, deposited dust, fine soils ($d < 53$ µm), and bulk soils.

2.5.4 Evaluation of dust production mechanisms

2.5.4.1 Contribution of saltation-sandblasting

Parameterizations of dust emissions make the, often correct, assumption that vertical aerosol flux is proportional to horizontal flux. This is because saltation/sandblasting processes – in which larger, dense, wind-blown particles impact upon the surface, thus releasing fine sediments that would otherwise be too small to be entrained due to their low resistance in an airflow – are thought to be the dominant mechanism responsible for dust emission (Shao 2008). However, the details of this mechanism can vary depending on the composition and size distribution of particles in the erodible soils, and thus parameterizations of dust emission developed based on low-latitude dust sources may not be applicable to high-latitude dust sources whose erodible soils may differ greatly in size and composition. Moreover, it is also possible for dust entrainment to occur through processes other than sandblasting, such as through direct aerodynamic entrainment (Loosmore and Hunt 2000; Shao 2001).

We began by confirming whether the location of the Down Valley site was indeed a site of dust emission. By applying the method of Gillette et al. (1972), we calculated the daily net vertical aerosol flux as described in the experimental section. The results of this analysis can be found in Table 2-S5. We observed dust emissions on almost every day of our sampling campaign, with the exception being May 29. As a result, we concluded that we could safely assume that the location of our sampling instruments in the Ä'äy Chù Valley was indeed a site of dust emissions.

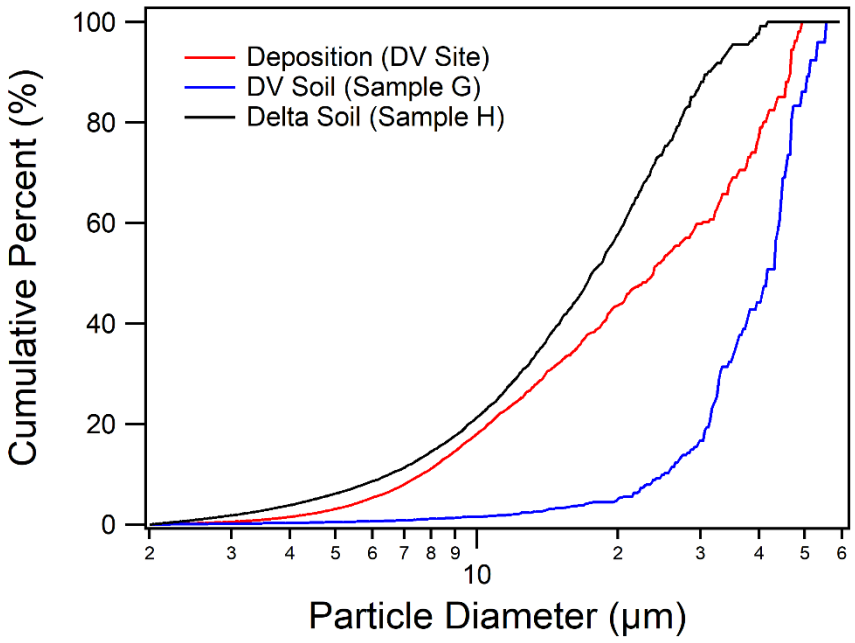

Figure 2-8. Normalized cumulative mass size distribution measured by a Coulter counter. Samples measured include dust deposition at the Down Valley (DV) site, as well as the fine fraction of two soil samples.

Because the saltation/sandblasting mechanism is known to be a dominant dust emission mechanism at previously characterized low-latitude dust sources, we attempted to confirm its importance as a mechanism for dust emissions in the erodible sediment of the Ä'äy Chù Valley. Through the process of sieving our soils we found that the percentage, by mass, of the bulk soil comprising particles smaller than 53 µm in diameter was 12.4 % for a soil sample near the Down Valley site (Sample G), and 14.5 % and 19.6 % for two soil samples collected in the delta, closer to Kluane Lake (Samples I and L, respectively). The results of our size distribution analysis, described in the Supplemental Information section, also demonstrated that the silt fraction ($d < 20$ µm) makes up 50-60 % of the the fine fraction of the soil samples analyzed (Figure 2-8). This demonstrates that the fine fraction of the soils is significant relative to the overall bulk mass of the erodible soils in the dust source, indicating that fine materials are present that could be released in the event that saltation were to occur.

Furthermore, it is highly likely that saltation does occur at this location, as both the measured wind speeds and the calculated shear velocities at the Down Valley site are quite high relative to those previously documented to cause saltation to occur. The average shear velocity

measure over the course of our campaign was 0.61 m/s ± 0.12 m/s, which is well above most thresholds for the emission of dust via the saltation/sandblasting mechanism (Bagnold 1941; Parajuli et al. 2016). We have also analyzed the size-resolved threshold velocity for entrainment. Figure 2-9 provides the comparison between the wind velocities measured at the Down Valley site during the entirety of our dust measurement campaign and the size-resolved threshold velocity for entrainment used by Ginoux et al. (2001). The threshold velocities for entrainment of PM_{10} are surpassed by the recorded wind speeds and the threshold velocities for particles 50 to 100 µm in diameter (particles that dominate in saltation processes) were surpassed throughout the majority of the campaign (56 % of the time for particles 100 µm in diameter or less); both of these results indicate saltation occurred at this location. Finally, the data indicating high shear velocities and significant soil mass within the saltation (fine sand) size range is consistent with the result of Nickling et al. (1978), who measured horizontal flux of particles in the Ä'äy Chù Valley.

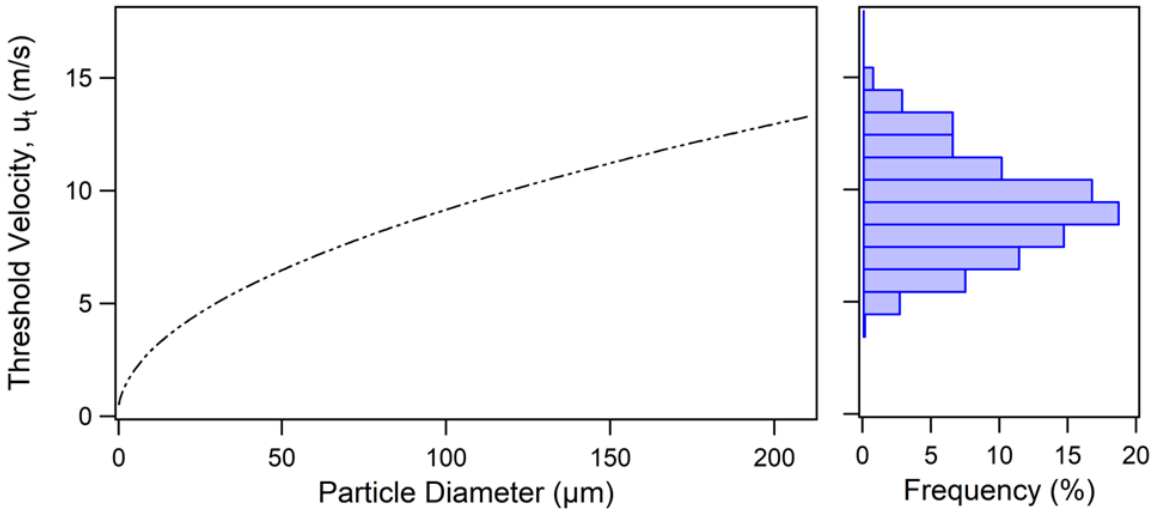

Figure 2-9. (left) Size-resolved threshold wind velocity necessary for dust entrainment, calculated from the parameterization used by Ginoux et al, 2001, which incorporates the physical mechanisms that lead to dust entrainment, including saltation-sandblasting (right) A histogram plot denoting the range of wind speeds calculated at a height of 10 m during May 4 to June 2 at the Down Valley site.

While the occurrence of the sandblasting mechanism is supported by our measurements of shear velocity, and wind speed, as well as the previous study by Nickling et al. (1978), it is noteworthy that the measurements of horizontal flux activity estimated by an installed SENSIT sensor at the Down Valley site did not detect significant saltation during the sampling period (Figure 2-S7), and furthermore the SENSIT detected zero particles during periods of intense dust emissions. Firstly, the observed trends may be a result of the lack of instrumentation sensitivity to the horizontal flux of particles at the Down Valley site. SENSIT instruments possess a limit of detection in terms of the kinetic energy of impact that will be counted as horizontal mass flux of particles (Baas 2004). The lack of saltation recorded during our study may be a result of saltating particles or dissociating aggregates whose impact was below the kinetic energy limit able to be registered by our SENSIT instrument – for example, insufficient momentum possibly stemming from the larger percentage of particles in the mass fraction below 53 μm. Thus, dust emission may have occurred due to sandblasting processes, but due to the limit of detection on our instrument these processes and the fine nature of the soil distribution, the horizontal mass transport may not have been recorded. Regardless of the reason for the lack of particle counts from the SENSIT, we conclude that the majority of the evidence supports the presence of the saltation/sandblasting mechanism and its contribution to the emission of dust from the Ä'äy Chù Valley.

2.5.4.2 Detailed analysis of the saltation-sandblasting mechanism based on particle sizing and elemental composition

We have considered the elemental composition of PM_{10} and soil samples to investigate the detailed saltation/sandblasting dust emission mechanism, as the composition information can serve as a signature of the source material for the PM_{10}. We have chosen to focus on PM_{10} analysis. This is because the results of our dust deposition sampling are much more difficult to interpret, as these samples were collected via passive sampling over several months.

There are four ways through which sandblasting can result in dust emissions, as outlined by Huang et al (2019). First, the release of fine materials through the spalling or chipping of sand grains (defined as particles larger than 50 μm in diameter) is unlikely to be a dominant

mechanism of dust emission, as the elemental composition of the PM_{10} particles collected was distinct from that of the bulk fractions of the soils. Second, the disintegration of clay- and silt-sized particle aggregates upon impact with the surface, or after being impacted by larger sand-sized particles, may release fine particulate matter. If this were a predominant mechanism of dust emissions in the Ä'äy Chù Valley, the PM_{10} elemental composition would reflect that of the fine fraction of the soils. However, this was not the case either. Furthermore, the PM_{10} size distribution measured by the OPC at the Down Valley site is much finer than the particle size distribution predicted by the brittle fragmentation theory developed by Kok, which details the expected particle size distribution of PM_{10} emitted via this emission mechanism (Kok 2011). For these reasons, we conclude that the disintegration of fine particle aggregates is not likely a dominant dust emissions mechanism resulting from saltation-sandblasting.

The third process through which saltation/sandblasting can produce dust is through the rupturing of clay coatings attached to the surface of soil grains. This process corresponds well with both the elemental and mineralogical analyses we have performed in this study, as the SEM/EDS analysis indicated that the majority of the PM_{10} particles were composed of silt-sized clay mineral aggregates. Furthermore, the PM_{10} size distribution measured by the OPC at the Down Valley site is similar to that recorded by the Bullard et al. (2004) study of the release of particulate matter due to the rupture of clay coatings. The Bullard et al. (2004) study found a mode in the volume size distribution between 2.80 μm and 3.29 μm for the diameter of PM_{10} emitted via this mechanism, which fits much more closely with our measured normalized mass size distribution mode at 3.25 μm in diameter in comparison with the size distribution predicted by the Kok (2011) brittle fragmentation theory.

In addition, this would explain the enhancement of trace elements in the PM_{10} samples as compared to the soil samples, both fine and bulk. It is noteworthy that if the enrichment factors were relatively consistent across all elements analyzed, the elevated minor and trace element content in the PM_{10} samples could also be explained by the presence of large silicate particles, such as quartz, which contribute significant mass to the sample relative to their trace element content and can effectively dilute the sample mass fraction. However, the fact that a wide range of enrichment factors were observed further indicates a difference in chemical composition beyond the presence of large silicate particles in the soil samples; juxtaposition of

the elemental enrichment results with the results of Bullard et al. (2004) further supports this conclusion. Moreover, we observed coatings on soil particles using SEM, and we confirmed using EDS analysis that the coating possessed a unique chemical composition as compared with the particle itself (Figure 2-S8), in which the coating clearly contains Mg and Fe, unlike the particle itself. Lastly, the release of resident fine particulate matter trapped within sand particles is another mechanism through which sandblasting can result in the emission of dust; while we are unable to confirm or deny the occurrence of this dust emission mechanism, we note that these particles would need to be have a very different chemical composition as compared to the fine and bulk soils, in order to explain the lack of similarity between the PM_{10} elemental composition and that of both the fine and bulk soils.

2.6 Conclusions

We have successfully characterized dust emissions from the Ä'äy Chù Valley in Yukon, Canada. During our sampling campaign, which took place May 4 to June 2, 2018, we observed a significant dust event on May 19 as well as several smaller dust events during each day of the campaign. Our initial analysis indicates that the PM_{10} originating from the dust source comprises primarily non-spherical aluminosilicate clay mineral aggregates, as well as pure minerals such as quartz, gypsum, calcite, and dolomite. Analysis of the elemental composition of soils (both bulk and fine), dust deposition, and ambient PM_{10} indicate enrichment of trace metal concentration with decreased particle size cut-off, with clear enrichment of PM_{10} as compared to bulk soil samples, and slight enrichment of PM_{10} as compared to dust deposition and the fine fraction ($d < 53$ μm) of soils. Moreover, the 24-hr average concentrations of PM_{10} (near-FRM method) and $PM_{2.5}$ (estimated) at all our sampling sites exceeded the air quality guidelines of the WHO. However, more sampling is needed for a longer period in order to more fully assess the impact on air quality and potential local health risks posed by the mineral dust emitted from the Ä'äy Chù Valley. In addition, we have discussed the physical processes that may dominate in the production of dust from the Ä'äy Chù Valley, and we have highlighted the rupturing of clay mineral coatings and the release of resident fine particulate matter as the two most likely emission mechanisms that take place at

this dust source. This conclusion was based on previous knowledge of the mechanism of dust emission via the extensively studied saltation/sandblasting mechanism, as well as confirmation using our chemical and mineralogical analysis. Our results have demonstrated the value of monitoring dust emissions from the Ä'äy Chù Valley in the Kluane Lake region of Yukon, Canada, and highlight the importance of continued study to elucidate the chemistry and physical mechanisms of dust emissions at this site that functions as an analogue for other high-latitude proglacial dust sources.

2.7 Acknowledgements

We are grateful to Kluane First Nations, the Dän Keyi Renewable Resource Council, and Parks Canada, without whose permission and consultation this work would not have been possible. We also thank James Allen and Shakat Tun Wilderness Camp for allowing us to collect samples of dust deposition on their premises. Many thanks to Sian and Lance Goodwin of Outpost Research Station for going above and beyond the call of duty in providing aid in the field, as well as to Michael Bach, Sarah Butez, Stella Sotorra, Charles Phillips, and Sharpal Singh for volunteering their time to help with the project. Thank you to Jonathan Abbatt of the University of Toronto for kindly allowing us to use his aerodynamic particle sizer. And of course, thanks are due to Donna Sueper of Aerodyne Research, whose code we used to determine diurnal trends in our OPC and net radiometer data. This work was supported by the Université de Montréal, the Natural Science and Engineering Research Council of Canada (Discovery Grant RGPIN-05002- 2014) and the Canada Foundation for Innovation (Leaders Opportunity Fund Project 32277).

2.8 Supplemental Information (Text)

2.8.1 Quality control and data analysis for aerosol sampling instruments

The level of contamination introduced during the handling and transport of the filter samples was determined through analysis of the field blanks for all four air samplers deployed in the field. The average mass on the field blanks was 0.11 mg ± 0.07 mg. The maximum mass of particulate matter recorded on a filter blank was 0.21 mg (found in a blank collected from the

6 m sampler at the DV site), which could introduce an over-estimation of no more than 10 $\mu g/m^3$ into the monitoring of a 24-hour period; this is more than an order of magnitude lower than the typical 24-hour mass concentration recorded by these instruments, and is thus a negligible contribution. Moreover, ICP-MS analysis of field blanks indicated negligible metal concentrations as compared to filter samples, also demonstrating the limited contamination introduced to the filters (see ICP-MS section). For all gravimetric and ICP-MS analyses, measurements were blank-subtracted to account for any contamination.

To assess the accuracy of our OPC measurements, an averaged PM_{10} mass concentration was calculated from the measured particle size distribution for the same periods sampled by our mini-vol samplers at the Down Valley site (Gillies and Berkofsky 2004). An assumed particle density of 2.6 g cm^{-3} was used for this calculation, in accordance with the generally accepted density of mineral dust particles provided in the literature (Tegen and Fung 1994; Yang et al. 2009). The daily mass concentration calculated from the OPC data was well correlated with the mass concentrations determined via gravimetric analysis of both the 6 m and 2 m quartz filters, with R^2 values of 0.963 and 0.918, respectively. We then used the gravimetric data from the Down Valley site 6 m and 2 m samplers to estimate the daily ambient mass concentration of PM_{10} at the height of the OPC (4.5 m), using the method of Gillies et al. (2004). The comparison of the estimated values and OPC output gave an R^2 value of 0.98 and a slope of 1.13 (Supplemental Information, Figure 2-S2); as the ideal slope should be 1.00, we found this to be an acceptable indicator of the validity of the OPC data.

Furthermore, analysis of the variation in particle size distribution with wind speed showed no sampling error due to wind speed-induced biases in the OPC data. In addition, no correction for the refractive index of mineral dust particles was used to modify the OPC data output. This was justified by the fact that clay minerals, which SEM/EDS analysis indicated make up a large portion of ambient PM_{10} at the Down Valley site (see section 2.1), typically have refractive indices that fall in the range of 1.47 to 1.68 (Mukherjee 2013). The refractive index of polystyrene latex spheres (PSL) is included in this range (Smart and Willis 1967), and these were used as a reference to calibrate the OPC by the manufacturer. As a result, it was assumed that the difference between the refractive index of the mineral dust sampled and that of the

PSL calibration standard had a negligible effect on the particle sizing data provided by the OPC.

2.8.2 Comparison of OPC data from 2018 and APS data from 2017

An aerodynamic particle sizer (APS) sampled ambient air outside the Thachal Dhal Visitor's Center from June 13 to June 21, 2017. The instrument was operated at a flow rate of 5 LPM ± 0.2 LPM, with samples taken every minute. The data from the APS indicated the only clear dust event that occurred during the June 2017 sampling period took place from 12:00 to 15:00 on June 19. We applied a Stokes correction to the average particle size distribution measured during this period. The purpose of the Stokes correction was to account for the error introduced into the particle sizing due to deviations of particle densities from the densities of the polystyrene latex particles used by the instrument supplier to calibrate the instrument; these particles have a density of 1.05 g/cm^3, while typical values of the density of mineral dust have been shown to be 2.65 g/cm^3 (Allen and Raabe 1985; Tegen and Fung 1994). The resulting size distribution of the measured aerodynamic diameters are provided in Figure 2-S4. The maximum of this distribution lies at 3.87 μm, which compares well with the maximum optical diameter measured by the OPC in May 2018, which was 3.25 μm.

2.8.3 Calculation of 10-min PM_{10} at 6 m and 2 m at the Down Valley site

Due to the high correlation between the results of the gravimetric analysis of filters from the Down Valley site and the 24-hour calculated OPC data, we calculated the interpolation equation relating the gravimetric and OPC data. The interpolation equations and R^2 values for this analysis can be found in the Supplemental Information section (Figure 2-S3). This analysis allowed us to obtain data at two different heights with a 5-minute timescale.

2.8.4 Method validation for ICP-MS analysis of elemental composition

As our protocol significantly modified Method 3051a, special care was taken to validate the procedure used in this study. Validation tests for the filter sample digestion protocol were completed by digesting 25 mg of a NIST standard together with a quartz filter, using the acid mixture 4 mL HNO_3/1 mL HCl. Soil samples were analyzed using only 3 mL HNO_3/1 mL HCl; the reduction in acid volume was due to the absence of the quartz filter, as this reduces the total sample mass by 0.14 g. Thus, this procedure was validated by digesting 25 mg of NIST standard using the acid mixture 3 mL HNO_3/1 mL HCl. Three standards supplied by NIST were used for the validation tests: Montana I Soil with Highly Elevated Trace Element Concentrations (NIST 2710a), Montana II Soil with Moderately Elevated Trace Element Concentrations (NIST 2711a), and Buffalo River Sediment (NIST 8704).

The percent recoveries of the NIST standards subjected to the digestion conditions used to digest soil and filter samples are provided in the Supplemental Information section (Table 2-S2). For both soil and filter samples, the percent recoveries of these metals fell within an acceptable range of 80 to 110 %. Furthermore, analysis of filter blanks obtained in the field showed negligible concentrations of the metals quantified. The results of the field blank limit of detection (LOD), calculated as three times the standard deviation of the blank divided by the slope of the calibration curve, compared to the concentrations found in select filter samples can be found in Table 2-S3.

There are several advantages to the technique we have employed, as we have avoided the use of highly hazardous materials, such as HF, which is typically used to digest samples of low mass (e.g. less than 50 mg). Furthermore, we have extracted several key elements that are crucial to the characterization of dust emitted from the Ä'äy Chù Valley, notably Fe and As. However, as neither HNO_3 nor HNO_3/HCl can completely digest the aluminosilicate matrix, there were several important metals that we were not able to quantitatively extract from our samples. These include Na, Mg, Al, K, and Ca, all of which can impact primary ecological productivity and can be related to the mineralogy of air and soil samples through the calculation of elemental ratios. Future work will focus on expanding the number of elements quantified in samples collected in the Ä'äy Chù valley

2.8.5 Coulter counter analysis of deposition and fine soils

Both soil and deposition samples were sieved to select the size fraction smaller than 53 μm in diameter. This fraction of the soils was then analyzed by a Coulter counter using a 100 μm aperture, in order to obtain the size distribution of the particles in these samples. The fine fractions of two soil samples were analyzed (Samples G and H), as well as the June to August 2018 deposition collected at the Down Valley site.

2.8.6 Calculation of the size-resolved threshold velocity for particle entrainment

The size-resolved threshold wind velocity for dust emission was calculated using the method employed by Ginoux et al. when parameterizing vertical aerosol flux for the Global Ozone Chemistry Aerosol Radiation and Transport (GOCART) chemical transport model (Ginoux et al. 2001). Equation (2-4) gives this parameterization, where u_t is the threshold wind velocity, A is a dimensionless parameter of 6.5, $\Phi$is the particle diameter, g is acceleration due to gravity, ρ_a is air density, ρ_p is particle density, and w is soil moisture. Note that this equation is only valid for soil moisture values less than 0.5 (ratio by volume of moisture to soil); the typical soil moisture measured during our campaign was 0.05, which is well below this limit.

$$u_t = A\sqrt{\Phi g \frac{\rho_a - \rho_p}{\rho_a}}(1.2 + 0.2\log_{10} w) \qquad (2\text{-}4)$$

2.8.7 Comparison of vertical aerosol flux and saltation measurements

We have compared the output of our SENSIT horizontal mass flux monitor with the ambient concentrations of PM_{10} obtained through our gravimetric analysis and OPC data, and have

provided two examples of this comparison performed on May 19 and 24 (Figure 2-S7). The 10-min resolved PM_{10} concentrations at 6 m and 2 m were extrapolated based on the OPC data (Supplemental Information, Figure 2-S5). The results show very little correlation between the SENSIT data and ambient dust, with dust observed almost the entire 24-hour period on both days and very little horizontal mass flux recorded. While these are just two examples pulled from the entirety of our sampling period, there were no dust events that occurred which showed correlation between horizontal mass flux and ambient PM_{10}.

2.9 Supplemental Information (Figures)

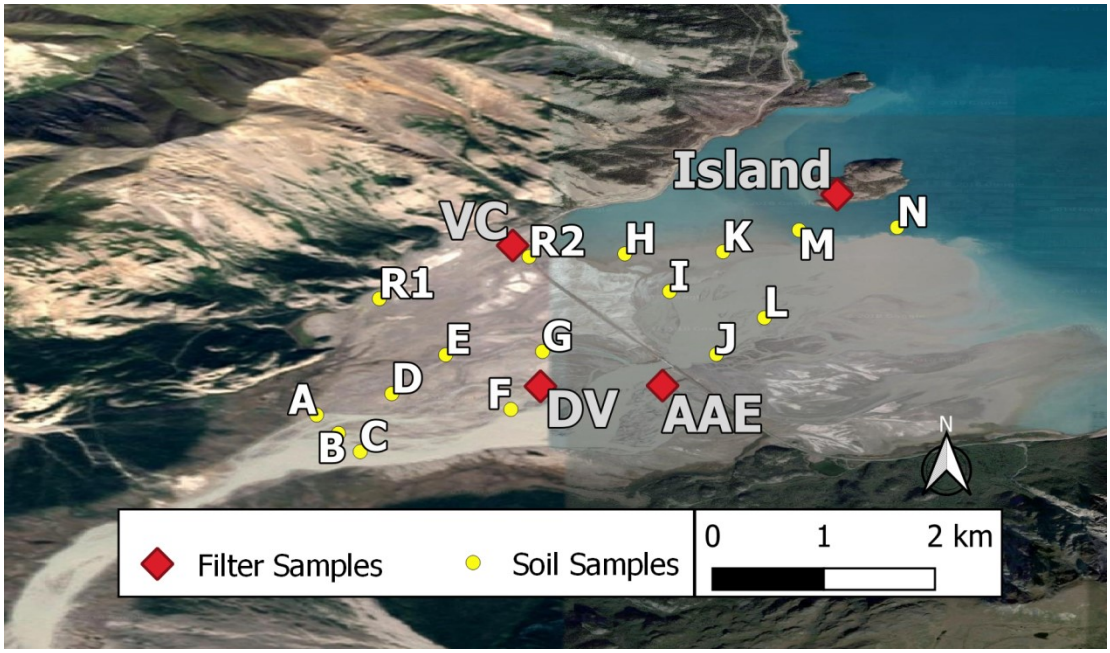

Figure 2-S1. Map of soil sampling locations. Samples A to N were taken from the Ä'äy Chù Valley and Delta, while sample R1 was well removed from the valley and R2 is a roadside sample retrieved near the Alaska Highway. For reference, the location of the four air sampling locations have been included: the Down Valley site (DV), Ä'äy Chù East (AAE), the Visitor's Center (VC), and the Island.

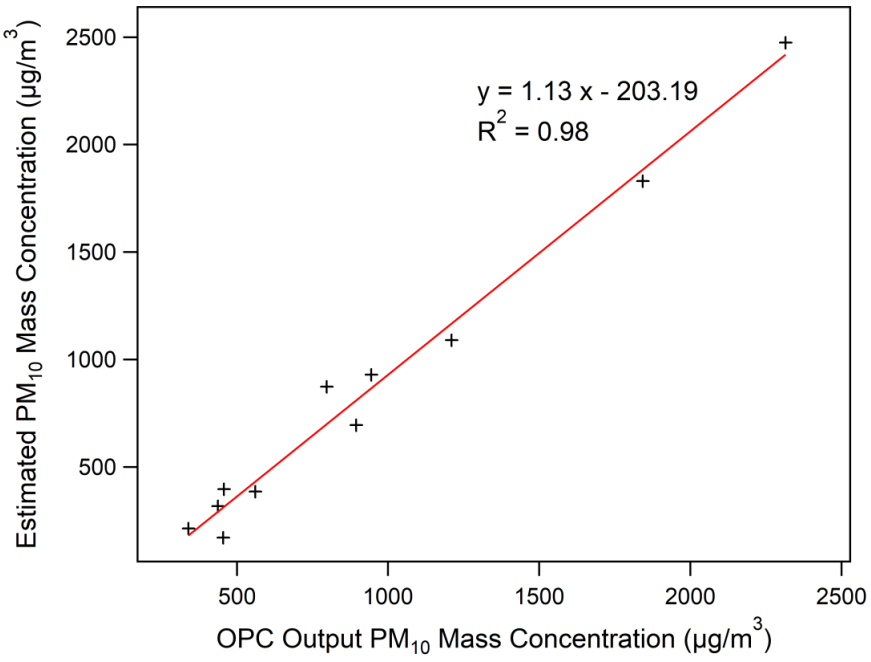

Figure 2-S2. Comparison of ambient PM_{10} mass concentrations measured by the OPC (x-axis) with concentration values interpolated at the OPC height based on gravimetric data (y-axis). This analysis was based on the work of Gillies et al. 2004.

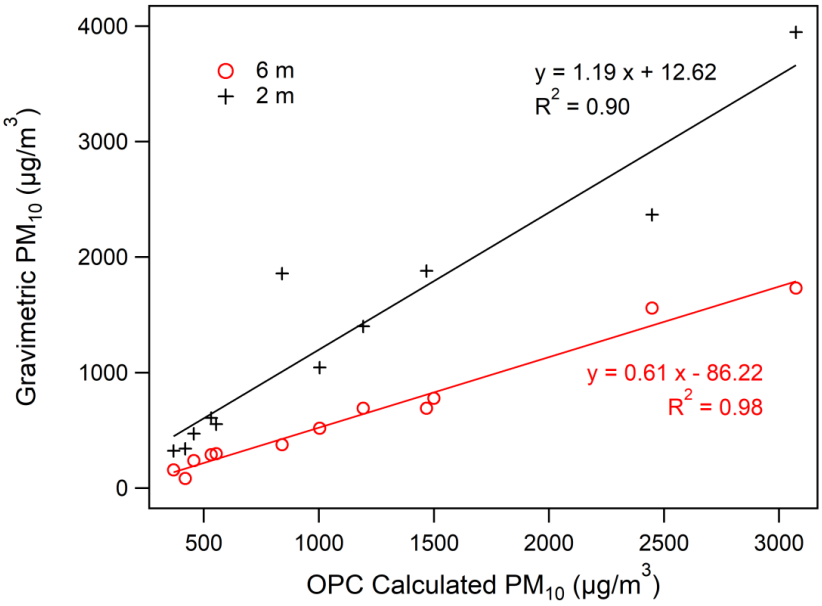

Figure 2-S3. Correlation between 6 m and 2 m gravimetric data and 24-hour averaged PM_{10} calculated from the OPC data. Interpolation equations and R^2 values are provided in the image.

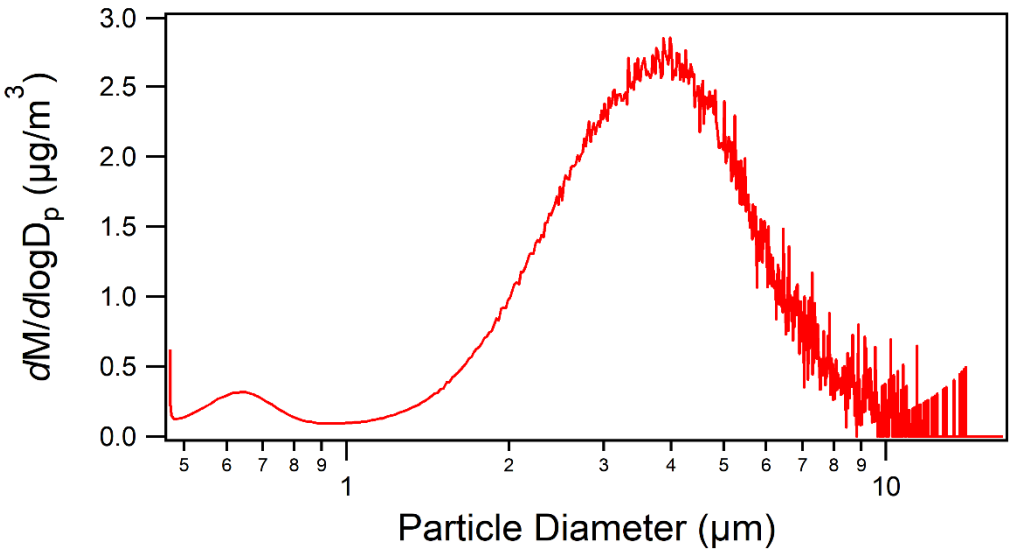

Figure 2-S4. Results of the Stokes-corrected output of aerodynamic particle sizer (APS) measurements obtained on June 19, 2017 at the Thachäl Dhäl Visitor's Center. Maximum at a particle diameter of 3.87 µm.

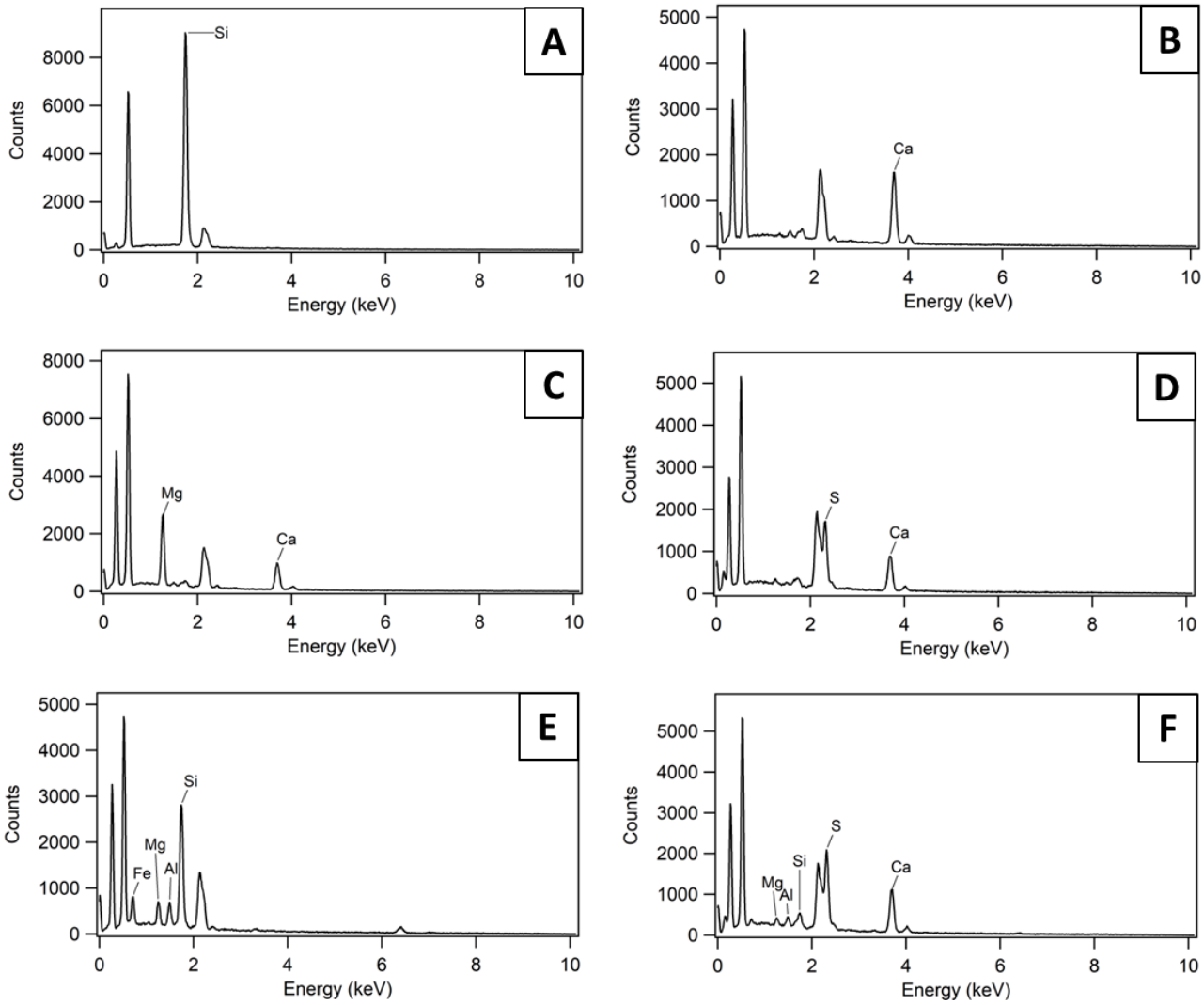

Figure 2-S5. EDS spectra of individual mineral dust particles. (a) pure quartz, (b) pure calcite, (c) dolomite, (d) gypsum, (e) clay mineral aggregate, (f) clay-gypsum aggregate. Note (d) is attributed to gypsum even though the S-Ca ratio is slightly higher than 1:1, as it was reasoned that the increased S peak size was due to partial overlap of the S and Au peaks. C, O, and Au peaks are not labeled.

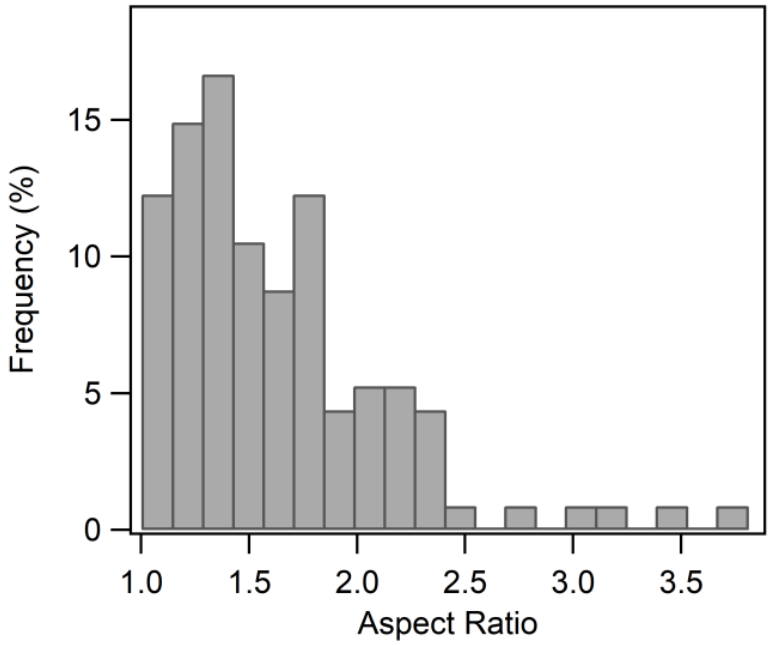

Figure 2-S6. Particle aspect ratios as determined by SEM/EDS analysis.

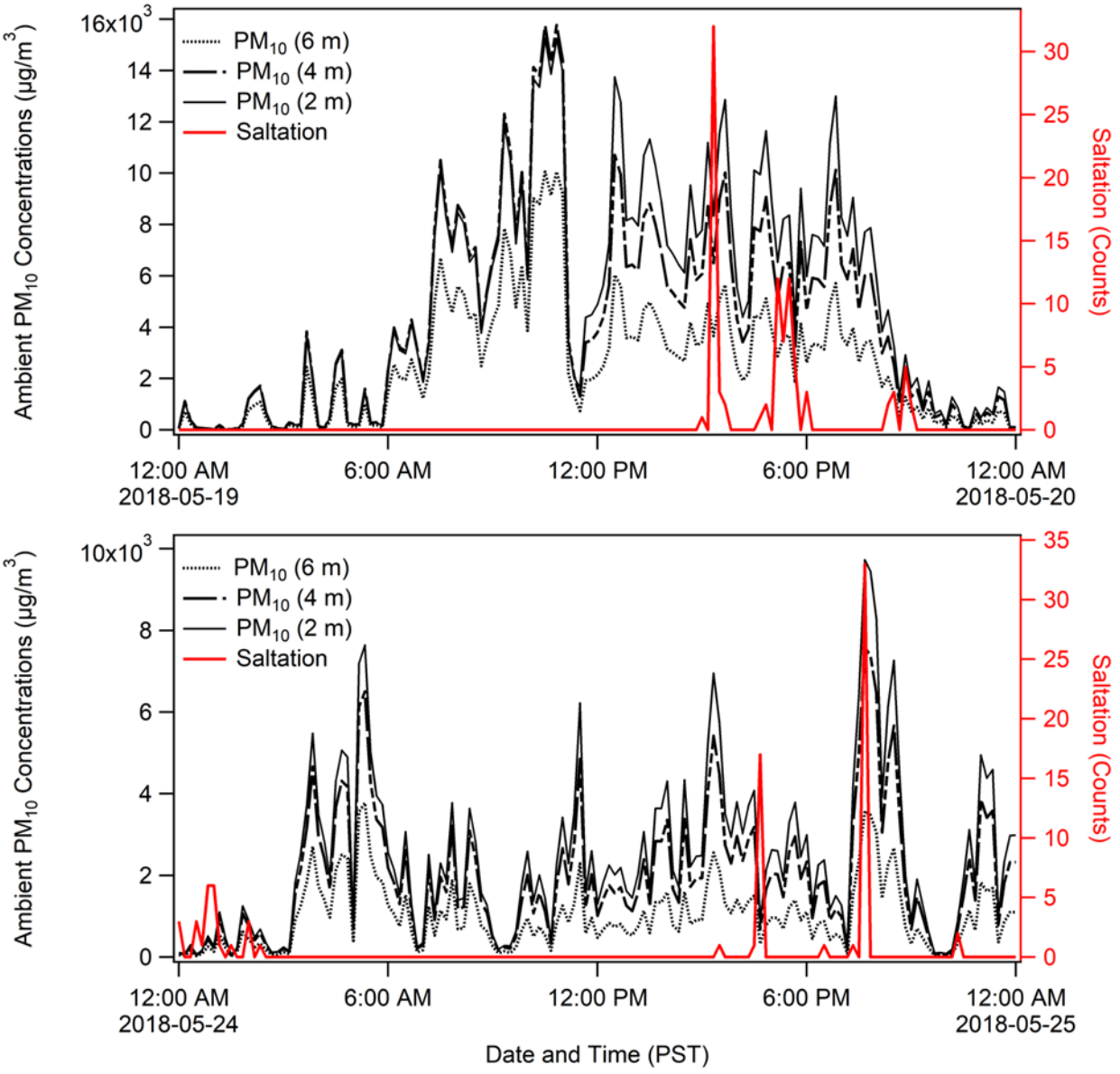

Figure 2-S7. Down Valley site ambient PM_{10} concentrations and saltation during dust events on (A) May 19 and (B) May 24.

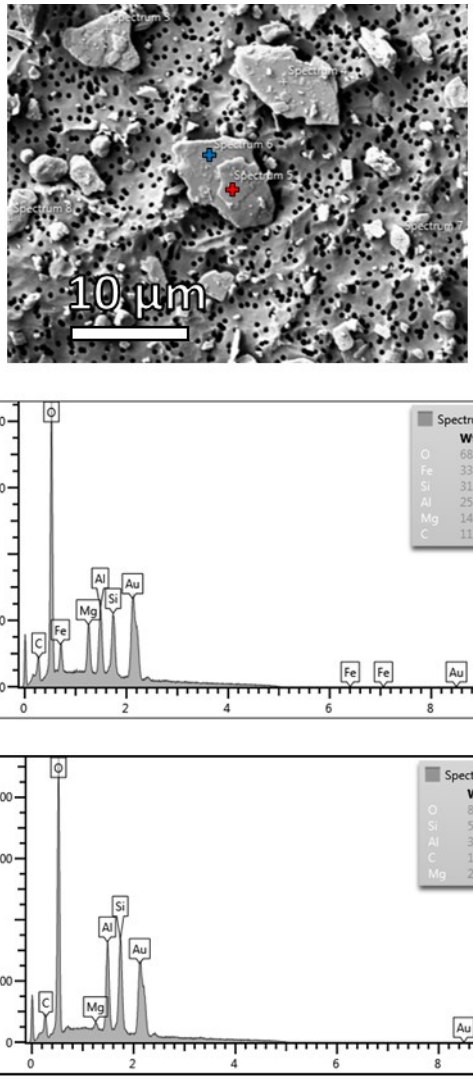

Figure 2-S8. SEM image of a soil particles collected from the river delta; one particle is clearly coated by a layer of clay. EDS analysis of the points with the coating (red cross, spectrum 5) and without (blue cross, spectrum 6) demonstrate a difference in the chemical composition between the particle and its coating.

2.10 Supplmental Information (Tables)

Meteorological Equipment	Manufacturer	Model Name	Height (m)
Soil Volumetric Water Content Sensor (Soil Moisture)	Campbell Scientific	CS616	-0.05, -0.10
Saltation	Sensit	H14-LIN	0.0
Anemometer 1	NRG	40C	0.3
Anemomenter 2	NRG	40C	0.5
Anemomenter 3	NRG	40C	0.9
Net Radiometer	Biomet	CNR4	1.4
Humidity, Temperature Sensor	Campbell Scientific	CS215	1.5
Anemomenter 4	NRG	40C	1.7
PM_{10} Sampler (Quartz Filter)	ARA Instruments	N-FRM Sampler	2.6
Humidity, Temperature Sensor	Campbell Scientific	CS215	3.0
Sonic Anemomenter	Campbell Scientific	CSAT 3B	3.5
Optical Particle Counter	FAI Instruments		3.5
PM_{10} Sampler (Quartz Filter)	ARA Instruments	N-FRM Sampler	5.9
Anemomenter 5	NRG	40C	6.0
PM_{10} Sampler (Nuclepore Filter)	ARA Instruments	N-FRM Sampler	6.1

Table 2-S1. Down Valley Site meteorological monitoring instrument details.

Digestion Condition	% Recovery								
	^{55}Mn	^{57}Fe	^{59}Co	^{60}Ni	^{63}Cu	^{75}As	^{111}Cd	^{133}Cs	^{208}Pb
Filter Sample Analysis Validation: 4 mL HNO3 + 1 mL HCl + Filter									
NIST 2710a	86.3	90.7	92.7		98.7	94.8	99.4	83.1	92.9
NIST 2711a	80.5	84.4	106.8	84.9	97.3	88.1	100.2	75.1	104.4
NIST 8704	88.0	84.0		84.5			105.3	70.6	93.9
Soil Sample Analysis Validation: 3 mL HNO3 + 1 mL HCl + No Filter									
NIST 2710a	83.8	90.2	102.8		107.6	103.9	103.2	92.2	84.7
NIST 2711a	81.3	86.6	104.4	84.6	103.5	98.1	105.6	89.0	98.2
NIST 8704	94.0	90.5		96.3			100.2	90.4	90.2

Table 2-S2. Percent recoveries of NIST standards digested to validate the quantitative nature of the protocol employed for soil and filter sample analysis. Missing values indicate that the element in question is not present in the standard reference material digested.

	VC Blank LOD (μg/L)	VC , May 20 (μg/L)	DV Blank LOD (μg/L)	DV, May 29 (μg/L)
^{55}Mn	0.05	11.15	0.01	37.44
^{57}Fe	0.57	728.67	1.93	2493.93
^{59}Co	0.12	0.51	1.66×10^{-3}	1.37
^{60}Ni	0.18	1.23	0.02	4.24
^{63}Cu	0.19	1.21	0.06	4.32
^{75}As	0.17	0.22	0.37	1.11
^{111}Cd	4.00×10^{-3}	0.03	0.01	0.07
^{113}Cs	0.00	0.03	0.00	0.08
^{208}Pb	0.04	0.36	3.02×10^{-3}	0.93

Table 2-S3. Limit of detection (LOD) of the Visitor's Center (VC) and Down Valley Site (DV) field blank as compared to the solution-phase elemental concentrations of the May 20 filter sample collected at the VC Site and the May 29 filter collected from a height of 6 m at the DV site.

Time Period	Average Vertical Aerosol Flux (μg/m^2/s)
May 15 9:46 to May 16 6:22	204.9
May 16 6:23 to May 17 10:38	91.1
May 17 10:39 to May 18 10:26	39.7
May 18 10:27 to May 19 11:34	42.7
May 19 11:35 to May 20 9:30	708.4
May 20 9:31 to May 21 9:50	74.2
May 21 9:51 to May 22 9:20	115.5
May 22 9:21 to May 23 10:31	
May 23 10:32 to May 24 9:35	
May 24 9:36 to May 25 9:38	173.3
May 25 9:39 to May 26 9:48	50.0
May 26 9:49 to May 27 10:15	29.6
May 27 10:16 to May 28 8:20	19.2
May 28 8:21 to May 29 9:30	244.3
May 29 9:31 to May 30 9:29	-50.8

Table 2-S4. Tabulated average daily vertical aerosol flux calculated from gravimetric data at the Down Valley site, using the method of Gillette et al. (1972). Positive values indicate net emissions, while negative values indicate net dust deposition during the filter sampling period. The overall average value of vertical flux measured during our sampling campaign, including standard error, was found to be 134.0 ± 52.9 (μg/m^2/s)

Chapter 3 – Supplemental Analyses

3.1 APS data collected from the Ä'äy Chù Valley in June 2017

An APS sampled ambient air outside the Thachal Dhal Visitor's Center from June 13 to June 21, 2017. The instrument was operated at a flow rate of 5 LPM ± 0.2 LPM, with samples taken every minute. The APS setup at the Visitor's Center can be found in Figure 3-S1.

All APS data analysis was performed using IGOR Pro, and can be found in Section F of the Annex. The data from the APS indicated that, during the June 2017 sampling period, the only dust event whose emissions were above the detection limit of the instrument at the location of the Visitor's Center took place from 12:00 to 15:00 on June 19, 2017; the instrument output from this event can be found in Figure 3-S2. Photos taken of the Ä'äy Chù Valley confirm that dust was produced during this period (Figure 3-S3). The APS data indicated that both fine and coarse particles were present in the ambient air sampled at the Visitor's Center, and that ambient concentrations of particulate matter decreased significantly at 15:00 on June 19, remaining negligible for the rest of the day.

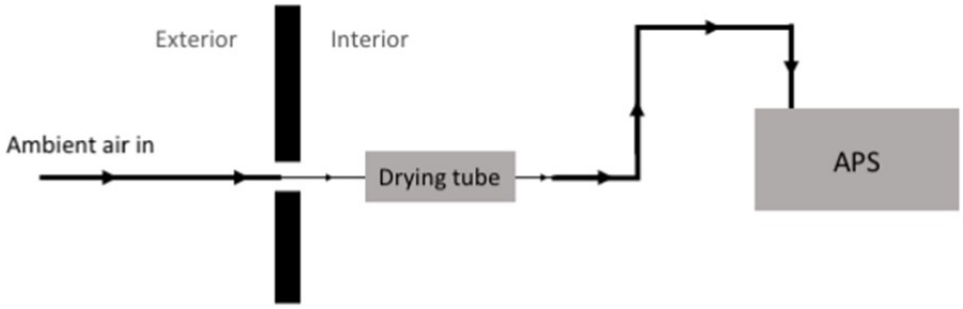

Figure 3-S1. (A) Image of the aerodynamic particle sizer (APS) situated in the shed of the Visitor's Center near Kluane Lake, with tubing passing from the exterior of the shed into the instrument inlet. (B) Schematic of the APS sampling scheme, denoting the process of sampling and drying ambient air from the exterior before analysis by the instrument.

In addition to particle size, the APS measures the side scatter intensity, which is a parameter related to the granularity and composition of particulate matter. Figure 3-S4 depicts the integrated side scatter intensity plotted against the integrated particle mass concentrations found by the APS. This plot shows a clear difference in the ratio of side scatter intensity to integrated particle mass during the period of 12:00 to 15:00 on June 19, when the dust event was observed, indicating unique granularity and composition of the particles sampled during this period as compared to the background concentrations of ambient particles sampled when there was no dust observed. Thus, analysis of the side scatter intensity is further indication that, not only did a dust event occur during this period, but that the particles emitted during the event were unique in their granularity and composition as compared to the background particles.

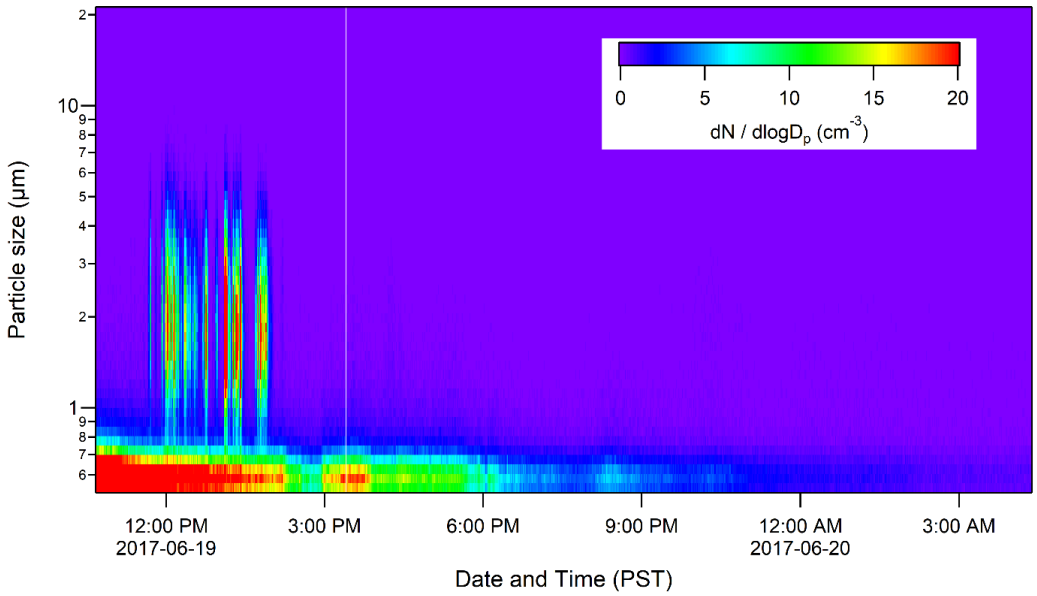

Figure 3-S2. Normalized particle size distribution measured by an APS at the Thachal Dhal Visitor's center on June 19, 2017.

Finally, the error of the APS data was evaluated by applying a Stokes correction and observing the subsequent effect on the particle size distribution output by the instrument, as per instructions from the Aerosol Instruments Manager software manual (TSI 2013). The purpose of the Stokes correction was to account for the error introduced into the particle sizing due to

deviations of particle densities from the densities of the polystyrene latex particles used by the instrument supplier to calibrate the instrument; these particles have a density of 1.05 g/cm^3, while typical values of the density of mineral dust have been shown to be 2.65 g/cm^3 (Allen and Raabe 1985; Tegen and Fung 1994). A value of 1.60 g/cm^3 was also tested, as this is the average density of PM_{10} determined from the analysis of predominantly organic aerosols (Hu et al. 2012). The results of the Stokes correction are provided in Figure 3-S5. The applied Stokes correction clearly indicates an over-estimation of particle sizing occurs when the particle density is assumed to be 1.05 g/cm^3 as compared to when a density of 2.65 g/cm^3 is used.

Figure 3-S3. Photographic evidence obtained by the Island camera station on June 19, 2017 at 12:20 PST, confirming dust emissions occurred during the measurement period of the APS. Dust has been circled in red.

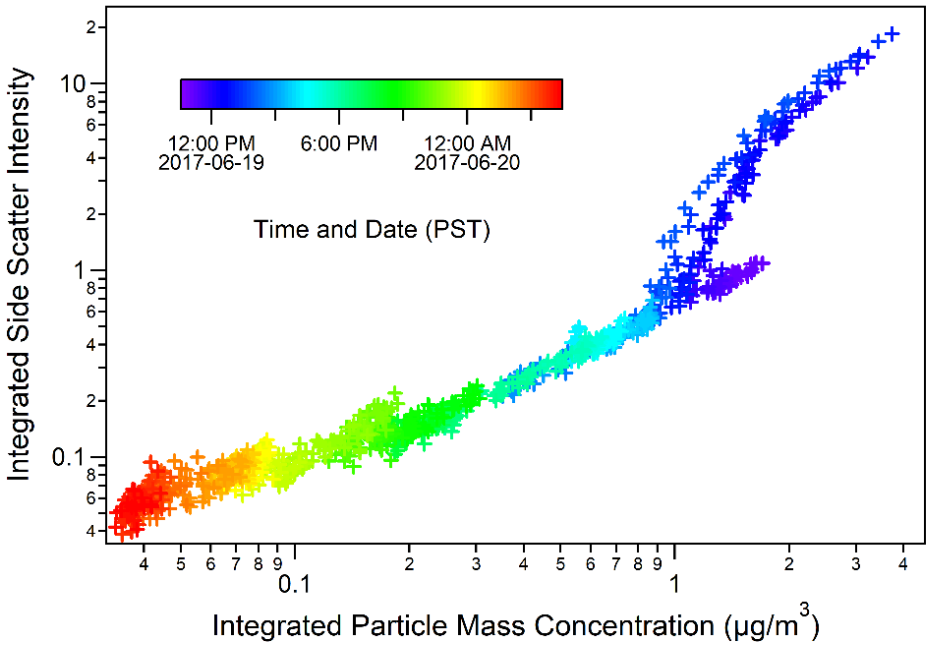

Figure 3-S4. Correlation plot relating the integrated side scatter and particle mass concentrations for a time period that includes a known dust event on June 19, 2017. The correlation plot clearly shows an altered scatter-to-mass ratio (indicated by the overall slope of the correlation plot) for the times during which dust was observed, indicating a difference in the granularity of ambient dust with the background aerosol species. The presence of multiple trends with different slopes in the concentration range of 1-2 µg/m^3 indicates that at different points in the sampling period, for similar concentrations of ambient particulate matter in this size range, the granularity – and thus, particle composition – was not the same.

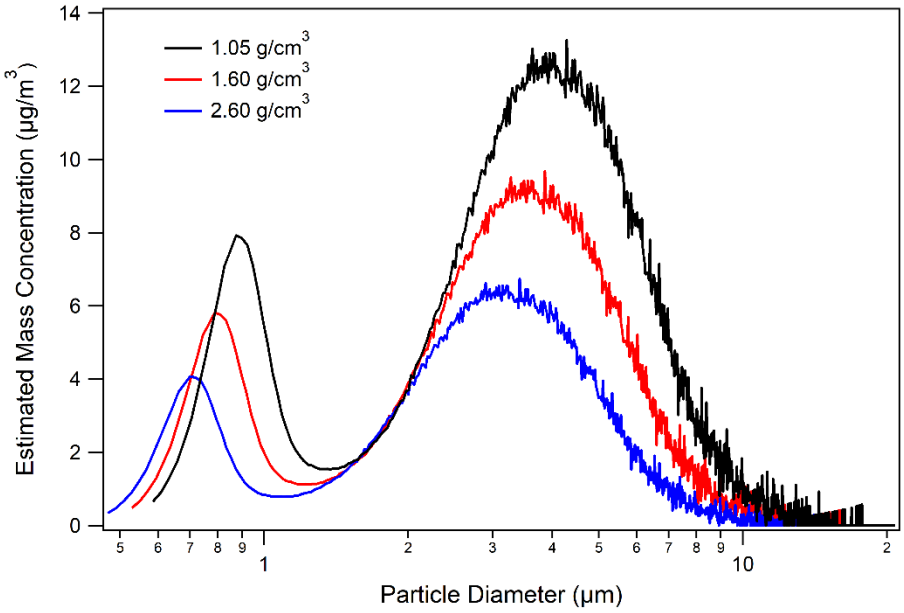

Figure 3-S5. Results of the particle size distribution measured by the APS on June 19, 2017, with and without the application of a Stokes correction. Densities employed for the Stokes correction calculations were 1.05 g/cm^3, as this is the density of polystyrene latex spheres which are used for calibration of the instrument; 1.60 g/cm^3, a typical average value of PM_{10}; and 2.65 g/cm^3, the density of mineral dust. All estimated mass concentrations were calculated assuming a density of 2.65 g/cm^3 regardless of which density was used for the Stokes correction calculation, as this is the density of mineral dust, which was thought to dominate in large part the sample composition due to the proximity of the site to the dust emission source.

3.2 LA-ICP-MS microanalysis of mineral dust particles

The procedure employed for LA-ICP-MS analysis is as follows. An Attom high-resolution ICP-MS instrument was used, set to perform the lowest resolution analysis possible to increase sample throughput. A Ni sampler cone (Nu Instruments, 0.9 mm hole, screw in, FB9) and skimmer (Nu Instruments, Ni WA7 Skimmer cone) meant for the analysis of dry samples were installed in the ICP-MS prior to analysis. The spectrometer was turned on and allowed to warm up for 20 minutes before the analysis took place, after which it was rinsed using 1 % (v/v) HNO_3 for five minutes followed by a rinse with MilliQ water for five minutes. Optimization of the ICP-MS was first performed using a tune solution (provided by Nu Instruments) introduced through the nebulisation system. The peak shape of ^{115}In was used as

an indicator for the optimization of the instrument, and parameters such as nebuliser gas flow rate, plasma torch position, and components of the ion optics system were modified until the peak of ^{115}In showed a symmetrical and smooth shape with an intensity above 10^5 counts per second.

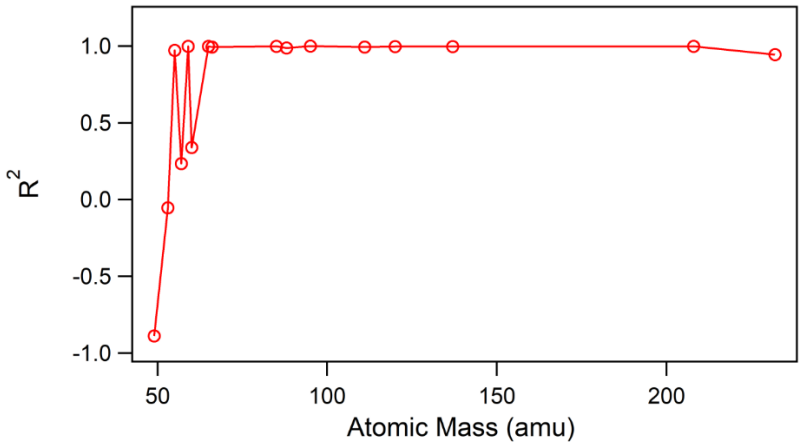

Figure 3-S6. Analysis of the R^2 values of the calibration curves generated from gas blanks, NIST 612, and NIST 610 standard reference materials. Elements with R^2 values below 0.5 were Ti, Cr, Fe, and Ni. Laser ablation was completed on September 15, 2017 using 17 % laser power and a 10 µm diameter spot size.

After solution-phase optimization, the nebuliser was detached from the instrument and replaced by tubing leading from the laser ablation unit (Applied Spectra, J200, 266 nm Nd :YAG laser). The average laser power of the 266 nm Nd :YAG laser in the instrument was calculated by Madjid Hadioui to be approximately 90 mW (Hadioui 2018). In order to avoid the recurring problem of the ICP shutting down upon attachment of the laser ablation unit, the gas flow (0.7 LPM He/0.7 LPM Ar) of the laser ablation unit was turned on prior to attachment to the ICP-MS. In addition, prior to the analysis of all samples, gases within the chamber were purged to avoid the presence of ambient air in the ablation chamber. Two standard reference materials provided by the National Institute of Standards and Technology – NIST 612 and NIST 610 – were inserted into the ablation chamber, and the optimization procedure previously performed using the ^{115}In peak was repeated by ablating NIST 612 and using the peak of ^{238}U.

	R^2	LOD (ppm)
^{49}Ti	-0.887	N/A
^{53}Cr	-0.053	N/A
^{55}Mn	0.972	13.91
^{57}Fe	0.235	465.00
^{59}Co	0.998	2.13
^{60}Ni	0.339	123.24
^{65}Cu	0.999	12.55
^{66}Zn	0.994	8.83
^{85}Rb	0.999	4.32
^{88}Sr	0.987	9.30
^{95}Mo	1.000	6.98
^{111}Cd	0.994	18.07
^{120}Sn	0.997	4.26
^{137}Ba	0.997	3.68
^{208}Pb	0.999	1.72
^{232}Th	0.944	0.03

Table 3-S1. R^2 and limit of detection (LOD) values for the analysis depicted in Figure 3-S6.

Once optimization was complete, NIST 612 and NIST 610 were employed in the generation of a calibration curve. Firstly, a gas blank was obtained by performing ICP-MS analysis while the laser ablation system was online, but no ablation was occurring. Next, an area in a fresh, not previously ablated portion of the NIST 612 standard was located, and a spot in this area was ablated for 45 s. ICP-MS analysis was delayed for 15 s after the start of ablation in order to ensure the sample had reached the instrument. This procedure was repeated using NIST 610.

The laser power was optimized by generating several calibration curves from the NIST 612 and 610 glass standards, each curve with a varied laser power. These tests were performed using a beam width of 10 μm, as this was the smallest beam width setting available on the laser ablation instrument's Axiom user interface software. It is noteworthy that no validation tests were performed to confirm the spot size of the ablation crater after firing, as the Axiom software microscope imagery did not possess enough resolution to clearly see the ablation crater on the NIST standard, and we did not have the capabilities to verify the spot size using other microscopy techniques. Furthermore, a laser power greater than 20 % was not able to be used, as this was observed to ablate soil particles too quickly and to generate large aerosol particles that could be harmful if introduced into the ICP-MS instrument. The results of our optimization tests can be found in Figure 3-S6 and Table 3-S1. For elements not certified by NIST but still contained within the NIST standard, we used the elemental mass fraction values published elsewhere to complete the calibration curve (Pearce et al. 1997). In the end, a beam width of 10 μm and a laser power of 10 % were used for microanalysis (single-spot laser ablation), thus these were the conditions employed in the ablation of the standard reference materials and samples during both calibration and analyses.

We chose to begin by analyzing soils collected by Dr. James King, our collaborator from the Department of Geography, from the exposed sediment of the Ä'äy Chù in May 2017, as we only collected very limited ambient PM_{10} samples during our first mineral dust sampling campaign in June 2017. Samples were mounted adhesively, by placing a small portion of soils in a clean petri dish and pressing the adhesive side of a clean piece of Scotch tape into the soils. Another piece of tape was then used to remove particles that were not securely attached to the tape in order to avoid the possibility of particles becoming detached and directly entering the ICP-MS in the absence of ablation. An image taken by the Axiom user interface software of the samples after mounting can be found in Figure 3-S7a, while images of a particle being ablated can be found in Figure 3-S7b,c.

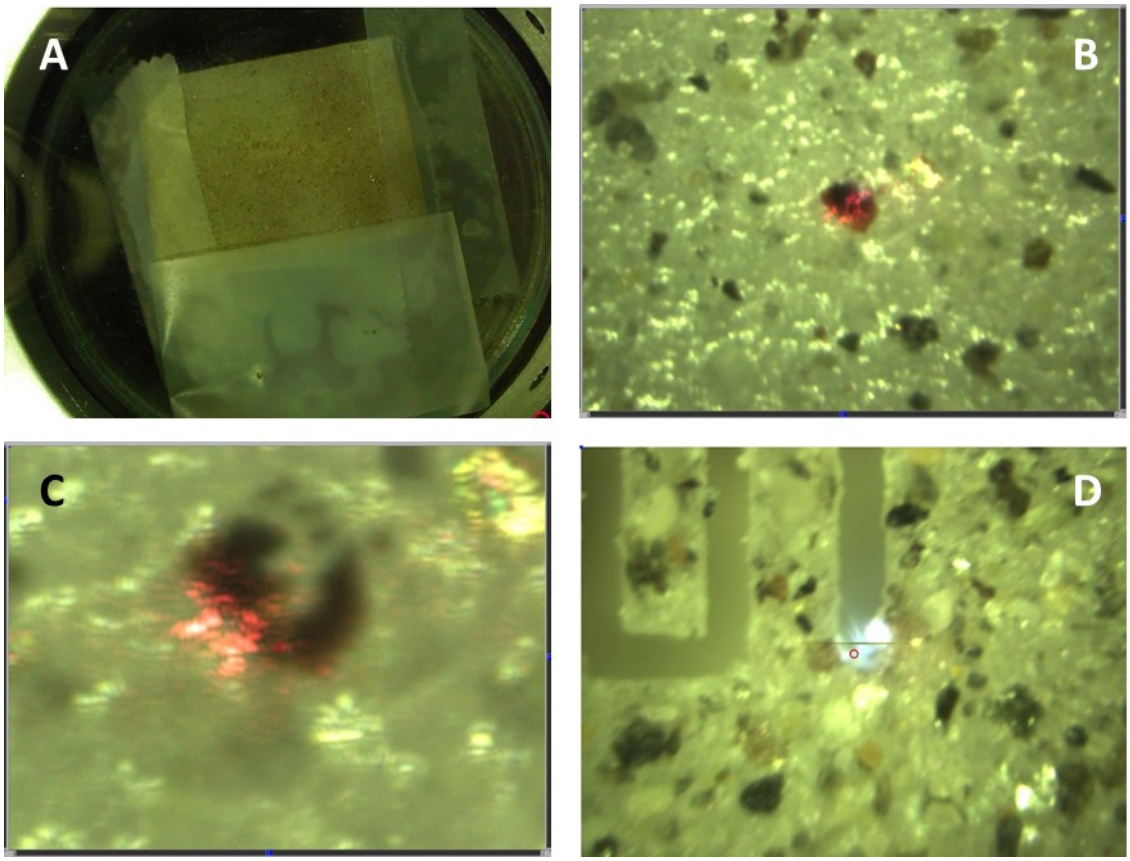

Figure 3-S7. (a) Soil sample mounted and introduced into the ablation chamber. (b) Microanalysis of an individual soil particle; photo was taken as ablation was taking place. (c) The same soil particle after ablation took place. (d) Pattern used during bulk analysis of soils.

As individual particles are ablated in a relatively short period of time, the ICP-MS analysis must be completed within a period of seconds during which the sample aerosol mass passes through the mass spectrometer. To determine the proper timing of analysis, ablation of individual soil particles was completed using time-resolved single-particle analysis mode, which revealed that it takes 5 s after the start of ablation for the sample to reach the ICP-MS, and typically 5 s for a chosen spot to be completely ablated through. Thus, the analysis must take place very quickly and can only be completed for very few elements per particle analyzed. Because a magnetic sector instrument was employed, elements of similar masses were chosen to decrease the time spent by the instrument scanning between elemental masses.

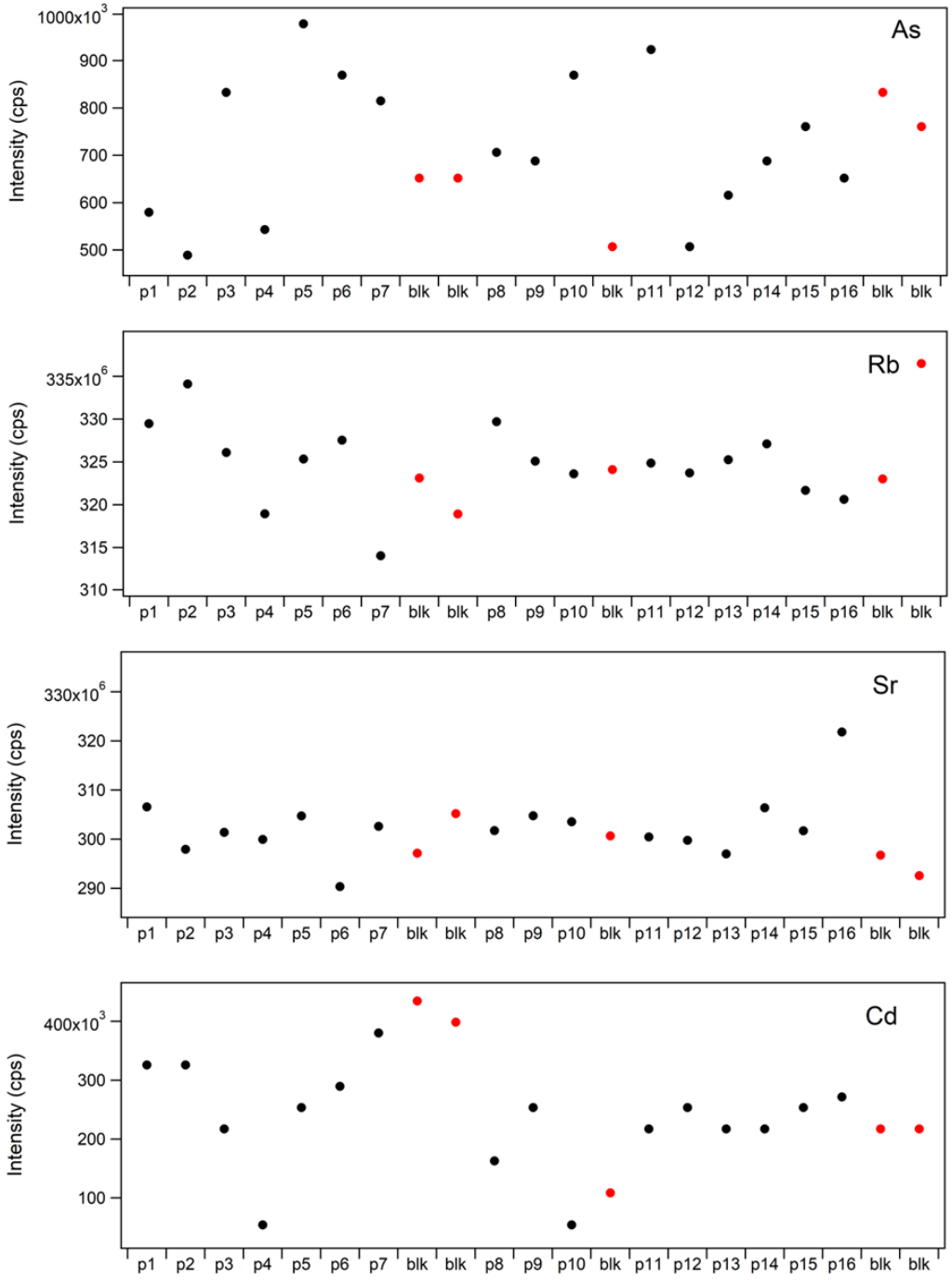

Figure 3-S8a. Microanalysis of soil particles, with only particles smaller than 10 µm in diameter targeted. The results for four metals (As, Rb, Sr, and Cd) are provided, with gas blanks highlighted by red markers while particle analyses are in black. « Blk » indicates gas blanks, while « p » indicates the particle number.

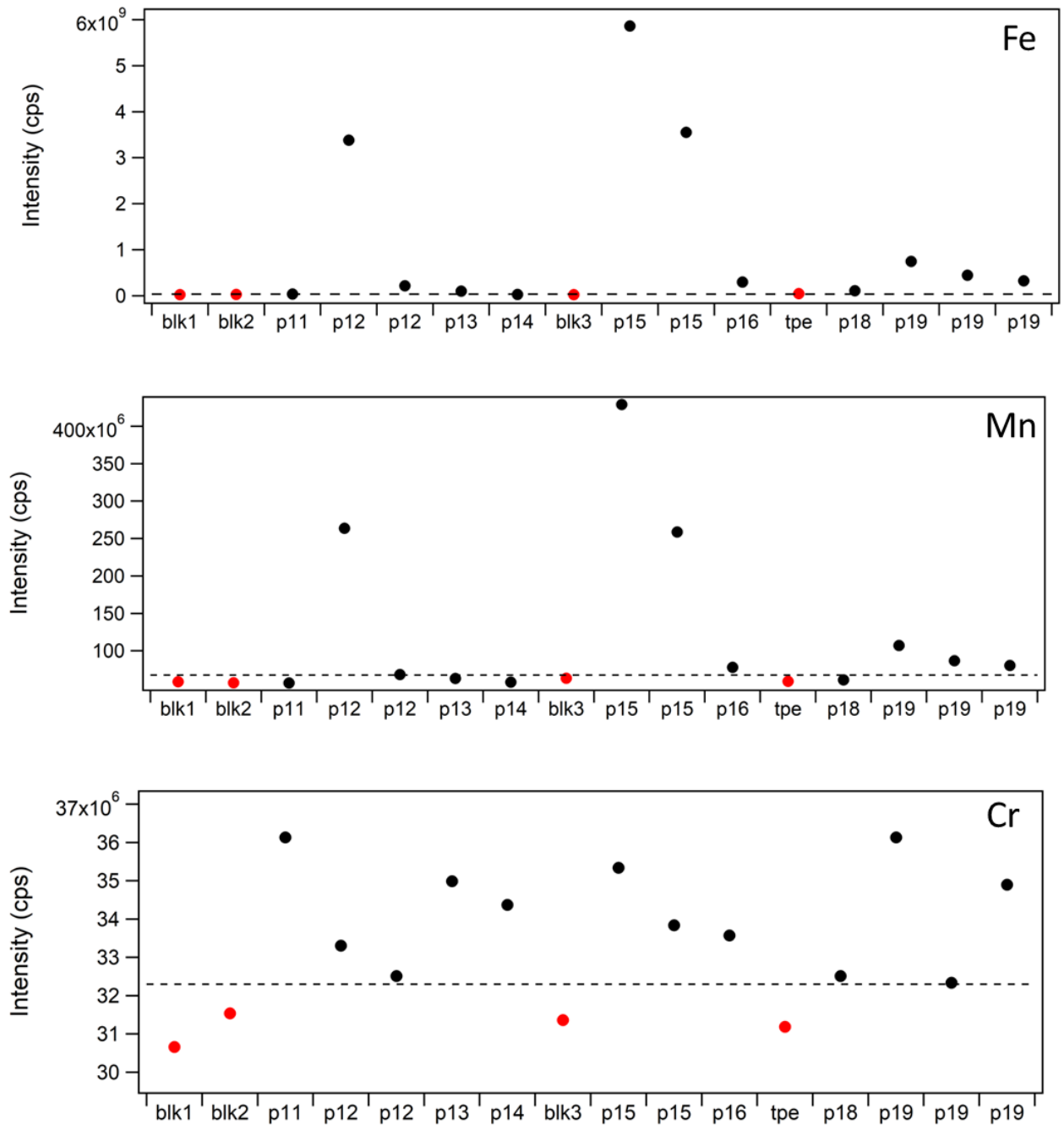

Figure 3-S8b. Microanalysis of soil particles, with the intensity of peaks of As, Mn, and Cr provided. Blanks are highlighted by red markers ("blk" indicates gas blanks, "tpe" indicates tape blanks) while particle analyses are in black. Dotted black lines indicate the limit of detection calculated from the intensities of the blank replicates.

It was quickly found that the setup used in this study was not suitable for microanalysis of PM_{10}. During analyses where PM_{10} particles were specifically targeted, the gas blanks provided intensities that were higher than those of the sample. The example of As, Rb, Sr, and Cd is given in Figure 3-S8a. As the variation in the gas blank intensities demonstrated a similar range and intensity as the analyses of particles, it was concluded that no signal from the PM_{10} particles targeted had been obtained. Possible explanations for this were the speed of ablation per particle, which may have been too fast to allow for detection using this method; the laser beam width, which may have been larger than the particles; the aim of the microscope, which may not have been accurate enough to aim at particles as small as PM_{10}; or due to technical issues with the ICP-MS, such as improper optimization. Furthermore, the sensitivity of the technique was lower due to the infeasibility of using Si or Ca as an internal standard, as is typically done in LA-ICP-MS of geological samples to overcome the error introduced by elemental fractionation and matrix effects. In order to use an internal standard, the concentration of the reference element must be known, and due to the infeasibility of using microscopy to quantify Si or Ca in all particles analyzed, we were unable to use these elements as internal standards. This fact, coupled with the increased influence of matrix effects and elemental fractionation on the analysis of small particles found by Pearce et al. (2011) may have been a large factor in the unsuccessful nature of these analyses.

Attempts were made to determine whether microanalysis of larger particles, such as soil particles in the 100 – 500 μm size range, were able to be analyzed using our LA-ICP-MS setup. However, due to the heterogeneity of our sample, it was conjectured that matrix effects likely had a significant impact on the signal output; due to the infeasibility of using an internal standard, there was no way to ensure the quantitative analysis of the elemental composition of the particles. Nevertheless, the relative elemental composition still holds interest as it can shed light into particle mineralogy, and thus a qualitative approach was employed for the analysis of these particles. The results of our analysis of Fe, Mn, and Cr in particles 100 – 500 μm in diameter can be found in Figure 3-S8b. It is much more clear which particles possessed the elements analyzed, as the measured peak intensity was much higher than the calculated limit of detection (which was calculated as three times the standard deviation of the blank, added to the average value of the blank, in the absence of an applicable calibration curve). The results

from this analysis can be used as a binary indicator of whether or not the particle contained the metals analyzed (with a result of either "yes" or "no), in order to count, over a large population of particles, the number that contain a given metal. In addition, the relative concentrations of the various metals can be used to shed light on the mineralogy of the particles. However, as this technique was not able to be applied to our PM_{10} air samples, it was decided that the cost and time intensity of the technique were not worth the limited information able to be obtained, and thus attempts at microanalysis using LA-ICP-MS were not pursued.

	1% laser power		*2% laser power*	
	R^2	LOD (ppm)	R^2	LOD (ppm)
^{53}Cr	0.9994	46.9	0.9996	45.228
^{55}Mn	0.998	84.05	0.9997	72.9484
^{57}Fe	0.333	833.061	0.9967	61.5065
^{61}Ni	0.5803	366.461	0.9995	61.5065
^{75}As	0.9979	-5.143	1	4.4604
^{82}Se	0.99303	1184.97	0.9734	690.646
^{85}Rb	0.9998	252.169	0.9971	208.069
^{88}Sr	0.99452	-6.3286	0.99902	4.0469
^{107}Ag	0.9997	-1.0824	0.9979	11.4475
^{111}Cd	0.9978	-7.6533	1	0.26237
^{121}Sb	0.99936	-7.9025	0.9997	5.28133
^{137}Ba	0.99957	0.1455	0.9998	0.0855
^{208}Pb	0.9992	0.02878	0.9995	0.038
^{232}Th	0.99913	0	0.9996	0
^{238}U	0.99924	0.18055	0.9996	0.216

Table 3-S2. R^2 and limit of detection (LOD) values for the analysis depicted in Figure 3-S9.

While microanalysis using LA-ICP-MS proved unsuccessful, we hoped to use this technique to obtain the bulk elemental composition of our samples. Thus, the final attempt to use LA-ICP-MS to characterize reference soil samples (to assess the feasibility before applying the technique to PM_{10}) was the application of bulk analysis techniques. To perform this analysis, a similar protocol as was used for microanalysis was employed, with the only differences being the use of a lower laser power, wider spot size, and firing patter instead of ablating a single spot. Calibration curves using NIST 612 and 610 were created using a laser beam width of 100 µm and both 1 % and 2 % laser power (Table 3-S2). A visual comparison of the resulting R^2 values for each of the elements monitored can be found in Figure 3-S9.

Similarly, a beam width of 100 µm and a laser power of 1 % was used for the analysis of soil samples. Soils were mounted and analyzed using a firing pattern, as can be seen in Figure 3-

S7d. The ablation time per firing pattern was 5 mins, and ten replicates from different portions of the soil sample were analyzed. The resulting concentrations for each element, from each replicate, were averaged to obtain the overall concentration. Again, due to the heterogeneity of our sample, as well as the presence of Si in the tape, it was not possible to use neither Si nor Ca as an internal standard, and thus only external standard calibration was used to quantify each element.

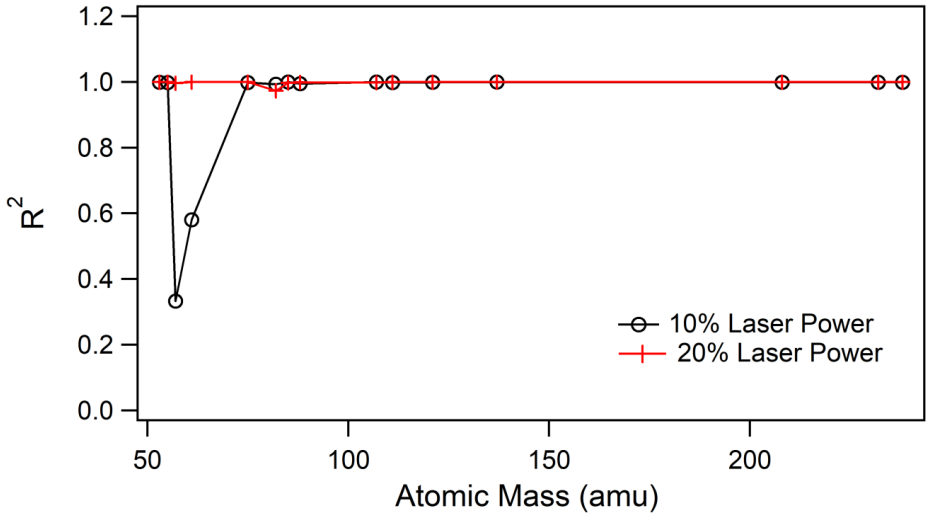

Figure 3-S9. Comparison of the R^2 values of the calibration curves generated using laser ablation ICP-MS with a laser spot size of 100 µm and varied laser power.

The resulting elemental concentration of a soil sample determined using LA-ICP-MS is shown in Table 3-S3, alongside the results of ICP-MS analysis of the soil sample after metals extraction via digestion. Only the concentrations of elements that were both measured by LA-ICP-MS analysis and were quantifiable using solution phase ICP-MS are provided. There is a clear difference between the LA-ICP-MS results and those of the ICP-MS analysis of the digested soil. Furthermore, the discrepancy is not consistent: LA-ICP-MS detected much higher levels of Cr than solution phase ICP-MS (171 mg/kg versus only 29.8 mg/kg), while the opposite was true for Fe (1627.9 mg/kg versus 21782 mg/kg). There were two elements where the measured concentrations were somewhat similar between the two techniques: Mn and Pb. It is also possible that some of the measured element mass fractions were quantifiable for LA-ICP-MS but were not quantifiable via digestion method employed for solution phase

ICP-MS; however, there is no possibility of confirming whether these concentrations were correct. Furthermore, we did not attempt to perform bulk LA-ICP-MS on PM_{10} filter samples, a feat that could potentially be much more successful than the bulk analysis of soil samples due to the smaller particle size and increased homogeneity of PM_{10} size and composition.

Element	LA-ICP-MS Mass Fraction (mg/kg)	Digested Sample ICP-MS Mass Fraction (mg/kg)
^{53}Cr	171.2 ± 8.61 (5.03 %)	29.8 ± 1.25 (4.19 %)
^{55}Mn	358.9 ± 25.99 (7.24 %)	376.8 ± 14.91 (3.96 %)
^{57}Fe	1627.9 ± 122.5 (7.53 %)	21782 ± 581.12 (2.67 %)
^{61}Ni	507.8 ± 11 (2.17 %)	34.07 ± 0.88 (2.57 %)
^{88}Sr	29.8 ± 6.57 (22.04 %)	115.8 ± 6.29 (5.43 %)
^{137}Ba	190.1 ± 21.54 (11.33 %)	93.78 ± 8.24 (8.79 %)
^{208}Pb	7.3 ± 3.44 (47.11 %)	6.17 ± 0.25 (4.05 %)

Table 3-S3. Comparison of ICP-MS results from the analysis of a reference soil sample collected from the exposed sediment of the Ä'äy Chù, with aerosols introduced to the plasma via laser ablation (left) or digestion followed by solution-phase nebulisation (right).

3.3 Single particle ICP-MS analysis of TiO_2 microspheres

The goal of the SP-ICP-MS analysis performed in this study was to evaluate the potential use of SP-ICP-MS for the determination of the mineralogical composition of mineral dust particles with diameters of 1 μm or less, or PM_1. A suspension of 950 nm TiO_2 microspheres supplied by Corpuscular Inc. was analysed using SP-ICP-MS to evaluate the feasibility of using this technique for analysis of ambient dust particles collected from the Ä'äy Chù Valley. SP-ICP-MS is typically employed for the analysis of nanoparticles; thus, a validation test was required to determine whether the technique can be employed for the analysis of particles 1 μm in diameter. Evaluation of whether particles in the PM_1 size range of mineral dust can be measured using this technique was of interest, as expanding the use of SP-ICP-MS beyond the nanoparticle size range holds great advantages in the analysis of mineral dust.

Samples were prepared by performing a 10,000x dilution of the stock solution of TiO_2, which has a concentration of 2.5 g/mL according to the manufacturer. The stock solution was vortexed for 1 min followed by 1 hour of sonicating. An aliquot of 4 µL of the stock solution was then transferred to a clean, 50 mL polypropylene tube, and 40 mL of MilliQ water was added.

The Attom HR-ICP-MS was utilized for SP-ICP-MS analysis. Optimization of the ICP-MS was performed in an identical manner as described in the previous section, the only difference being that a Ni WA7 skimmer and Nu instruments 1.15 mm screw-in cone were used in this analysis, as these are more suitable for the analysis of wet samples. All analyses were performed using attenuated detection mode, meaning that the instrument used a filter to attenuate the ion beam before detection. This was due to the exceptionally high ion concentrations injected into the instrument during analyses, as the analysis of microspheres required calibration standards that are much higher than those typically used for nanoparticle analysis.

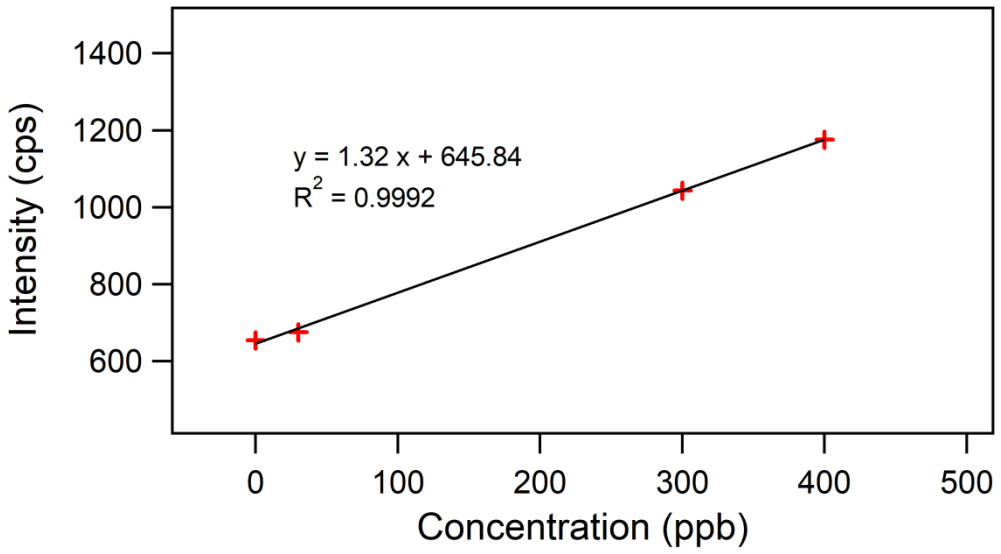

Figure 3-S10. Calibration curve developed for single particle ICP-MS analysis of TiO_2 microspheres. R^2 and interpolation equation are also displayed.

To begin, the transmission efficiency was measured by analyzing a 500 ppt solution of 60 nm gold nanoparticles prepared from the certified reference material NIST 8013. Using NuQuant

data analysis software, the transmission efficiency was found to be 0.18 %. Ionic calibration standards of Ti^{4+} were prepared over a range of 0 – 400 ppb, with the resulting calibration curve possessing an R^2 value of 0.9992 (Figure 3-S10). Finally, a solution of 950 nm TiO_2 particles was analyzed. The concentration of TiO_2 microspheres provided by the manufacturer was 2.5 g/mL, but this was called into question because a large aggregated mass of particles was observed to have formed at the bottom of the stock solution tube, and it was not possible to resuspend these particles in solution. As a result, we have classified the concentration of the solution analyzed as unknown.

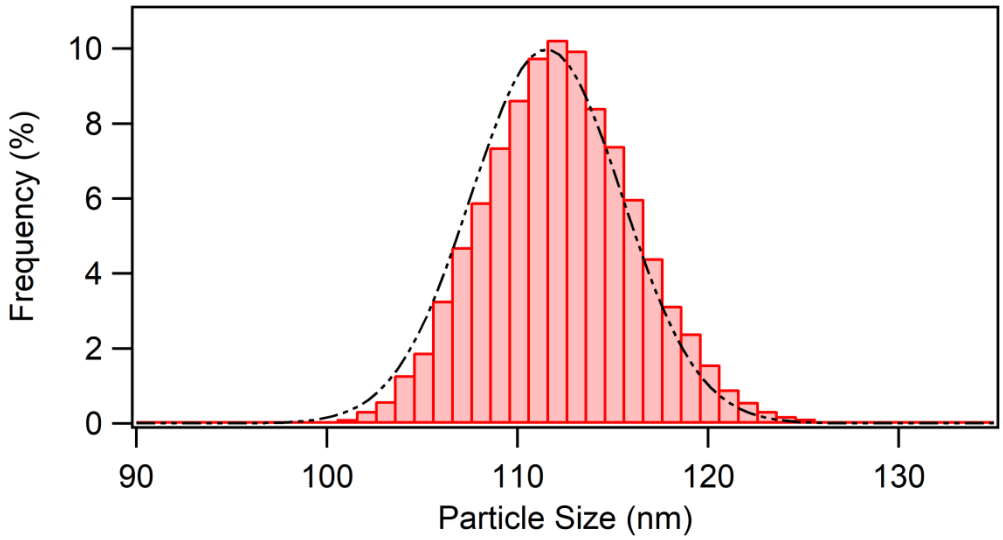

Figure 3-S11. Single particle ICP-MS results from the analysis of 950 nm TiO_2 microspheres. The average size of the analyzed particles, with the standard deviation, was found to be 111.6 nm ± 4.1 nm, indicating this technique undersized the analyzed particles by over an order of magnitude.

The result of the above protocol was that the TiO_2 microspheres were sized as 111.6 nm ± 4.1 nm, where the error provided comprises one standard deviation. A histogram of the sizing results, as well as a gaussian fit of the size distribution, can be found in Figure 3-S11. Assuming the average particle size of 950 nm provided by the manufacturer is correct, this demonstrated that the SP-ICP-MS procedure used underestimated the size of the analyzed TiO_2 microspheres by almost one order of magnitude. Thus, it was concluded that our SP-ICP-MS analysis was unable to accurately characterize PM_1.

There are several reasons why this result was obtained. Firstly, there may have been an incorrect assessment of the transmission efficiency of particles from the solution into the ICP. This value is calculated using 60 nm gold nanoparticles, which usually poses no issue for the analysis of nanoparticles. However, the microspheres used in this study were more than ten-times larger than the gold particles used for the transmission efficiency calculation. As a result, the TiO_2 particles analyzed may have possessed a much lower transmission efficiency than the nanoparticles, as it may be more likely for these particles to settle in the various components of the ICP during transport. The transmission efficiency is used by the Nu Quant software to calculate particle size, and thus any errors in this value will result in erroneous particle sizing results.

Secondly, and by far the most likely explanation for the observed underestimation of the diameter of TiO_2 microspheres analyzed, it is possible that the background levels of titanium particles in solution were mistakenly sized. This would be a result of a signal from Ti that was too high to be detected by SP-ICP-MS. This is due to the fact that the attenuated signal detection by the ICP-MS has a limit to the maximum intensity that can be recorded. This limit corresponds to a particle analysis peak intensity of approximately 1×10^9, which, according to calculations performed by Madjid Hadioui, corresponds to a particle diameter of 350 nm (Hadioui 2018). Thus, if the peak intensity of the 950 nm TiO_2 particles analyzed exceeded this threshold, the instrument may not have been able to process the signal and all peaks resulting from microsphere analysis may have been excluded from the dataset. As a result, the dataset would only include particles that were in the detectable range of the ICP-MS instrument, which could include any smaller nanoparticles of TiO_2 that may have been present in background concentrations in the sample.

Thirdly, it may be possible that the TiO_2 particles were not sized correctly due to incomplete ionization in the ICP. If particles were only partially ionized in the ICP, this would result in a much lower peak intensity per particle, resulting in the underestimation of particle size. Regardless of the reason for the discrepancy in the results, we have concluded that the results of these experiments indicate the infeasibility of characterizing PM_1 using SP-ICP-MS. Because the TiO_2 microspheres analyzed were not accurately sized using this technique, we are unable to confirm whether or not particles of this size are completely ionized in the ICP,

nor whether it is feasible to quantify their minor and trace element content. We did not test whether or not SP-ICP-MS may be used to analyze particles in the 100 nm size range, and thus it may still be possible to apply this technique to the determination of mineral dust nanoparticle mineralogical content. In addition, it may be more feasible to analyze minor and trace elements in PM_1, if the particles are completely ionized in the ICP and the sizing issue was due to the overwhelmingly high signal from the particles. This is because minor and trace elements have much lower concentrations than the major element, and thus provide a lower signal that may be detected by the instrument.

3.4 Vertical aerosol flux calculations

The vertical aerosol mass flux of PM_{10} particles was calculated using the gradient method of Gillette et al. (1972), given by Equations 2-1 and 2-2. This simple flux model was also used to calculate the vertical flux of trace elements analyzed via ICP-MS. The results of the gradient method were compared to the modeled dust emissions given by the vertical flux parameterization provided by Ginoux et al. (2001). The parameterization is given in equation (3-1), where F_p is the vertical flux of a given particle size range, C is a dimensional constant of 1 $\mu g \cdot s^2/m^5$, S is the probability of finding erodible sediment at the location studied (and was thus set to 1), s_p is the fraction associated with each particle size range, u_{10m} is the wind speed at a height of ten meters, and u_t is the threshold velocity as calculated by Equation 2-4. However, note that Equation 3-1 is only valid when u_{10m} is above the threshold velocity, u_t, and that otherwise F_p is set to zero. A more detailed accout of this vertical aerosol flux parameterization can be found in the text of the Ginoux et al. 2001 manuscript.

$$F_p = CSs_p(u_{10m})^2(u_{10m} - u_t) \qquad (3\text{-}1)$$

$$v_{stk} = \frac{2}{9}\frac{\rho_p g}{\mu} r^2 C_{cunn} \qquad (3\text{-}2)$$

The threshold wind velocity, u_t, was calculated using Equation 2-4 and the meteorological equipment in place at the DV site. In addition, the flux due to gravitational settling, v_{stk}, was calculated using Equation 3-2, in which ρ_p is the particle density, g is acceleration due to gravity, μ is the absolute viscosity of the air, r is the particle radius, and C_{cunn} is the

Cunningham correction factor. To calculate the deposition flux of particles due to gravitational settling, the product of the v_{stk} and the calculated F_p was subtracted from F_p, for each size bin.

The purpose of the comparison between the Gillette et al. and the Ginoux et al. parameterizations was to investigate whether the Ginoux et al. parameterization would be able to successfully model trends in dust emission that we observed at our DV tower if all the meteorological data was provided. We tested this parameterization both with and without the modified particle size distribution of the Kok group (Kok 2011; Zhang et al. 2013), as well as with the size distribution output by our OPC measurements. Finally, we tested varying the threshold velocity and particle size distributions used in the model, which we found to have little effect on the model output (Figure 3-S12).

The vertical aerosol flux results of the gradient method of Gillette et al. (calculated using our wind-speed data and gravimetric analysis) and the parameterization developed by Ginoux et al. (which used meteorological data only) are provided in Figure 3-S13. The output of the Gillette method ranges from -9855.6 $\mu g/m^2/s$ to 5491.6 $\mu g/m^2/s$, while that of the Ginoux et al. method ranges from 13.691 $\mu g/m^2/s$ to 2685.2 $\mu g/m^2/s$; generally, the correlation between the outputs of the two dust emissions parameterizations is quite low, with an R^2 value of 0.007. The two parameterizations give results that differ greatly in their identification of major dust emission events: the gradient method indicates a major dust event occurred on May 19 from 11 a.m. to 10 p.m. (PST) while the Ginoux et al. parameterization predicts significantly less dust emission during this period, and the Ginoux et al. parameterization infers major dust emission episodes on May 20 from 6 a.m. to 10 p.m. (PST) and from May 25 at 10 a.m. to May 26 at 3 a.m. (PST) while there are no significant dust emissions indicated by the gradient method during either of these periods. There is also a significant portion of the gradient method result that is negative, while the results of the Ginoux et al. parameterization never fall below zero. Thus, the dust emissions fluxes calculated from our experimental gravimetric data and those calculating using the parameterization of Ginoux et al. do not agree.

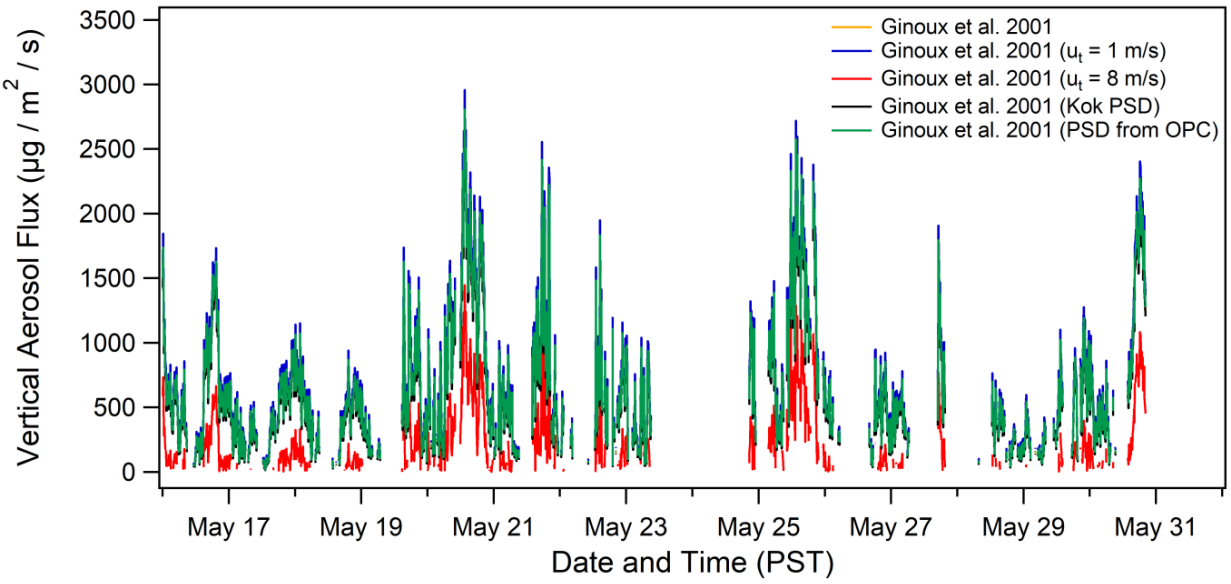

Figure 3-S12. Comparison of the Ginoux et al. 2001 vertical aerosol flux model output with varied threshold velocity (u_t) and particle size distribution (PSD).

The differences between the results of the gradient method and the Ginoux et al. parameterization are most likely due either to the calculations performed or to differences in the mechanism of dust emission considered by the Ginoux et al. parameterization and those that occur from the sediment of the Ä'äy Chù Valley. The errors in the output of the Ginoux et al. parameterization may result from the omission of the term accounting for dry deposition turbulent transfer of particles to the surface. Because this was not included in the calculation, the Ginoux et al. results provided in Figure 3-S13 may be slightly higher than the values that would have been predicted by the parameterization were this component of dry deposition to be included. This may be a reason why the values output by the Ginoux et al. parameterization do not fall below zero for the period of sampling.

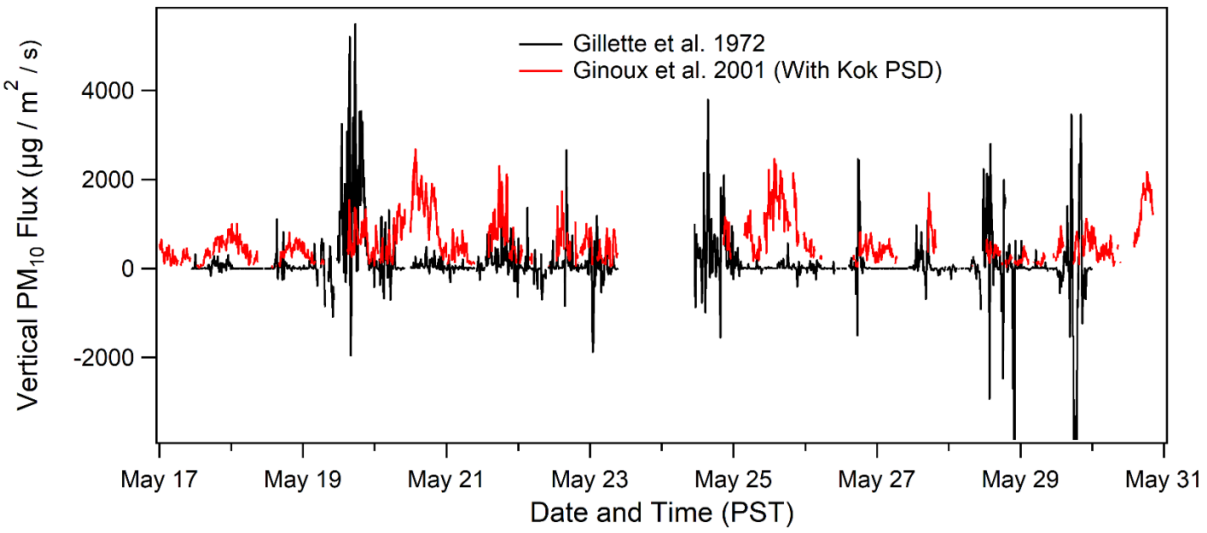

Figure 3-S13. 10-min vertical aerosol flux calculate using both the Ginoux and Gillette parameterizations. Points below -3000 ug/m^2/s are not shown. Weather data from the DV site was used to compute all results.

However, the omission of this deposition mechanism cannot explain the discrepancy between the parameterization outputs during which the gradient method calculations surpass those of the Ginoux et al. parameterization, such as in the case of May 19. Thus, another explanation is needed to more fully explain the discrepancy between the observed and modeled dust emission results. One possibility is that the mechanism of dust emission modeled by the Ginoux et al. parameterization is not applicable to or does not consider factors affecting the mechanism of sediment emission from the Ä'äy Chù Valley. The parameterization of Ginoux et al. assumes dust production occurs only from a saltation and sand-blasting mechanism, and has only been verified for a certain size distribution of soils; due to the high abundance of silt in the sediment of our pro-glacial location, the particle size distribution of the erodible soil from which dust is emitted is likely finer compared to other studies of dust emission sources. Thus, the dust emissions mechanisms dominant at this location may not be the same as at more well characterized low-latitude dust sources.

Finally, it should be noted calculations to determine the ambient vertical aerosol flux were completed using IGOR Pro. The code used to perform these calculations is provided in the Appendix (Section A and B), for both the method of Gillette et al. 1972 and the method of

Ginoux et al. 2001. All calculations were performed on a 10-minute time resolution, and any necessary information regarding air density or wind speed was calculated using the weather data collected at the Down Valley site.

3.5 Data analysis using IGOR Pro

A significant portion of the work in this thesis document involved the analysis of large datasets using IGOR Pro (Appendix A to G). This includes the calculation of the time-resolved normalized size distribution from the OPC data, calculation of the threshold velocity for dust emissions from weather data, and the graphical representation of SEM/EDS spectral data. The analyses that were and were not included in the Bachelder et al. manuscript, such as calculations involving the APS data or the vertical aerosol flux calculation based on the Ginoux et al parameterization, are included in these appendices.

3.6 SEM Images and SEM/EDS Mapping

While the images obtained during SEM/EDS analysis of PM_{10} and soil particles were not directly used in the published manuscript, they nevertheless contain insight into the shape, angularity, and surface characteristics of the mineral dust particles analyzed. Select images of both microscopy images and the SEM/EDS mapping results are provided in Annex H.

Chapter 4 – Conclusions

The chemical and microphysical properties of wind-blown mineral dust emitted from the Ä'äy Chù Valley, Yukon in Northern Canada were successfully determined from samples collected in May 2018. The overall trends in dust emissions, particle size distribution, mineralogy, and chemical composition of ambient PM_{10} were observed during this period, and important insights were gained concerning the dust emissions mechanisms at this site. This characterization study also included a mineral dust sampling campaign which took place June 2017, during which initial observations of dust emissions at this site confirmed that the Ä'äy Chù Valley is an active dust source. In the preceding pages, we have outlined both the final analyses in Chapter 2, as well as the unsuccessful exploratory work (Chapter 3). Overall, we have provided important results that will aid in establishing an understanding of the dust emission mechanisms and local impact of the dust emitted at this site, while validating low-cost, efficient methods of characterizing mineral dust emissions from a remote, high-latitude dust source.

4.1 Characterization of microphysical properties

The results of particle sizing and gravimetric analysis performed during both June 2017 and May 2018 have been provided. The initial results of APS measurements obtained June 10 to 23, 2017 at the Thachäl Dhäl Visitor's Center confirmed that the Ä'äy Chù Valley is a source of mineral dust whose composition and shape are unique relative to the background aerosol species present at this location; however, due to increased precipitation that suppressed the emission of dust during the sampling period, limited data was obtained during this field campaign. A more comprehensive dataset was obtained May 4 to 31, 2018, providing crucial information as to the intensity and pervasiveness of dust emissions from this location. The highest concentrations of ambient PM_{10} were typically observed between 13:00 and midnight (PST), according to analysis of diurnal trends, while gravimetric analysis of 24-hour filter samples showed significant daily PM_{10} throughout the sampling period, both directly in the dust source as well as at three surrounding sites. Furthermore, the normalized particle size distribution showed little day-to-day variation, indicating consistency in the size distribution of PM_{10} particles in the Ä'äy Chù Valley.

In addition, the 24-hour measured PM_{10} and estimated $PM_{2.5}$ concentrations for May 2018 at sites surrounding the dust source surpassed the 24-hour PM_{10} and $PM_{2.5}$ air quality thresholds supplied by the World Health Organization (WHO) at least once at each site during the sampling period. This includes measurements performed at the Thachäl Dhäl Visitor's Center and a location near the Alaska Highway. As the WHO 24-hour PM_{10} and $PM_{2.5}$ thresholds are an indicator of the level of ambient particulate matter that may have negative effects on human health in the short-term – such as aggravation of asthma, impaired lung function, and risk for those with heart problems – the fact that these levels were surpassed at multiple sites near the dust source indicates that dust emitted from the Ä'äy Chù Valley negatively impacts local air quality. However, further sampling over a longer period is necessary to fully evaluate the impact of mineral dust emissions from the Ä'äy Chù Valley on local air quality and public health. In future dust sampling campaigns, measurement stations will also be established in local communities – for example, Destruction Bay would be an excellent location to monitor PM_{10} and $PM_{2.5}$ as it is the closest town to the dust source, located 40 km northwest of the site.

4.2 Mineralogical composition and particle morphology

The mineralogical composition and particle morphology of a PM_{10} sample was determined using SEM/EDS analysis. It was found that the mineralogy comprised primarily aluminosilicate clay mineral aggregates, with pure minerals such as quartz, calcite, gypsum, and dolomite making up only 24% of the overall mineralogical composition. Fe was detected in 23 % of particles, all of which were clay minerals; no Fe-oxide minerals were detected by our SEM/EDS analysis. In addition, analysis of the aspect ratio – a parameter characterizing particle shape that has been defined in this study as the ratio of the length of the longest axis to that of the longest perpendicular axis – indicated that 88 % of particles analyzed possessed elongated shapes with aspect ratios exceeding the first size bin of 1 to 1.14 µm, with certain particles possessing aspect ratios exceeding 3. The SEM/EDS analysis performed in this study, while only semi-quantitative due to the limited number of samples and particles analyzed, demonstrates that ambient PM_{10} collected from the Ä'äy Chù Valley is composed primarily of aluminosilicate aggregate minerals and non-spherical particles. These results are highly valuable for future attempts to model the impact of dust emissions from the Ä'äy Chù Valley

on regional climate, as the mineralogy and shape of particles are highly related to their optical properties.

4.3 Analysis of elemental composition

Two techniques were employed to determine the elemental composition of soil samples collected from the Ä'äy Chù: ICP-MS and LA-ICP-MS. Microanalysis of individual PM_{10} particles using LA-ICP-MS was not possible, as particles in this size range were too small to be detected by our LA-ICP-MS setup. This is because the microscope system of the laser ablation unit does not possess high enough resolution to allow for the precise ablation of particles as small as 10 μm in diameter, as well as the fact that the minimum diameter of the laser beam width is 5 μm. It is for these reasons that no signal was able to be obtained from the analysis of PM_{10} particles using LA-ICP-MS. As soil particles are much larger than PM_{10}, often including particles 100 μm in diameter or larger, a signal was successfully obtained from these particles using LA-ICP-MS. However, due to matrix effects and elemental fractionation, we were unable to quantify the elemental content of individual soil particles. Finally, our attempts to determine bulk composition of soils using LA-ICP-MS were also unsuccessful, while the feasibility of using this technique to analyze ambient PM_{10} collected on filters was not assessed.

ICP-MS analysis of the bulk elemental composition proved more effective than LA-ICP-MS analysis, allowing us to quantify the minor and trace element content in the ambient PM_{10}, deposited dust, and soil samples we collected. Method 3051a, which outlines the U.S. EPA certified procedure for the extraction of metals from samples using acid digestion followed by ICP-MS analysis, was modified to allow lower detection limits and, subsequently, the analysis of smaller sample masses compared to those typically used. Thus, acid extractions of filter samples were performed using 4 mL ultrapure HNO_3 and 1 mL ultrapure HCl, while the digestion of soil samples was performed using 3 mL ultrapure HNO_3 and 1 mL HCl due to the absence of a filter which decreased sample mass. Validation of both the filter and soil digestion methods was performed to determine whether metals were quantitatively extracted and analyzed by applying the modified protocol to the analysis of standard reference soils of

known elemental composition. It was found that nine elements (Mn, Fe, Co, Ni, Cu, As, Cd, Cs, and Pb) were quantitatively extracted using these methods.

Samples of ambient PM_{10}, deposited dust, and soils collected from the Ä'äy Chù Valley were analyzed using this validated ICP-MS protocol. The analysis of both the bulk composition as well as the isolated fine fraction (<53 μm in diameter) of soils was completed, as this is the size fraction that is most likely to be entrained as mineral dust. The composition of ambient PM_{10} samples did not show significant temporal and spatial variation, nor did deposition samples collected both within the dust source and at surrounding locations (with the exception of the Christmas Bay location). Fine soil samples showed higher variability in As and Pb than in the other metals analyzed, while bulk soils lacked the high variability in Pb content but otherwise showed similar trends in spatial variability as the fine soils. Furthermore, we observed significant enrichment in the minor and trace element content of PM_{10} as compared to bulk samples, with enrichment factors between 1.5 and 3.5 depending on the element. This enrichment was not consistent across all elements, with Cu and As showing much higher enrichment compared to the other metals analyzed. We also observed a similar enrichment in the elemental composition of deposited dust as compared to that of bulk samples. Moreover, the elemental composition of the deposition samples was found to be relatively similar to that of the fine fraction of the soils.

Initial tests were performed to evaluate the feasibility of using SP-ICP-MS to analyze PM_1, or particles smaller than 1 μm in diameter. The analysis of 950 nm TiO_2 engineered particles using SP-ICP-MS set to attenuated detection mode undersized the analyzed microspheres by almost an order of magnitude. While the specific reason for the underestimation of the particle size is not known, the analysis was not able to confirm that 1 μm particles can be completely ionized in the ICP, nor that their elemental compositions analyzed correctly. However, this does not necessarily eliminate the possibility of using SP-ICP-MS for the analysis of smaller mineral dust particles, such as those in the 400 nm or less size range, though the issue of unknown chemical composition and polydispersity of the particles must be considered. The idea of using SP-ICP-TOF-MS to detect the relative elemental concentrations, similar to how SEM/EDS was used in this study, is a possible question for future research on this topic.

4.4 Dust emission mechanisms

Finally, analyses were completed to gain insight into the intensity and mechanism of dust emissions from the Ä'äy Chù Valley during the May 2018 sampling campaign. The vertical aerosol flux was calculated using measurements from the Down Valley site (Gillette et al. 1972), with the results demonstrating that emissions were occurring at the Down Valley site throughout the May 2018 sampling period. The calculation of vertical aerosol flux from a common dust emission parameterization (Ginoux et al. 2001) yielded very different results from that of Gillette et al; this may be explained by the fact that the Ginoux et al. 2001 parameterization was developed specifically from field studies completed in commonly studied low-latitude dust sources, such as in the Sahara desert, whose soils vary greatly in size and composition as compared to the soils of the Ä'äy Chù Valley. Given the discrepancy in the results of these two methods for calculating vertical aerosol flux, it is likely the mechanism for dust emissions at the Ä'äy Chù Valley differs greatly from those at lower latitudes. Therefore, it was concluded that the parameterization of dust emissions by Ginoux et al. is not appropriate for the calculation of dust emissions from the Ä'äy Chù Valley. This is a compelling result, as the discrepancy between the output vertical aerosol flux of the Ginoux et al. model – which is commonly used in global climate models, such as GEOS-Chem (Johnson et al. 2012) – and the results of the experimentally determined vertical aerosol flux is likely indicative of the inadequacy of these global climate models in depicting emissions from high-latitude dust sources.

The vertical aerosol flux calculations provided insight into the emissions processes occurring at the Ä'äy Chù Valley. To delve deeper into the potential mechanism of dust emission at the Ä'äy Chù, an analysis of the spatial variability of deposited dust composition was performed. Overall, the dust deposition samples showed little variation in composition, with the exception being the sample collected from Christmas Bay. By extension, the enrichment factor of each element analyzed as compared to the bulk soil samples was relatively consistent between deposition samples. This was a key result, as it demonstrated that the elemental enrichment of the deposition samples is present at the dust source, in the areas surrounding the dust source, and across Kluane Lake, indicating that the mechanism that leads to the observed elemental enrichment occurs during dust entrainment as opposed to during transport.

An important dust emissions mechanism that was evaluated in this study was the saltation-sandblasting mechanism that is often thought to be an important contributor to the emission of dust. We found no correlation between our saltation measurements and the dust emitted from the Down Valley site, a highly irregular result that has either stemmed from instrument malfunction or a limit of detection of our saltation measurements that was too high to detect saltating particles. However, we have identified the extensive evidence that saltation-sandblasting was an important mechanism for dust emission, including calculated shear velocities and measured windspeeds that greatly surpass the values at which saltation-sandblasting was observed in previous studies, as well as our investigation of calculated horizontal mass flux using the parameterization developed by Nickling et al. 1978. Furthermore, through analysis of the small particle sizes measured in both ambient PM_{10} and soil samples, as well as the variation in elemental composition between sample types, we have identified the rupturing of clay coatings present on larger silt- and sand-sized particles as a likely mechanism for dust emissions from the Ä'äy Chù Valley. Our conclusion is further supported by the observations of the SEM/EDS analysis, which showed a dominance of clay minerals in the mineralogical composition of ambient PM_{10} as well as the presence of clay coatings on soil particles. We were also unable to rule out the possible contribution of the release of resident fine particulate matter from sand particles upon impact with the surface.

4.5 Future work

As this study was the first of attempt of a longer, five-year research campaign dedicated to the study of dust emitted from the Ä'äy Chù Valley, a major function of the results presented here is to highlight the importance of future work studying the physico-chemical characteristics of dust emissions from this site. This is due to the fact that the results presented in this thesis cover a wide range of topics, including potential air quality concerns, the nutritive content of the dust and its potential impact on local biogeochemical cycling of minerals, the detailed mechanisms of dust production, and more. Thus, as much as these results provide new information on dust emitted from this source, they serve equally as an indicator for how much more there is to learn about the emisson of dust and its impact in Yukon's Kluane Lake region.

An important next step in the process of researching the dust emissions from the Ä'äy Chù Valley is to extend the campaign period to include study of the microphysical and chemical properties of the emitted dust throughout the year. The measurement campaigns depicted in this work were confined only to the late spring and early summer. This is, admittedly, a crucial period for dust emissions, as explained previously – however, it is also noteworthy that intense dust emissions were also observed at other points in the year, particularly towards late summer and early fall. Moreover, dust emissions were observed to occur regularly throughout the entire period of May to October 2017 by the camera monitoring station at the Island site. Vertical flux of the dust from the site may vary seasonally, and the collection of more data points throughout the year could aid in efforts to better understand, and eventually parameterize, this flux as it relates to meteorological factors, such as wind speed. Longer-term measurements would additonally aid the evaluation of the negative effects of the emitted dust on local air quality.

Indeed, the impact of the emitted dust on public health must be more thoroughly evaluated, as no measurements of PM_{10} or $PM_{2.5}$ were taken in the communities that live closest to the dust source such as Destruction Bay or Burwash Landing. This is crucial to study, as it is necessary to evaluate the impact of the dust emissions from the Ä'äy Chù Valley on the air quality in communities closest to the source in order to evaluate whether or not the emissions are a menace to public health. Thus, while the results of this study did indicate that the dust emitted from the Ä'äy Chù Valley does negatively impact the air quality in the area immediately surrounding the dust source, more information is needed on the degree to which air quality in local communities is impacted by emissions. Additionally, the effect of the dustiness on indoor air quality must also be considered when evaluating the impact of the dust on public health (Ghoshdastidar et al. 2018).

Another important aspect of this project is the effect the emitted dust may have on local biogeochemical cycling of metals, which may impact primary productivity in both marine and terrestrial environments, and may also impact the health of local wildlife. While this study does report the total elemental content of certain metals, such as iron and arsenic, the speciation of these elements must be determined to better evaluate their bioavailability and potential impact on local ecosystems. This is because the bioavailability of metals may change

significantly based on their speciation in the environment – for example, inorganic species arsenate and arsenite are more toxic than organic arsenic compounds due to the difference in their bioavailability (Pongratz 1998). Thus, a study of the speciation of the metals present in the dust emitted from the Ä'äy Chù Valley, with particular focus on iron and arsenic, is an important next step in the processes of evaluating the potential impact of the dust on local ecosystems and wildlife.

To conclude, we have successfully completed a case study of the composition, microphysical properties, and mechanisms of emission of mineral dust from the Ä'äy Chù Valley in the Kluane Lake region of Yukon, Canada. This campaign was the first, to our knowledge, in which direct measurements of dust emitted from a high-latitude dust source in a pro-glacial valley were performed. Furthermore, mineral dust emissions at this location are highly impacted by the active retreat of the Kaskawulsh Glacier – whose meltwaters no longer flow into the Ä'äy Chù Valley, leaving the sediment dried and more prone to erosion – and are thus indirectly affected by the rapidly rising temperatures in the Canadian North. Our research has shown the negative effects of the mineral dust emitted from this location on air quality, and indicate the enrichment of minor and trace elements in PM_{10} as compared to bulk soils. This work also provides important insights into the mechanism of dust production that leads to this enrichment, while providing an example of a robust approach for studying the chemistry and microphysical properties of dust in the harsh environment and remote location of an active dust source. These results have demonstrated the value of measuring dust emissions from the Ä'äy Chù Valley in the Kluane Lake region of Yukon, Canada, and highlight the importance of continued study to elucidate the physical mechanisms of dust emissions at this site and the resulting impact on atmospheric composition, chemistry, and ecosystems.

Bibliography

Allen, M. D. and Raabe, O. G. (1985). Slip Correction Measurements of Spherical Solid Aerosol Particles in an Improved Millikan Apparatus. Aerosol Science and Technology 4:269-286.

Alloway, B. and Steinnes, E. (1999). Anthropogenic additions of cadmium to soils, in Cadmium in soils and plants, Springer, 97-123.

Archuleta, C. M., DeMott, P., Kreidenweis, S. (2005). Ice nucleation by surrogates for atmospheric mineral dust and mineral dust/sulfate particles at cirrus temperatures. Atmos Chem Phys 5:2617-2634.

Arnalds, O. (2004). Volcanic soils of Iceland. CATENA 56:3-20.

Atkins, P. and De Paula, J. (2009). Elements of Physical Chemistry. Macmillan.

Atkinson, J. D., Murray, B. J., Woodhouse, M. T., Whale, T. F., Baustian, K. J., Carslaw, K. S., Dobbie, S., O'sullivan, D., Malkin, T. L. (2013). The importance of feldspar for ice nucleation by mineral dust in mixed-phase clouds. Nature 498:355.

Avila, A., Alarcon, M., Queralt, I. (1998). The chemical composition of dust transported in red rains—its contribution to the biogeochemical cycle of a holm oak forest in Catalonia (Spain). Atmospheric Environment 32:179-191.

Baas, A. C. (2004). Evaluation of saltation flux impact responders (Safires) for measuring instantaneous aeolian sand transport intensity. Geomorphology 59:99-118.

Bagnold, R. A. (1941). The physics of blown sand and desert dunes. Springer Netherlands.

Baker, A. R., Jickells, T. D., Witt, M., Linge, K. L. (2006). Trends in the solubility of iron, aluminium, manganese and phosphorus in aerosol collected over the Atlantic Ocean. Marine Chemistry 98:43-58.

Barrie, L. A. (1986). Arctic air pollution: An overview of current knowledge. Atmospheric Environment 20:643-663.

Becker, J. and Tenzler, D. (2001). Studies of LA-ICP-MS on quartz glasses at different wavelengths of a Nd: YAG laser. Fresenius' journal of analytical chemistry 370:637-640.

Bergametti, G. (2004). Dust emission processes.

Betzer, P. R., Carder, K. L., Duce, R. A., Merrill, J. T., Tindale, N. W., Uematsu, M., Costello, D. K., Young, R. W., Feely, R. A., Breland, J. A., Bernstein, R. E., Greco, A. M. (1988). Long–range transport of giant mineral aerosol particles. Nature 336:568.

Brown, P. H., Welch, R. M., Cary, E. E. (1987). Nickel: A Micronutrient Essential for Higher Plants. Plant Physiology 85:801-803.

Bullard, J. E. (2017). The distribution and biogeochemical importance of high-latitude dust in the Arctic and Southern Ocean-Antarctic regions. Journal of Geophysical Research: Atmospheres 122:3098-3103.

Bullard, J. E., Baddock, M., Bradwell, T., Crusius, J., Darlington, E., Gaiero, D., Gassó, S., Gisladottir, G., Hodgkins, R., McCulloch, R., McKenna-Neuman, C., Mockford, T., Stewart, H., Thorsteinsson, T. (2016). High-latitude dust in the Earth system. Reviews of Geophysics 54:447-485.

Bullard, J. E., McTainsh, G. H., Pudmenzky, C. (2004). Aeolian abrasion and modes of fine particle production from natural red dune sands: an experimental study. Sedimentology 51:1103-1125.

Buma, A. G., De Baar, H. J., Nolting, R. F., Van Bennekom, A. J. (1991). Metal enrichment experiments in the Weddell-Scotia Seas: Effects of iron and manganese on various plankton communities. Limnology and Oceanography 36:1865-1878.

Chtaib, M. and Schmit, J.-P. (1988). Negative-ion mode in inductively coupled plasma mass spectrometry. Journal of Analytical Atomic Spectrometry 3:315-318.

Crusius, J., Schroth, A. W., Gasso, S., Moy, C. M., Levy, R. C., Gatica, M. (2011). Glacial flour dust storms in the Gulf of Alaska: Hydrologic and meteorological controls and their importance as a source of bioavailable iron. Geophysical Research Letters 38.

Cutter, G. A., Cutter, L. S., Featherstone, A. M., Lohrenz, S. E. (2001). Antimony and arsenic biogeochemistry in the western Atlantic Ocean. Deep Sea Research Part II: Topical Studies in Oceanography 48:2895-2915.

DeCarlo, P. F., Slowik, J. G., Worsnop, D. R., Davidovits, P., Jimenez, J. L. (2004). Particle Morphology and Density Characterization by Combined Mobility and Aerodynamic Diameter Measurements. Part 1: Theory. Aerosol Science and Technology 38:1185-1205.

Dubovik, O., Holben, B., Eck, T. F., Smirnov, A., Kaufman, Y. J., King, M. D., Tanré, D., Slutsker, I. (2002). Variability of absorption and optical properties of key aerosol types observed in worldwide locations. Journal of the atmospheric sciences 59:590-608.

Dusek, U., Frank, G., Hildebrandt, L., Curtius, J., Schneider, J., Walter, S., Chand, D., Drewnick, F., Hings, S., Jung, D. (2006). Size matters more than chemistry for cloud-nucleating ability of aerosol particles. Science 312:1375-1378.

E. O'Brien, S., W. Acon, B., F. Boulyga, S., S. Becker, J., J Dietze, H., Montaser, A. (2003). Reduction of molecular ion interferences with hexapole collision cell in direct injection nebulization-inductively coupled plasma mass spectrometry. Journal of Analytical Atomic Spectrometry 18.

Ed Hudson, D. A., Tim Gaines, Gilles Simard, John Mullock (2001). The Weather of Nunavut and the Arctic. Graphic Area Forecast 36 and 37.

Engelbrecht, J. P., McDonald, E. V., Gillies, J. A., Jayanty, R. K. M., Casuccio, G., Gertler, A. W. (2009). Characterizing Mineral Dusts and Other Aerosols from the Middle East—Part 1: Ambient Sampling. Inhalation Toxicology 21:297-326.

EPA (2007). Method 3051A (SW-846): Microwave Assisted Acid Digestion of Sediments, Sludges, and Oils, U.S. EPA, Washington D.C.

Falciani, R., Novaro, E., Marchesini, M., Gucciardi, M. (2000). Multi-element analysis of soil and sediment by ICP-MS after a microwave assisted digestion method. Journal of Analytical Atomic Spectrometry 15:561-565.

Falkovich, A. H., Ganor, E., Levin, Z., Formenti, P., Rudich, Y. (2001). Chemical and mineralogical analysis of individual mineral dust particles. Journal of Geophysical Research: Atmospheres 106:18029-18036.

Fan, S. M., Moxim, W. J., Levy, H. (2006). Aeolian input of bioavailable iron to the ocean. Geophysical Research Letters 33.

Formenti, P., Elbert, W., Maenhaut, W., Haywood, J., Andreae, M. (2003). Chemical composition of mineral dust aerosol during the Saharan Dust Experiment (SHADE) airborne campaign in the Cape Verde region, September 2000. Journal of Geophysical Research: Atmospheres 108.

Formenti, P., Schütz, L., Balkanski, Y., Desboeufs, K., Ebert, M., Kandler, K., Petzold, A., Scheuvens, D., Weinbruch, S., Zhang, D. (2011). Recent progress in understanding physical and chemical properties of African and Asian mineral dust. Atmos Chem Phys 11:8231-8256.

Fréchette-Viens, L., Hadioui, M., Wilkinson, K. J. (2017). Practical limitations of single particle ICP-MS in the determination of nanoparticle size distributions and dissolution: case of rare earth oxides. Talanta 163:121-126.

Friehmelt, R., Büttner, H., Ebert, F. (2000). On-line Characterisation of Aerosols – Comparability and Combination of Selected Measuring Devices. KONA Powder and Particle Journal 18:183-193.

Gaudino, S., Galas, C., Belli, M., Barbizzi, S., de Zorzi, P., Jaćimović, R., Jeran, Z., Pati, A., Sansone, U. (2007). The role of different soil sample digestion methods on trace elements analysis: a comparison of ICP-MS and INAA measurement results. J Accreditation Quality Assurance 12:84-93.

Ghoshdastidar, A. J., Hu, Z., Nazarenko, Y., Ariya, P. A. (2018). Exposure to nanoscale and microscale particulate air pollution prior to mining development near a northern indigenous community in Québec, Canada. Environmental Science and Pollution Research 25:8976-8988.

Gillette, D. A., Blifford Jr, I. H., Fenster, C. R. (1972). Measurements of aerosol size distributions and vertical fluxes of aerosols on land subject to wind erosion. Journal of Applied Meteorology 11:977-987.

Gillies, J. and Berkofsky, L. (2004). Eolian suspension above the saltation layer, the concentration profile. Journal of Sedimentary Research 74:176-183.

Ginoux, P., Chin, M., Tegen, I., Prospero, J. M., Holben, B., Dubovik, O., Lin, S.-J. (2001). Sources and distributions of dust aerosols simulated with the GOCART model. Journal of Geophysical Research: Atmospheres 106:20255-20273.

Girão, A., Caputo, G., Ferro, M. C. (2017). Application of Scanning Electron Microscopy-Energy Dispersive X-ray Spectroscopy (SEM-EDS), in Comprehensive Analytical Chemistry.

Grini, A. and Zender, C. S. (2004). Roles of saltation, sandblasting, and wind speed variability on mineral dust aerosol size distribution during the Puerto Rican Dust Experiment (PRIDE). Journal of Geophysical Research: Atmospheres (1984–2012) 109.

Groot Zwaaftink, C. D., Grythe, H., Skov, H., Stohl, A. (2016). Substantial contribution of northern high-latitude sources to mineral dust in the Arctic. Journal of Geophysical Research: Atmospheres 121:13,678-613,697.

Günther, D. and Heinrich, C. A. (1999). Comparison of the ablation behaviour of 266 nm Nd: YAG and 193 nm ArF excimer lasers for LA-ICP-MS analysis. Journal of Analytical Atomic Spectrometry 14:1369-1374.

GÜVEN, D. and Akinci, G. (2011). Comparison of acid digestion techniques to determine heavy metals in sediment and soil samples. Gazi University Journal of Science 24:29-34.

Hadioui, M. (2018). J. Bachelder, ed., Montreal, QC.

Harris, A. R. and Davidson, C. I. (2009). A Monte Carlo Model for Soil Particle Resuspension Including Saltation and Turbulent Fluctuations. Aerosol Science and Technology 43:161-173.

Haywood, J. and Boucher, O. (2000). Estimates of the direct and indirect radiative forcing due to tropospheric aerosols: A review. Reviews of geophysics 38:513-543.

Heithmar, E. M., Hinners, T. A., Rowan, J. T., Riviello, J. M. (1990). Minimization of interferences in inductively coupled plasma mass spectrometry using on-line preconcentration. Analytical Chemistry 62:857-864.

Hinds, W. C. (2012). Aerosol technology: properties, behavior, and measurement of airborne particles. John Wiley & Sons.

Hu, M., Peng, J., Sun, K., Yue, D., Guo, S., Wiedensohler, A., Wu, Z. (2012). Estimation of size-resolved ambient particle density based on the measurement of aerosol number, mass, and chemical size distributions in the winter in Beijing. Environmental science & technology 46:9941-9947.

Huang, J., Minnis, P., Lin, B., Wang, T., Yi, Y., Hu, Y., Sun-Mack, S., Ayers, K. (2006). Possible influences of Asian dust aerosols on cloud properties and radiative forcing observed from MODIS and CERES. Geophysical Research Letters 33.

Huang, Y., Kok, J. F., Martin, R. L., Swet, N., Katra, I., Gill, T. E., Reynolds, R. L., Freire, L. S. (2019). Fine dust emissions from active sands at coastal Oceano Dunes, California. Atmos Chem Phys 19:2947-2964.

Hutton, M. (1983). Sources of cadmium in the environment. Ecotoxicology and Environmental Safety 7:9-24.

Johnson, M. S., Meskhidze, N., Praju Kiliyanpilakkil, V. (2012). A global comparison of GEOS-Chem-predicted and remotely-sensed mineral dust aerosol optical depth and extinction profiles. Journal of Advances in Modeling Earth Systems 4.

Journet, E., Desboeufs, K. V., Caquineau, S., Colin, J. L. (2008). Mineralogy as a critical factor of dust iron solubility. Geophysical Research Letters 35.

Kalashnikova, O. and Sokolik, I. (2004). Modeling the radiative properties of nonspherical soil-derived mineral aerosols. Journal of Quantitative Spectroscopy and Radiative Transfer 87:137-166.

Kappos, A. D., Bruckmann, P., Eikmann, T., Englert, N., Heinrich, U., Höppe, P., Koch, E., Krause, G. H. M., Kreyling, W. G., Rauchfuss, K., Rombout, P., Schulz-Klemp, V., Thiel, W. R., Wichmann, H. E. (2004). Health effects of particles in ambient air. International Journal of Hygiene and Environmental Health 207:399-407.

Kelly, F. J. and Fussell, J. C. (2015). Air pollution and public health: emerging hazards and improved understanding of risk. Environmental Geochemistry and Health 37:631-649.

Kok, J. F. (2011). A scaling theory for the size distribution of emitted dust aerosols suggests climate models underestimate the size of the global dust cycle. Proceedings of the National Academy of Sciences 108:1016-1021.

Krueger, B. J., Grassian, V. H., Cowin, J. P., Laskin, A. (2004). Heterogeneous chemistry of individual mineral dust particles from different dust source regions: the importance of particle mineralogy. Atmospheric Environment 38:6253-6261.
Kuhn, H.-R. and Günther, D. (2003). Elemental fractionation studies in laser ablation inductively coupled plasma mass spectrometry on laser-induced brass aerosols. Analytical chemistry 75:747-753.
Lane, T. W. and Morel, F. M. (2000). Regulation of carbonic anhydrase expression by zinc, cobalt, and carbon dioxide in the marine diatom Thalassiosira weissflogii. Plant Physiology 123:345-352.
Lee, Y. H., Chen, K., Adams, P. J. (2009). Development of a global model of mineral dust aerosol microphysics. Atmos Chem Phys 9:2441-2458.
Lepow, M. L., Bruckman, L., Gillette, M., Markowitz, S., Robino, R., Kapish, J. (1975). Investigations into sources of lead in the environment of urban children. Environmental Research 10:415-426.
Lide, D. R. (1964). Handbook of Chemistry and Physics:B241-B246.
Limbeck, A., Galler, P., Bonta, M., Bauer, G., Nischkauer, W., Vanhaecke, F. (2015). Recent advances in quantitative LA-ICP-MS analysis: challenges and solutions in the life sciences and environmental chemistry. Analytical bioanalytical chemistry 407:6593-6617.
Lis, H., Shaked, Y., Kranzler, C., Keren, N., Morel, F. M. M. (2014). Iron bioavailability to phytoplankton: an empirical approach. The ISME journal 9:1003-1013.
Liu, Y., Hu, Z., Li, M., Gao, S. (2013). Applications of LA-ICP-MS in the elemental analyses of geological samples. Chinese Science Bulletin 58:3863-3878.
Lohmann, U. and Diehl, K. (2006). Sensitivity Studies of the Importance of Dust Ice Nuclei for the Indirect Aerosol Effect on Stratiform Mixed-Phase Clouds. Journal of the Atmospheric Sciences 63:968-982.
Loosmore, G. A. and Hunt, J. R. (2000). Dust resuspension without saltation. Journal of Geophysical Research: Atmospheres 105:20663-20671.
Mahowald, N., Albani, S., Kok, J. F., Engelstaeder, S., Scanza, R., Ward, D. S., Flanner, M. G. (2014). The size distribution of desert dust aerosols and its impact on the Earth system. Aeolian Research 15:53-71.
Mason, B. J. and Maybank, J. (1958). Ice-nucleating properties of some natural mineral dusts. Quarterly Journal of the Royal Meteorological Society 84:235-241.
May, T. W. and Wiedmeyer, R. H. (1998). A table of polyatomic interferences in ICP-MS. ATOMIC SPECTROSCOPY-NORWALK CONNECTICUT- 19:150-155.
McInnes, L., Quinn, P., Covert, D., Anderson, T. (1996). Gravimetric analysis, ionic composition, and associated water mass of the marine aerosol. Atmospheric Environment 30:869-884.
Miller, S. D., Wang, F., Burgess, A. B., McKenzie Skiles, S., Rogers, M., Painter, T. H. (2016). Satellite-based estimation of temporally resolved dust radiative forcing in snow cover. Journal of Hydrometeorology 17:1999-2011.
Mishchenko, M. I., Hovenier, J. W., Travis, L. D. (1999). Light scattering by nonspherical particles: theory, measurements, and applications. Elsevier.

Mitchell, J. (2014). Time-of-Flight Methods for the Measurement of the Aerodynamic Particle Size Distribution of Aerosols from Orally Inhaled Products: Points to Consider. Journal of Aerosol Medicine and Pulmonary Drug Delivery 28.

Mitrano, D. M., Barber, A., Bednar, A., Westerhoff, P., Higgins, C. P., Ranville, J. F. (2012). Silver nanoparticle characterization using single particle ICP-MS (SP-ICP-MS) and asymmetrical flow field flow fractionation ICP-MS (AF4-ICP-MS). Journal of Analytical Atomic Spectrometry 27:1131-1142.

Montaser, A. (1998). Inductively coupled plasma mass spectrometry. John Wiley & Sons.

Moore, C. M., Mills, M. M., Arrigo, K. R., Berman-Frank, I., Bopp, L., Boyd, P. W., Galbraith, E. D., Geider, R. J., Guieu, C., Jaccard, S. L., Jickells, T. D., La Roche, J., Lenton, T. M., Mahowald, N. M., Marañón, E., Marinov, I., Moore, J. K., Nakatsuka, T., Oschlies, A., Saito, M. A., Thingstad, T. F., Tsuda, A., Ulloa, O. (2013). Processes and patterns of oceanic nutrient limitation. Nature Geoscience 6:701.

Morel, F. M., Rueter, J. G., Price, N. M. (1991). Iron nutrition of phytoplankton and its possible importance in the ecology of ocean regions with high nutrient and low biomass. J Oceanography 4:56-61.

Mukherjee, S. (2013). The science of clays. Applications in Industry, Engineering and Environment.

Nardi, E. P., Evangelista, F. S., Tormen, L., Saint, T. D., Curtius, A. J., de Souza, S. S., Barbosa Jr, F. (2009). The use of inductively coupled plasma mass spectrometry (ICP-MS) for the determination of toxic and essential elements in different types of food samples. Food Chemistry 112:727-732.

Nickling, W. (1978). Eolian sediment transport during dust storms: Slims River valley, Yukon Territory. Canadian Journal of Earth Science 15:1069-1084.

Otto, S., Reus, M. d., Trautmann, T., Thomas, A., Wendisch, M., Borrmann, S. (2007). Atmospheric radiative effects of an in situ measured Saharan dust plume and the role of large particles. Atmospheric Chemistry and Physics 7:4887-4903.

Pachauri, T., Singla, V., Satsangi, A., Lakhani, A., Kumari, K. M. (2013). SEM-EDX characterization of individual coarse particles in Agra, India. Aerosol and Air Quality Research 13:523-536.

Parajuli, S. P., Zobeck, T. M., Kocurek, G., Yang, Z.-L., Stenchikov, G. L. (2016). New insights into the wind-dust relationship in sandblasting and direct aerodynamic entrainment from wind tunnel experiments. Journal of Geophysical Research: Atmospheres 121:1776-1792.

Pardess, D., Levin, Z., Ganor, E. (1992). A new method for measuring the mass of sulfur in single aerosol particles. Atmospheric Environment Part A General Topics 26:675-680.

Pearce, N. J., Perkins, W. T., Westgate, J. A., Gorton, M. P., Jackson, S. E., Neal, C. R., Chenery, S. P. (1997). A compilation of new and published major and trace element data for NIST SRM 610 and NIST SRM 612 glass reference materials. Geostandards Newsletter 21:115-144.

Pearce, N. J., Westgate, J. A., Gatti, E., Pattan, J. N., Parthiban, G., Achyuthan, H. (2014). Individual glass shard trace element analyses confirm that all known Toba tephra

reported from India is from the c. 75-ka Youngest Toba eruption. Journal of Quaternary Science 29:729-734.
Pearce, N. J. G., Perkins, W. T., Westgate, J. A., Wade, S. C. (2011). Trace-element microanalysis by LA-ICP-MS: The quest for comprehensive chemical characterisation of single, sub-10 µm volcanic glass shards. Quaternary International 246:57-81.
Pekney, N. J. and Davidson, C. I. (2005). Determination of trace elements in ambient aerosol samples. Analytica Chimica Acta 540:269-277.
Perkin-Elmer (2001). The 30-Minute Guide to ICP-MS, Electronic Document. www. perkinelmer. com/Catalog/CategoryPage. htm.
Phalen, R., G Cuddihy, R., Fisher, G. L., Moss, O. R., Schlesinger, R. B., L Swift, D., C Yeh, H. (1991). Main Features of the Proposed NCRP Respiratory Tract Model. Radiation Protection Dosimetry 38.
Pongratz, R. (1998). Arsenic speciation in environmental samples of contaminated soil. Science of The Total Environment 224:133-141.
Posacka, A. M., Semeniuk, D. M., Whitby, H., van den Berg, C. M., Cullen, J. T., Orians, K., Maldonado, M. T. (2017). Dissolved copper (dCu) biogeochemical cycling in the subarctic Northeast Pacific and a call for improving methodologies. Marine Chemistry 196:47-61.
Prospero, J. (1999a). Long-range transport of mineral dust in the global atmosphere: Impact of African dust on the environment of the southeastern United States. Proceedings of the National Academy of Sciences 96:3396-3403.
Prospero, J. (1999b). Long-term measurements of the transport of African mineral dust to the southeastern United States: Implications for regional air quality. Journal of Geophysical Research: Atmospheres 104:15917-15927.
Prospero, J. M. (1999c). Long-range transport of mineral dust in the global atmosphere: Impact of African dust on the environment of the southeastern United States. Proceedings of the National Academy of Sciences 96:3396-3403.
Prospero, J. M., Nees, R. T., Uematsu, M. (1987). Deposition rate of particulate and dissolved aluminum derived from saharan dust in precipitation at Miami, Florida. Journal of Geophysical Research: Atmospheres 92:14723-14731.
Qian, Y., Yasunari, T. J., Doherty, S. J., Flanner, M. G., Lau, W. K. M., Ming, J., Wang, H., Wang, M., Warren, S. G., Zhang, R. (2015). Light-absorbing particles in snow and ice: Measurement and modeling of climatic and hydrological impact. Advances in Atmospheric Sciences 32:64-91.
R. Osborne, S., Johnson, B. T., Haywood, J., Baran, A., A. J. Harrison, M., Ryder, C. (2008). Physical and optical properties of mineral dust aerosol during the Dust and Biomass-burning Experiment (DABEX). Journal of Geophysical Research: Atmospheres 113.
Reid Jeffrey, S., Reid Elizabeth, A., Walker, A., Piketh, S., Cliff, S., Al Mandoos, A., Tsay, S. C., Eck Thomas, F. (2008). Dynamics of southwest Asian dust particle size characteristics with implications for global dust research. Journal of Geophysical Research: Atmospheres 113.
Resano, M., García-Ruiz, E., Vanhaecke, F. (2010). Laser ablation-inductively coupled plasma mass spectrometry in archaeometric research. Mass Spectrometry Reviews 29:55-78.

Richon, C., Dutay, J. C., Dulac, F., Wang, R., Balkanski, Y. (2018). Modeling the biogeochemical impact of atmospheric phosphate deposition from desert dust and combustion sources to the Mediterranean Sea. Biogeosciences 15:2499-2524.

Rosenberg, P. D., Dean, A. R., Williams, P. I., Dorsey, J. R., Minikin, A., Pickering, M. A., Petzold, A. (2012). Particle sizing calibration with refractive index correction for light scattering optical particle counters and impacts upon PCASP and CDP data collected during the Fennec campaign. Atmos Meas Tech 5:1147-1163.

Ryder, C. L., Marenco, F., Brooke, J. K., Estelles, V., Cotton, R., Formenti, P., McQuaid, J. B., Price, H. C., Liu, D., Ausset, P., Rosenberg, P. D., Taylor, J. W., Choularton, T., Bower, K., Coe, H., Gallagher, M., Crosier, J., Lloyd, G., Highwood, E. J., Murray, B. J. (2018). Coarse-mode mineral dust size distributions, composition and optical properties from AER-D aircraft measurements over the tropical eastern Atlantic. Atmos Chem Phys 18:17225-17257.

Schroth, A. V., Crusius, J., Gasso, S., Moy, C. M., Buck, N. J., Resing, J. A., Campbell, R. W. (2017). Position of Aleutian Low Drives Dramatic Inter-Annual Variability in Atmospheric Transport of Glacial Iron to the Gulf of Alaska.

Schroth, A. W., Crusius, J., Sholkovitz, E. R., Bostick, B. C. (2009). Iron solubility driven by speciation in dust sources to the ocean. Nature Geoscience 2:337.

Schulz, M., Prospero, J. M., Baker, A. R., Dentener, F., Ickes, L., Liss, P. S., Mahowald, N. M., Nickovic, S., García-Pando, C. P., Rodríguez, S., Sarin, M., Tegen, I., Duce, R. A. (2012). Atmospheric Transport and Deposition of Mineral Dust to the Ocean: Implications for Research Needs. Environmental Science & Technology 46:10390-10404.

Seinfeld, J. and Pandis, S. (2006). Atmospheric Chemistry and Physics, A Wiley-Inter Science Publication, John Wiley & Sons Inc, New York.

Shao, Y. (2001). A model for mineral dust emission. Journal of Geophysical Research: Atmospheres 106:20239-20254.

Shao, Y. (2008). Physics and modelling of wind erosion. Springer Science & Business Media.

Shelley, R. U., Sedwick, P. N., Bibby, T. S., Cabedo-Sanz, P., Church, T. M., Johnson, R. J., Macey, A., Marsay, C. M., Sholkovitz, E. R., Ussher, S. J. (2012). Controls on dissolved cobalt in surface waters of the Sargasso Sea: Comparisons with iron and aluminum. Global Biogeochemical Cycles 26.

Shi, Z., Krom, M. D., Bonneville, S., Baker, A. R., Jickells, T. D., Benning, L. G. (2009). Formation of Iron Nanoparticles and Increase in Iron Reactivity in Mineral Dust during Simulated Cloud Processing. Environmental Science & Technology 43:6592-6596.

Shi, Z., Krom, M. D., Bonneville, S., Benning, L. G. (2015). Atmospheric Processing Outside Clouds Increases Soluble Iron in Mineral Dust. Environmental Science & Technology 49:1472-1477.

Shugar, D. H., Clague, J. J., Best, J. L., Schoof, C., Willis, M. J., Copland, L., Roe, G. H. (2017). River piracy and drainage basin reorganization led by climate-driven glacier retreat. Nature Geoscience 10:370.

Sigel, A., Sigel, H., Sigel, R. K. (2007). Nickel and its surprising impact in nature. John Wiley & Sons.

Skoog, D. A., West, D. M., Holler, F. J., Crouch, S. R. (2013). Fundamentals of analytical chemistry. Nelson Education.
Smart, C. and Willis, E. (1967). Determination of refractive indices of polystyrene latices by light scattering. Journal of Colloid and Interface Science 25:577-583.
Sokolik, I. N. and Toon, O. B. (1996). Direct radiative forcing by anthropogenic airborne mineral aerosols. Nature 381:681.
Stocker, T. (2014). Climate change 2013: the physical science basis: Working Group I contribution to the Fifth assessment report of the Intergovernmental Panel on Climate Change. Cambridge University Press.
Stocker, T. F., Qin, D., Plattner, G., Tignor, M., Allen, S., Boschung, J., Nauels, A., Xia, Y., Bex, V., Midgley, P. (2013). Climate change 2013: the physical science basis. Intergovernmental panel on climate change, working group I contribution to the IPCC fifth assessment report (AR5). New York.
Stuut, J.-B., Smalley, I., O'Hara-Dhand, K. (2009). Aeolian dust in Europe: African sources and European deposits. Quaternary International 198:234-245.
Sullivan, R., Moore, M., Petters, M., Kreidenweis, S., Roberts, G., Prather, K. (2009). Effect of chemical mixing state on the hygroscopicity and cloud nucleation properties of calcium mineral dust particles. Atmospheric Chemistry and Physics 9:3303-3316.
Tegen, I. and Fung, I. (1994). Modeling of mineral dust in the atmosphere: Sources, transport, and optical thickness. Journal of Geophysical Research: Atmospheres 99:22897-22914.
Thevenon, F., Anselmetti, F. S., Bernasconi, S. M., Schwikowski, M. (2009). Mineral dust and elemental black carbon records from an Alpine ice core (Colle Gnifetti glacier) over the last millennium. Journal of Geophysical Research: Atmospheres 114.
Thornton, I. (1996). Sources and pathways of arsenic in the geochemical environment: health implications. Geological Society London Special Publications 113:153-161.
TSI (2013). Aerosol Instrument Manager® Software for Aerodynamic Particle Sizer (APS™) Spectrometers, T. Instruments, ed., Shoreview, MN.
Usher, C. R., Al-Hosney, H., Carlos-Cuellar, S., Grassian, V. H. (2002). A laboratory study of the heterogeneous uptake and oxidation of sulfur dioxide on mineral dust particles. Journal of Geophysical Research: Atmospheres 107(D23):ACH 16.
Von der Weiden, S., Drewnick, F., Borrmann, S. J. A. M. T. (2009). Particle Loss Calculator–a new software tool for the assessment of the performance of aerosol inlet systems. Atmos Meas Tech 2:479-494.
WHO (2006). WHO Air quality guidelines for particulate matter, ozone, nitrogen dioxide and sulfur dioxide-Global update 2005 - Summary of risk assessment, 2006, W. H. Organization, ed.
Witte, C.-P. (2011). Urea metabolism in plants. Plant Science 180:431-438.
Yang, M., Howell, S. G., Zhuang, J., Huebert, B. J. (2009). Attribution of aerosol light absorption to black carbon, brown carbon, and dust in China – interpretations of atmospheric measurements during EAST-AIRE. Atmos Chem Phys 9:2035-2050.

Ye, Y. and Völker, C. (2017). On the Role of Dust-Deposited Lithogenic Particles for Iron Cycling in the Tropical and Subtropical Atlantic. Global Biogeochemical Cycles 31:1543-1558.

Zdanowicz, C., Hall, G., Vaive, J., Amelin, Y., Percival, J., Girard, I., Biscaye, P., Bory, A. (2006). Asian dustfall in the St. Elias Mountains, Yukon, Canada. Geochimica et Cosmochimica Acta 70:3493-3507.

Zhang, L., Kok, J. F., Henze, D. K., Li, Q., Zhao, C. (2013). Improving simulations of fine dust surface concentrations over the western United States by optimizing the particle size distribution. Geophysical Research Letters 40:3270-3275.

Zhao, X. SEM-EDX Analysis of Atmospheric Aerosols, in Rochester Symposium for Physics Students, Union College, Schenectady, NY.

Appendix A: Vertical Aerosol Flux Calculations – Gillette et al. 1972

Kluane 2018_1 - Igor Pro 6.37 - [Kluane 2018 toolz_backup Sept 25.ipf]

File Edit Data Analysis Macros Windows Procedure Misc Help

```
//// ------------ Dust Flux Calculations ------------ \\\\

Function VerticalAerosolFlux(CUP_WS_ARA_2m_FilterTimeRegrid,CUP_WS_ARA_6m_FilterTimeRegrid, weather_datetime,grav_DV_2m,grav_DV_6m)
// VerticalAerosolFlux(CUP_WS_ARA_2m_RegridFilters,CUP_WS_ms_4_Avg_RegridFilters, Weather_Filtertimes_START,grav_DV_2m,grav_DV_6m)
	Wave CUP_WS_ARA_2m_FilterTimeRegrid // u1
	Wave CUP_WS_ARA_6m_FilterTimeRegrid // u2, assuming it's really anemometer #5 (h = 5.95 m)
	Wave weather_datetime // time
	Wave grav_DV_2m, grav_DV_6m // n1 and n2, in ug/m3

	Variable C_drag_coeff // drag coefficient, Priestly, 1959

	Make/o/n=(numpnts(CUP_WS_ARA_2m_FilterTimeRegrid)) F_a_VertAeroFlux

	Variable i // index on gravimetric data
	Variable j // index on weather data
	Variable u_1, u_2, n_1, n_2

	for(j=j;j<numpnts(grav_DV_2m);j+=1)
		u_1 = CUP_WS_ARA_2m_FilterTimeRegrid[j]
		u_2 = CUP_WS_ARA_6m_FilterTimeRegrid[j]
		n_1 = grav_DV_2m[j]
		n_2 = grav_DV_6m[j]

		C_drag_coeff = (0.4^2 / (ln(5.95/2.63))^2) * ( (u_2/u_1)^2 - (2*(u_2/u_1)) +1)
//		If(numtype(CUP_WS_ms_4_Avg[j]) ==0 && numtype(CUP_WS_ARA_2m[j]) ==0 && grav_DV_2m_weatherRegrid[j] >0 && grav_DV_6m_weatherRegrid>0)
			F_a_VertAeroFlux[j] = -(C_drag_coeff*(u_1^2)*(n_2 - n_1))/(u_2-u_1) // PM10 MASS FLUX
//		Else
//			F_a_VertAeroFlux[j] = NaN
//		EndIf
	EndFor
End
```

Kluane 2018_1 - Igor Pro 6.37 - [Kluane 2018 toolz_backup Sept 25.ipf]

File Edit Data Analysis Macros Windows Procedure Misc Help

```
Function VerticalTraceElementFlux()

	Wave May29_6m_RA_massfluxcalcs,May29_3m_RA_massfluxcalcs
	Wave May23_6m_RA_massfracForFlux,May23_3m_RA_massfracForFlux
	Wave/t icp_ms_elements

	//Get mass flux

	Make/o/n=(numpnts(May29_6m_RA_massfluxcalcs)) F_a_VertElementFlux_May29
	Make/o/n=(,numpnts(May23_6m_RA_massfracForFlux)) F_a_VertElementFlux_May23


	// Calculate flux of each metal. For Matrixes, the ROW is time and COLUMNS are metals

	Variable C_drag_coeff // drag coefficient, Priestly, 1959
	Variable u_1_0523, u_2_0523
	Variable u_1_0529, u_2_0529

	u_1_0523 = 4.57415; u_2_0523 = 5.4518 // avg windspeed on that day, m/s
	u_1_0529 = 5.2143; u_2_0529 = 5.81909 // m/s

	Variable pm10_massconc_3m_0529,pm10_massconc_6m_0529
	pm10_massconc_3m_0529 = 478.2160 ; pm10_massconc_6m_0529 = 963.0044

	Variable pm10_massconc_3m_0523,pm10_massconc_6m_0523
	pm10_massconc_3m_0523 = 1401.0405; pm10_massconc_6m_0523 = 692.8565

	Variable j // index on icp-ms data
	Variable n_1, n_2 // n1 is x_el at 3m; n2 is x_el at 6m
	Variable u_1, u_2 // u1 is ws at 3m, u2 is ws at 6m

	//May 29
	for(j=0;j<numpnts(May29_6m_RA_massfluxcalcs);j+=1)
		u_1 = u_1_0529; u_2 = u_2_0529
		n_1 = May29_3m_RA_massfluxcalcs[j] * pm10_massconc_3m_0529 * 10^-3 // ng/m3
		n_2 = May29_6m_RA_massfluxcalcs[j] * pm10_massconc_6m_0529 * 10^-3 // ng/m3
```

Kluane 2018_1 - Igor Pro 6.37 - [Kluane 2018 toolz_backup Sept 25.ipf]

File Edit Data Analysis Macros Windows Procedure Misc Help

```
        C_drag_coeff = (0.4^2 / (ln(5.95/2.63))^2) * ( (u_2/u_1)^2 - 2*u_2/u_1 +1)
        F_a_VertElementFlux_May29[j] = -(C_drag_coeff*(u_1^2)*(n_2 - n_1))/(u_2-u_1) // ELEMENT MASS FLUX

    EndFor

    //May 23
    for(j=0;j<numpnts(May23_6m_RA_massfracForFlux);j+=1)
        u_1 = u_1_0523; u_2 = u_2_0523
        n_1 = May23_3m_RA_massfracForFlux[j] * pm10_massconc_3m_0523 * 10^-3 // ng/m3
        n_2 = May23_6m_RA_massfracForFlux[j] * pm10_massconc_6m_0523 * 10^-3 // ng/m3

        C_drag_coeff = (0.4^2 / (ln(5.95/2.63))^2) * ( (u_2/u_1)^2 - 2*u_2/u_1 +1)
        F_a_VertElementFlux_May23[j] = -(C_drag_coeff*(u_1^2)*(n_2 - n_1))/(u_2-u_1) // ELEMENT MASS FLUX

    EndFor

//    Display F_a_VertElementFlux_May23 vs icp_ms_elements
//    AppendToGraph F_a_VertElementFlux_May29 vs icp_ms_elements
End
```

Appendix B: Vertical Aerosol Flux Calculations – Ginoux et al. 2001

```
Function VerticalFlux()

    Variable S_source_function, z_max, z_min, z_i // SOURCE FUNCTION
    S_source_function = 1 // set z_i = z_min

    // Ginoux only, with Kok 2011mod, or with TeamDust mod? If you want Ginoux, turn both OFF
    Variable Kok_mod
    //Kok_mod = 1 // mod ON
    Kok_mod = -1 // mod OFF

    Variable TeamDust_mod
    //TeamDust_mod = 1 // mod ON
    TeamDust_mod = -1 // mod OFF
    If(TeamDust_mod ==1)
    TeamDust_PSD()
    Wave massFracOfEachClass
    EndIf

    // Set threshold velocity manually?
```

```
Variable u_t_switch, u_t_manual_value

u_t_switch = 1 // set u_t manually when on, off = -1

u_t_manual_value = 7


Wave Roughness_Length, CUP_WS_ms_6m_Avg, Shear_Velocity // import all Table 10 waves

// ---------------------------------------------- Dry Deposition ---------------------------------- \\

Make/o/n=(numpnts(Roughness_Length)) v_hat_d // effective dry dep velocity

Make/o/n=(numpnts(Roughness_Length)) v_d // deposition velocity NEED HALP


//Gravitational Settling

Make/o/n=(numpnts(Roughness_Length)) v_stk_1

// ---------------------------- Size Class 1: 0.1 - 0.18 um, eff. radius = 0.15 ---------------------- \\

Make/o/n=(numpnts(Roughness_Length)) Flux_p_1 // FLUX of particle size class p

Make/o/n=(numpnts(Roughness_Length)) u_10m

Make/o/d/n=(numpnts(Roughness_Length)) u_t_1

Variable C_dim_factor,s_p, i

C_dim_factor = 1 //ug s^2 m^-5


u_10m = NaN

For(i=0;i<numpnts(Roughness_Length); i+=1) // find the windspeed at 10 m from that at 6m

if(numtype(Roughness_Length[i])==0)
```

```
		u_10m[i] = (Shear_Velocity[i]/0.41)* (ln( 10/Roughness_Length[i])) // assuming stable conditions & zero plane displacement = 0
	EndIf
	EndFor
	Variable A_param,phi_p_1, acc_grav, rho_particle
	Variable w_surface_wetness
	w_surface_wetness = 0.050 // can also input wave from field data
	A_param = 6.5
	phi_p_1 = 0.15 *10^-6 // radius in m
	acc_grav = 9.80665 // m/s^2
	rho_particle = 2.6*10^3 // kg/m3 (ie, 2.6 g/cm3)
//CALCULATE AIR DENSITY
	Wave AirTC_Avg_1_5m, rel_humidity_1_5m, BP_mb
	Duplicate/o BP_mb, BP_Pa
	BP_Pa = BP_mb*100
	Make/o/n=(numpnts(Roughness_Length)) rho_air
	Make/o/d/n=(numpnts(Roughness_Length)) p_sat //saturation vap pressure
	Variable AirTemp_K
	For(i=0;i<numpnts(Roughness_Length); i+=1) // calculating the air density
		if(numtype(AirTC_Avg_1_5m[i])==0 && numtype(BP_Pa[i])==0)
		p_sat[i] = 6.1078*10^((7.5*AirTC_Avg_1_5m[i])/(237.15+AirTC_Avg_1_5m[i])) // in mb
		p_sat[i] = p_sat[i] // in Pa but got rid of conversion bc of RH
		AirTemp_K = AirTC_Avg_1_5m[i] + 273.15 // convert celcius to kelvin
```

```
        rho_air[i] = ((rel_humidity_1_5m[i]*p_sat[i])/(461.495*AirTemp_K)) + ((BP_Pa[i] - (rel_humidity_1_5m[i]*p_sat[i]))/(287.058*AirTemp_K)) // kg/m3
        Else
        p_sat[i] = NaN
        rho_air[i] = NaN
        EndIf
    EndFor

        u_t_1 = NaN
    For(i=0;i<numpnts(Roughness_Length); i+=1) // calculating the threshold windspeed
    if(numtype(rho_air[i])==0)
        u_t_1[i] = A_param*sqrt( ((rho_particle - rho_air[i])/rho_air[i])*acc_grav*phi_p_1*2)*(1.2+0.2*log(w_surface_wetness))
    endif
    EndFor

    s_p = 0.122*.25
    If(Kok_mod == 1 && TeamDust_mod!=1)
        s_p = 0.048*0.005
    ElseIf(TeamDust_mod==1 && Kok_mod != 1)
        s_p = massFracOfEachClass[0]
    ElseIf(Kok_mod == 1 && TeamDust_mod==1)
        Print "Where the PSD is concerned, you don't know what you want. So, I am just going to use the Ginoux."
```

```
	EndIf


	Flux_p_1 = NaN
	Variable V_u_10m, V_u_t
	For(i=0;i<numpnts(Roughness_Length); i+=1) // calculating the flux of size class 1
	if(numtype(u_10m[i])==0 && numtype(u_t_1[i])==0)
	If(u_10m[i] > u_t_1[i] && u_t_switch <0) // manual entry is OFF
		V_u_10m = u_10m[i]; V_u_t = u_t_1[i]
		Flux_p_1[i]  =flux_param(C_dim_factor,  S_source_function,  s_p,V_u_10m,
V_u_t)
	ElseIf(u_10m[i] > u_t_manual_value)
		V_u_10m = u_10m[i]; V_u_t = u_t_manual_value
		Flux_p_1[i]  =flux_param(C_dim_factor,  S_source_function,  s_p,V_u_10m,
V_u_t)
	EndIf
	EndIf
	EndFor
	//Gravitational Settling
	Make/o/n=(numpnts(Roughness_Length)) v_stk_1
	v_stk_1 = gravitational_settling(AirTC_Avg_1_5m, BP_Pa, phi_P_1)



	// ---------------------------- Size Class 2: 0.18 - 0.30 um, eff. radius = 0.25 ------------------
--------- \\
```

```
Make/o/n=(numpnts(Roughness_Length)) u_t_2 // threshold velocity of particle size class p
Make/o/n=(numpnts(Roughness_Length)) Flux_p_2 // FLUX of particle size class p
Variable phi_p_2
phi_p_2 = 0.25*10^-6 // radius in m

    u_t_2 = NaN
For(i=0;i<numpnts(Roughness_Length); i+=1) // calculating the threshold windspeed
if(numtype(rho_air[i])==0)
    u_t_2[i] = A_param*sqrt( ((rho_particle - rho_air[i])/rho_air[i])*acc_grav*phi_p_2*2)*(1.2+0.2*log(w_surface_wetness))
endif

EndFor
s_p = 0.122*.25
If(Kok_mod == 1 && TeamDust_mod!=1)
    s_p = 0.048*0.026
ElseIf(TeamDust_mod==1 && Kok_mod != 1)
    s_p = massFracOfEachClass[1]
EndIf

Flux_p_2 = NaN
For(i=0;i<numpnts(Roughness_Length); i+=1) // calculating the flux of size class 1
if(numtype(u_10m[i])==0 && numtype(u_t_2[i])==0)
```

```
If(u_10m[i] > u_t_2[i] && u_t_switch<0) // manual entry is OFF
        V_u_10m = u_10m[i]; V_u_t = u_t_2[i]
        Flux_p_2[i] = flux_param(C_dim_factor, S_source_function, s_p,V_u_10m, V_u_t)
ElseIf(u_10m[i] > u_t_manual_value)
        V_u_10m = u_10m[i]; V_u_t = u_t_manual_value
        Flux_p_2[i] = flux_param(C_dim_factor, S_source_function, s_p,V_u_10m, V_u_t)
EndIf
EndIf
EndFor
//Gravitational Settling
Make/o/n=(numpnts(Roughness_Length)) v_stk_2
v_stk_2 = gravitational_settling(AirTC_Avg_1_5m, BP_Pa, phi_p_2)

        // ---------------------------- Size Class 3: 0.30 - 0.60 um, eff. radius = 0.40 ---------- \\
Make/o/n=(numpnts(Roughness_Length)) u_t_3 // threshold velocity of particle size class p
Make/o/n=(numpnts(Roughness_Length)) Flux_p_3 // FLUX of particle size class p
Variable phi_p_3
phi_p_3 = 0.40 *10^-6 // radius in m

        u_t_3 = NaN
For(i=0;i<numpnts(Roughness_Length); i+=1) // calculating the threshold windspeed
```

```
if(numtype(rho_air[i])==0)
        u_t_3[i] = A_param*sqrt( ((rho_particle - rho_air[i])/rho_air[i])*acc_grav*phi_p_3*2)*(1.2+0.2*log(w_surface_wetness))
endif
EndFor

s_p = 0.122*.25
If(Kok_mod == 1 && TeamDust_mod!=1)
        s_p = 0.048*0.192
ElseIf(Kok_mod != 1 && TeamDust_mod==1)
        s_p = massFracOfEachClass[2]
EndIf

Flux_p_3 = NaN
For(i=0;i<numpnts(Roughness_Length); i+=1) // calculating the flux of size class 3
if(numtype(u_10m[i])==0 && numtype(u_t_3[i])==0)
If(u_10m[i] > u_t_3[i] && u_t_switch<0) // manual entry is OFF
        V_u_10m = u_10m[i]; V_u_t = u_t_3[i]
        Flux_p_3[i] =flux_param(C_dim_factor, S_source_function, s_p,V_u_10m, V_u_t)
ElseIf(u_10m[i] > u_t_manual_value)
        V_u_10m = u_10m[i]; V_u_t = u_t_manual_value
        Flux_p_3[i] =flux_param(C_dim_factor, S_source_function, s_p,V_u_10m, V_u_t)
```

```
EndIf
EndIf
EndFor

//Gravitational Settling
Make/o/n=(numpnts(Roughness_Length)) v_stk_3
v_stk_3 = gravitational_settling(AirTC_Avg_1_5m, BP_Pa, phi_p_3)

        // ---------------------------- Size Class 4: 0.60 - 1.0 um, eff. radius = 0.80 ----------
---------- \\
Make/o/n=(numpnts(Roughness_Length)) u_t_4 // threshold velocity of particle size class p
Make/o/n=(numpnts(Roughness_Length)) Flux_p_4 // FLUX of particle size class p
Variable phi_p_4
phi_p_4 = 0.80 *10^-6 // radius in m

        u_t_4 = NaN
For(i=0;i<numpnts(Roughness_Length); i+=1) // calculating the threshold windspeed
if(numtype(rho_air[i])==0)
        u_t_4[i] = A_param*sqrt( ((rho_particle - rho_air[i])/rho_air[i])*acc_grav*phi_p_4*2)*(1.2+0.2*log(w_surface_wetness))
endif
EndFor
```

```
s_p = 0.122*.25
If(Kok_mod == 1 && TeamDust_mod!=1)
        s_p = 0.048*0.777
ElseIf(Kok_mod != 1 && TeamDust_mod==1)
        s_p = massFracOfEachClass[3]
EndIf

Flux_p_4 = NaN
For(i=0;i<numpnts(Roughness_Length); i+=1) // calculating the flux of size class 1
if(numtype(u_10m[i])==0 && numtype(u_t_4[i])==0)
If(u_10m[i] > u_t_4[i] && u_t_switch<0) // manual entry is OFF
        V_u_10m = u_10m[i]; V_u_t = u_t_4[i]
        Flux_p_4[i] = flux_param(C_dim_factor, S_source_function, s_p,V_u_10m, V_u_t)
ElseIf(u_10m[i] > u_t_manual_value)
        V_u_10m = u_10m[i]; V_u_t = u_t_manual_value
        Flux_p_4[i] = C_dim_factor*S_source_function*s_p*(u_10m[i]^2)*(u_10m[i] - u_t_manual_value)
EndIf
EndIf
EndFor

//Gravitational Settling
Make/o/n=(numpnts(Roughness_Length)) v_stk_4
```

```
v_stk_4 = gravitational_settling(AirTC_Avg_1_5m, BP_Pa, phi_p_4)
        // ---------------------------- Size Class 5: 1.0 - 1.8 um, eff. radius = 1.5 ----------
---------- \\
Make/o/n=(numpnts(Roughness_Length)) u_t_5 // threshold velocity of particle size
class p
Make/o/n=(numpnts(Roughness_Length)) Flux_p_5 // FLUX of particle size class p
Variable phi_p_5
phi_p_5 = 1.5 *10^-6 // radius in m


        u_t_5 = NaN
For(i=0;i<numpnts(Roughness_Length); i+=1) // calculating the threshold windspeed
if(numtype(rho_air[i])==0)
        u_t_5[i]        =        A_param*sqrt(        ((rho_particle        -
rho_air[i])/rho_air[i])*acc_grav*phi_p_5*2)*(1.2+0.2*log(w_surface_wetness))
endif
EndFor


s_p = 0.253
If(Kok_mod == 1 && TeamDust_mod!=1)
        s_p = 0.125
ElseIf(Kok_mod != 1 && TeamDust_mod==1)
        s_p = massFracOfEachClass[4]
EndIf
```

```
Flux_p_5 = NaN
For(i=0;i<numpnts(Roughness_Length); i+=1) // calculating the flux of size class 1
if(numtype(u_10m[i])==0 && numtype(u_t_5[i])==0)
If(u_10m[i] > u_t_5[i] && u_t_switch<0) // manual entry is OFF
        V_u_10m = u_10m[i]; V_u_t = u_t_5[i]
        Flux_p_5[i] = flux_param(C_dim_factor, S_source_function, s_p,V_u_10m, V_u_t)
ElseIf(u_10m[i] > u_t_manual_value)
        V_u_10m = u_10m[i]; V_u_t = u_t_manual_value
        Flux_p_5[i] = flux_param(C_dim_factor, S_source_function, s_p,V_u_10m, V_u_t)
EndIf
EndIf
EndFor

//Gravitational Settling
Make/o/n=(numpnts(Roughness_Length)) v_stk_5
v_stk_5 = gravitational_settling(AirTC_Avg_1_5m, BP_Pa, phi_p_5)

        // ---------------------------- Size Class 6: 1.8 - 3.0 um, eff. radius = 2.5 ---------- \\
Make/o/n=(numpnts(Roughness_Length)) u_t_6 // threshold velocity of particle size class p
Make/o/n=(numpnts(Roughness_Length)) Flux_p_6 // FLUX of particle size class p
Variable phi_p_6
```

```
phi_p_6 = 2.5 *10^-6 // radius in m

        u_t_6 = NaN
For(i=0;i<numpnts(Roughness_Length); i+=1) // calculating the threshold windspeed
if(numtype(rho_air[i])==0)
        u_t_6[i] = A_param*sqrt( ((rho_particle - rho_air[i])/rho_air[i])*acc_grav*phi_p_6*2)*(1.2+0.2*log(w_surface_wetness))
endif
EndFor

s_p = 0.322
If(Kok_mod == 1 && TeamDust_mod!=1)
        s_p = 0.257
ElseIf(Kok_mod != 1 && TeamDust_mod==1)
        s_p = massFracOfEachClass[5]
EndIf

Flux_p_6 = NaN
For(i=0;i<numpnts(Roughness_Length); i+=1) // calculating the flux of size class 1
if(numtype(u_10m[i])==0 && numtype(u_t_6[i])==0)
If(u_10m[i] > u_t_6[i] && u_t_switch<0) // manual entry is OFF
        V_u_10m = u_10m[i]; V_u_t = u_t_6[i]
        Flux_p_6[i] = flux_param(C_dim_factor, S_source_function, s_p,V_u_10m, V_u_t)
```

```
ElseIf(u_10m[i] > u_t_manual_value)
        V_u_10m = u_10m[i]; V_u_t = u_t_manual_value
        Flux_p_6[i] = flux_param(C_dim_factor, S_source_function, s_p,V_u_10m, V_u_t)
EndIf
EndIf
EndFor

//Gravitational Settling
Make/o/n=(numpnts(Roughness_Length)) v_stk_6
v_stk_6 = gravitational_settling(AirTC_Avg_1_5m, BP_Pa, phi_p_6)
        // ---------------------------- Size Class 7: 3.0 - 6.0 um, eff. radius = 4.0 um ---------- \\
Make/o/n=(numpnts(Roughness_Length)) u_t_7 // threshold velocity of particle size class p
Make/o/n=(numpnts(Roughness_Length)) Flux_p_7 // FLUX of particle size class p
Variable phi_p_7
phi_p_7 = 4.0*10^-6 // radius in m
        u_t_7 = NaN
For(i=0;i<numpnts(Roughness_Length); i+=1) // calculating the threshold windspeed
if(numtype(rho_air[i])==0)
        u_t_7[i] = A_param*sqrt( ((rho_particle - rho_air[i])/rho_air[i])*acc_grav*phi_p_7*2)*(1.2+0.2*log(w_surface_wetness))
endif
EndFor
```

```
s_p = 0.302
If(Kok_mod == 1 && TeamDust_mod!=1)
        s_p = 0.570
ElseIf(Kok_mod != 1 && TeamDust_mod==1)
        s_p = massFracOfEachClass[6]
EndIf
Flux_p_7 = NaN
For(i=0;i<numpnts(Roughness_Length); i+=1) // calculating the flux of size class 1
if(numtype(u_10m[i])==0 && numtype(u_t_7[i])==0)
If(u_10m[i] > u_t_7[i] && u_t_switch<0) // manual entry is OFF
        V_u_10m = u_10m[i]; V_u_t = u_t_7[i]
        Flux_p_7[i] = flux_param(C_dim_factor, S_source_function, s_p,V_u_10m, V_u_t)
ElseIf(u_10m[i] > u_t_manual_value)
        V_u_10m = u_10m[i]; V_u_t = u_t_manual_value
        Flux_p_7[i] = flux_param(C_dim_factor, S_source_function, s_p,V_u_10m, V_u_t)
EndIf
EndIf
EndFor
//Gravitational Settling
Make/o/n=(numpnts(Roughness_Length)) v_stk_7
v_stk_7 = gravitational_settling(AirTC_Avg_1_5m, BP_Pa, phi_p_7)
```

```
// -------------------------- Get the total flux in ug / m^2 / s --------------------------
\\
	variable data_check
	For(i=0;i<numpnts(Roughness_Length);i+=1) // checking data
	if(numtype(Flux_p_1[i])==0 && numtype(Flux_p_2[i])==0 && numtype(Flux_p_3[i])==0 && numtype(Flux_p_4[i])==0 && numtype(Flux_p_5[i])==0 && numtype(Flux_p_6[i])==0 && numtype(Flux_p_7[i])==0)
	ElseIf(numtype(Flux_p_1[i])!=0 && numtype(Flux_p_2[i])!=0 && numtype(Flux_p_3[i])!=0 && numtype(Flux_p_4[i])!=0 && numtype(Flux_p_5[i])!=0 && numtype(Flux_p_6[i])!=0 && numtype(Flux_p_7[i])!=0)
	Else
		data_check = -1
	EndIf
	EndFor

	If(data_check == -1)
		print "data is not okay"
	endif

	compareModels(Kok_mod, TeamDust_mod, u_t_switch, u_t_manual_value)
End
Function compareModels(Kok_mod, TeamDust_mod, u_t_switch, u_t_manual_value)
	Variable Kok_mod, TeamDust_mod, u_t_switch, u_t_manual_value
	Wave Flux_p_1, Flux_p_2, Flux_p_3, Flux_p_4, Flux_p_5, Flux_p_6, Flux_p_7
```

```
	Wave v_stk_1, v_stk_2, v_stk_3, v_stk_4, v_stk_5, v_stk_6, v_stk_7
	Wave u_t_1, u_t_2, u_t_3, u_t_4, u_t_5, u_t_6, u_t_7
	Wave Roughness_Length

	Make/o/n=(numpnts(Flux_p_1)) Emission_all
	Make/o/n=(numpnts(Flux_p_1)) Vert_Flux_All
	Vert_Flux_All = NaN

	Variable i
	For(i=0;i<numpnts(Roughness_Length);i+=1)
	if(numtype(Flux_P_1[i])==0)
		Emission_all[i] = Flux_p_1[i] + Flux_p_2[i] + Flux_p_3[i] + Flux_p_4[i] + Flux_p_5[i] + Flux_p_6[i] + Flux_p_7[i]
		Vert_Flux_All[i] = (Flux_p_1[i] - v_stk_1[i]*Flux_p_1[i]) + (Flux_p_2[i] - v_stk_2[i]*Flux_p_2[i]) + (Flux_p_3[i] - v_stk_3[i]*Flux_p_3[i]) + (Flux_p_4[i] - v_stk_4[i]*Flux_p_4[i]) + (Flux_p_5[i] - v_stk_5[i]*Flux_p_5[i]) + (Flux_p_6[i] - v_stk_6[i]*Flux_p_6[i]) + (Flux_p_7[i] - v_stk_7[i]*Flux_p_7[i])
	EndIf
	EndFor
//
//	Wave weather_datetime, Weather_Filtertimes_START,Weather_Filtertimes_END
//	AMS_2_FTIR(weather_datetime,Flux_all_Ginoux, Weather_Filtertimes_START,Weather_Filtertimes_END,10,10)
//	Wave concwave_fil_avg
//	Duplicate/o concwave_fil_avg, Flux_filter_regrid_Ginoux
```

```
//RENAME based on PSD or U_t
	String EndOfWaveName
	EndOfWaveName = ""
	If(Kok_mod !=1 && TeamDust_mod !=1)
		EndOfWaveName = "_Ginoux"
	ElseIf(Kok_mod ==1 && TeamDust_mod ==1)
		EndOfWaveName = "_Ginoux"
	ElseIf(Kok_mod ==1 && TeamDust_mod !=1)
		EndOfWaveName = "_Kok"
	ElseIf(Kok_mod !=1 && TeamDust_mod ==1)
		EndOfWaveName = "_TeamDust"
	EndIf

	String nameThatWave

	if(u_t_switch < 0) // means manual entry is OFF
	nameThatWave = nameOfWave(Emission_all) + EndOfWaveName
	Duplicate/o Emission_all, $nameThatWave
	nameThatWave = nameOfWave(Vert_Flux_All) + EndOfWaveName
	Duplicate/o Vert_Flux_All, $nameThatWave
	Else
	nameThatWave = nameOfWave(Emission_all) + EndOfWaveName + "_"+num2str(u_t_manual_value) +"m_s"
	Duplicate/o Emission_all, $nameThatWave
```

```
nameThatWave = nameOfWave(Vert_Flux_All) + EndOfWaveName + "_"+num2str(u_t_manual_value) +"m_s"
Duplicate/o Vert_Flux_All, $nameThatWave
EndIf

// should calculate RMSE btwn Ginoux and Kok vs 6m and 3m

make/o/n=(numpnts(u_t_1)) u_t_overall

For(i=0;i<numpnts(u_t_1);i+=1)
    If(numtype(u_t_1[i])==2)
        u_t_overall[i] = NaN
    ELseIf(u_t_1[i]<u_t_2[i] && u_t_1[i]<u_t_3[i] && u_t_1[i]<u_t_4[i] && u_t_1[i]<u_t_5[i] && u_t_1[i]<u_t_6[i] && u_t_1[i]<u_t_7[i])
        u_t_overall[i] = u_t_1[i]
    ElseIf(u_t_2[i]<u_t_3[i] && u_t_2[i]<u_t_4[i] && u_t_2[i]<u_t_5[i] && u_t_2[i]<u_t_6[i] && u_t_2[i]<u_t_7[i] && u_t_2[i] < u_t_1[i])
        u_t_overall[i] = u_t_2[i]
    ElseIf(u_t_3[i]<u_t_1[i] && u_t_3[i]<u_t_4[i] && u_t_3[i]<u_t_5[i] && u_t_3[i]<u_t_6[i] && u_t_3[i]<u_t_7[i] && u_t_3[i] < u_t_2[i])
        u_t_overall[i] = u_t_3[i]
    ElseIf(u_t_4[i]<u_t_1[i] && u_t_4[i]<u_t_2[i] && u_t_4[i]<u_t_3[i] && u_t_4[i]<u_t_5[i] && u_t_4[i]<u_t_6[i] && u_t_4[i]<u_t_7[i])
        u_t_overall[i] = u_t_4[i]
```

```
		ElseIf(u_t_5[i]<u_t_1[i] && u_t_5[i]<u_t_3[i] && u_t_5[i]<u_t_4[i] && u_t_5[i]<u_t_2[i] && u_t_5[i]<u_t_6[i] && u_t_5[i]<u_t_7[i])
			u_t_overall[i] = u_t_5[i]
		ElseIf(u_t_6[i]<u_t_2[i] && u_t_6[i]<u_t_3[i] && u_t_6[i]<u_t_4[i] && u_t_6[i]<u_t_5[i] && u_t_6[i]<u_t_1[i] && u_t_6[i]<u_t_7[i])
			u_t_overall[i] = u_t_6[i]
		Else
			u_t_overall[i] = u_t_7[i]
		EndIf
	EndFor

	If(u_t_switch<0)
		Duplicate/o u_t_overall, u_t_fromGinoux
	Else
		nameThatWave = "u_t_" + num2str(u_t_manual_value)+"m_s"
		Duplicate/o u_t_overall, $nameThatWave
	EndIf
End
```

Appendix C: OPC Data Import and Processing

Kluane 2018_1 - Igor Pro 6.37 - [Kluane 2018 toolz_backup Sept 25.ipf]

File Edit Data Analysis Macros Windows Procedure Misc Help

```
#pragma rtGlobals=3        // Use modern global access method and strict wave access.

// All fOPC original data wave: all_fOPC_Matrix
// All fOPC original time wave: all_fOPC_twave

Function opcProcessData(numSpectra)
      Variable numSpectra // need to input how many spectra are being loaded
      DoLoadMultipleFiles() // select all waves you want to include

      //merge all data files together
      concatenateAllData(numSpectra)

End
```

Kluane 2018_1 - Igor Pro 6.37 - [Kluane 2018 toolz_backup Sept 25.ipf]

File Edit Data Analysis Macros Windows Procedure Misc Help

```
End


Function/S DoLoadMultipleFiles()
// Code copy pasted from the Igor Stack Exchange to load multiple files at once
 Variable refNum
 String message = "Select one or more files"
 String outputPaths
 String fileFilters = "Data Files (*.txt,*.dat,*.csv):.txt,.dat,.csv;"
 fileFilters += "All Files:.*;"

 Open /D /R /MULT=1 /F=fileFilters /M=message refNum
 outputPaths = S_fileName

 Wave/t dateFileNames_all
  String waveFileName

 if (strlen(outputPaths) == 0)
  Print "Cancelled"
 else
  Variable numFilesSelected = ItemsInList(outputPaths, "\r")

  Variable i
  for(i=0; i<numFilesSelected; i+=1)
   String path = StringFromList(i, outputPaths, "\r")
   Printf "%d: %s\r", i, path



   String filePath = ParseFilePath(3, path, ":", 0, 0)

   LoadWave/W/A/J/D/O/Q/C path // original was: LoadWave/a/D/J/O/W/K=1/M/U={0,0,1,0} path

   waveFileName = dateFileNames_all[i] // get the data into the good waves
   opcMergeColumns(waveFileName,i)
  endfor
 endif
```

Kluane 2018_1 - Igor Pro 6.37 - [Kluane 2018 toolz_backup Sept 25.ipf]

File Edit Data Analysis Macros Windows Procedure Misc Help

```
End

Function concatenateAllData(numSpectra) // putting all 6-hr matrices together to get one continuous dataset during sampling period
	Variable numSpectra
	String tempWaveName_Concatenate_matrix, tempWaveName_Concatenate_twave
	String tempWaveName_Concatenate_PM10,tempWaveName_Concatenate_PM2_5,tempWaveName_Concatenate_PM1
	String temp_gardOldTimes,temp_gardOldWaves, temp_gardOldPM10, temp_gardOldPM2_5,temp_gardOldPM1
	String all_matrix, all_twave, all_PM10, all_PM2_5, all_PM1
	tempWaveName_Concatenate_matrix = ""; temp_gardOldWaves = ""; temp_gardOldTimes = ""; temp_gardOldPM10="";temp_gardOldPM2_5 = "";temp_gardOldPM1=""

	Variable i
	For(i=0;i<numSpectra;i+=1)
		tempWaveName_Concatenate_matrix= "fOPC_conc_merged_"+num2str(i) +";"
		all_matrix = temp_gardOldWaves + tempWaveName_Concatenate_matrix
		temp_gardOldWaves = all_matrix

		tempWaveName_Concatenate_twave = "fOPC_datetime_"+num2str(i) + "; "
		all_twave = temp_gardOldTimes + tempWaveName_Concatenate_twave
		temp_gardOldTimes = all_twave
		//Concatenate/NP=0/O all_twave, all_fOPC_twave

		tempWaveName_Concatenate_pm10 = "fOPC_pm10massconc_"+num2str(i) + ";"
		all_PM10 = temp_gardOldPM10 + tempWaveName_Concatenate_pm10
		temp_gardOldPM10=all_PM10

	EndFor
	//print all_matrix
	//print all_twave
	//print all_PM10
	print all_twave

	Concatenate/NP=0/O all_matrix, all_fOPC_Matrix
	Concatenate/NP=0/O all_twave, all_fOPC_twave
	Concatenate/NP=0/O all_PM10, all_fOPC_PM10
End
```

Kluane 2018_1 - Igor Pro 6.37 - [Kluane 2018 toolz_backup Sept 25.ipf]

File Edit Data Analysis Macros Windows Procedure Misc Help

```
Function opcMergeColumns(YYYYMMDD, waveload_inc)
    String YYYYMMDD //sampling date
    Variable waveload_inc

    // FIRST, put all particle concentrations into the matrix
    // declaring waves loaded earlier
    Wave X0_28__m__part_l_, X0_40__m__part_l_,X0_45__m__part_l_,X0_50__m__part_l_
    Wave X0_60__m__part_l_,X0_70__m__part_l_,X0_80__m__part_l_,X0_90__m__part_l_
    Wave X10_00__m__part_l_,X1_10__m__part_l_,X1_60__m__part_l_,X2_00__m__part_l_
    Wave X2_50__m__part_l_, X3_00__m__part_l_,X3_50__m__part_l_,X4_00__m__part_l_
    Wave X5_00__m__part_l_,X6_00__m__part_l_,X0_65__m__part_l_,X7_00__m__part_l_,X8_00__m__part_l_
    Wave X9_00__m__part_l_,X10_00__m__part_l_

    Make/o/n=((numpnts(X0_28__m__part_l_)),22) fOPC_merged_conc // new matrix to store all particle concs

    Variable i
    For(i=0;i<(numpnts(X0_28__m__part_l_));i+=1)
        fOPC_merged_conc[i][0] = X0_28__m__part_l_[i]
        fOPC_merged_conc[i][1] = X0_40__m__part_l_[i]
        fOPC_merged_conc[i][2] = X0_45__m__part_l_[i]
        fOPC_merged_conc[i][3] = X0_50__m__part_l_[i]
        fOPC_merged_conc[i][4] = X0_60__m__part_l_[i]
        fOPC_merged_conc[i][5] = X0_65__m__part_l_[i]
        fOPC_merged_conc[i][6] = X0_70__m__part_l_[i]
        fOPC_merged_conc[i][7] = X0_80__m__part_l_[i]
        fOPC_merged_conc[i][8] = X0_90__m__part_l_[i]
        fOPC_merged_conc[i][9] = X1_10__m__part_l_[i]

        fOPC_merged_conc[i][10] = X1_60__m__part_l_[i]
        fOPC_merged_conc[i][11] = X2_00__m__part_l_[i]
        fOPC_merged_conc[i][12] = X2_50__m__part_l_[i]
        fOPC_merged_conc[i][13] = X3_00__m__part_l_[i]
        fOPC_merged_conc[i][14] = X3_50__m__part_l_[i]
        fOPC_merged_conc[i][15] = X4_00__m__part_l_[i]
        fOPC_merged_conc[i][16] = X5_00__m__part_l_[i]
        fOPC_merged_conc[i][17] = X6_00__m__part_l_[i]
```

Kluane 2018_1 - Igor Pro 6.37 - [Kluane 2018 toolz_backup Sept 25.ipf]

File Edit Data Analysis Macros Windows Procedure Misc Help

```
            fOPC_merged_conc[i][18] = X7_00__m__part_l_[i]
            fOPC_merged_conc[i][19] = X8_00__m__part_l_[i]
            fOPC_merged_conc[i][20] = X9_00__m__part_l_[i]
            fOPC_merged_conc[i][21] = X10_00__m__part_l_[i]
        EndFor

        // Make a date/time wave for this data
        Wave Hour__hh_mm_ss_, Date__mm_dd_yy_ // from Load function

        make/o/n=(dimsize(fOPC_merged_conc,0)+1)/d fOPC_datetime

        For(i=0;i<(numpnts(Hour__hh_mm_ss_));i+=1)
            fOPC_datetime[i] = Hour__hh_mm_ss_[i]+Date__mm_dd_yy_[i]
        EndFor
        // Process the PM10 and PM2.5 calculated mass concentrations

        Wave PM_10___g_m__, PM_2_5___g_m__,PM_1___g_m__

//      Variable avg_PM10, avg_Pm2_5, avg_PM1
//      avg_PM10 = mean(PM_10___g_m__)
//      avg_Pm2_5 = mean(PM_2_5___g_m__)
//      avg_PM1 = mean(PM_1___g_m__)
//
//      print "Average Pm10 on " + YYYYMMDD + " is " + num2str(avg_PM10)


        // Get data every second
        variable idex_delete
        For(i=1;i<numpnts(fOPC_datetime);i+=1)
            If(fOPC_datetime[i] == fOPC_datetime[i+1])
                idex_delete = i+1
                DeletePoints idex_delete,1, fOPC_datetime, fOPC_merged_conc,PM_10___g_m__,PM_2_5___g_m__,PM_1___g_m__
            ElseIf(fOPC_datetime[i] == fOPC_datetime[i-1])
                DeletePoints i,1, fOPC_datetime, fOPC_merged_conc,PM_10___g_m__,PM_2_5___g_m__,PM_1___g_m__
            ElseIf((fOPC_datetime[i] - fOPC_datetime[i-1]) == 0)
                DeletePoints i,1, fOPC_datetime, fOPC_merged_conc,PM_10___g_m__,PM_2_5___g_m__,PM_1___g_m__
            EndIf
```

Kluane 2018_1 - Igor Pro 6.37 - [Kluane 2018 toolz_backup Sept 25.ipf]

File Edit Data Analysis Macros Windows Procedure Misc Help

```
        EndFor

        idex_delete = numpnts(fOPC_datetime)-1
        DeletePoints idex_delete,1,fOPC_datetime


        // Rename all waves
        String new_filename
        new_filename = "fOPC_conc_merged_" + num2str(waveload_inc)
        Duplicate/o fOPC_merged_conc, $new_filename
        new_filename = "fOPC_datetime_" + num2str(waveload_inc)
        Duplicate/o fOPC_datetime, $new_filename
        String pm_rename
        pm_rename = "fOPC_pm10massconc_" + num2str(waveload_inc)
        Duplicate/o PM_10___g_m__, $pm_rename
        pm_rename = "fOPC_pm2_5massconc_" + num2str(waveload_inc)
        Duplicate/o PM_2_5___g_m__, $pm_rename
        pm_rename = "fOPC_pm1massconc_" + num2str(waveload_inc)
        Duplicate/o PM_1___g_m__, $pm_rename
End
```

Appendix D: OPC Data Analysis

Kluane 2018_1 - Igor Pro 6.37 - [Kluane 2018 toolz_backup Sept 25.ipf]

File Edit Data Analysis Macros Windows Procedure Misc Help

```
function makeSizeBinsAPS(particle_sizes)
	Wave particle_sizes
	Variable x
	x =  numpnts(particle_sizes)+1
	Make/o/n=(x) bins
	bins[0]=particle_sizes[0]
	//bins[1]=particle_sizes[1]
	Variable i
	For(i=1;i<numpnts(particle_sizes)-1;i+=1)
		bins[i]=(particle_sizes[i+1]+particle_sizes[i])/2
	endfor
	bins[numpnts(particle_sizes)] = (particle_sizes[numpnts(particle_sizes)-1] - particle_sizes[numpnts(particle_sizes)-2])+particle_sizes[numpnts(particle_sizes)-1]
end

function normalizetoBinSizes(vector1,matrix1)
	Wave vector1
	Wave matrix1
	Variable x
	x = numpnts(vector1)
	Variable x_1 = x-1
	Make/o/n=(dimsize(matrix1,0),dimsize(matrix1,1)) dNlogDp
	Variable i
	Variable j
	For(i=0;i<dimsize(matrix1,0);i+=1)
		For(j=0;j<numpnts(vector1)-1; j+=1)
			dNlogDp[i][j]=matrix1[i][j]/(log(vector1[j+1])-log(vector1[j]))
		endfor
	endfor
end
```

```
Function convert_dN_to_dM(sizeDias, dNmatrix) // takes the number conc output by OPC and coverts to a mass conc
	Wave sizeDias, dNmatrix // dias in um

	Variable i,j, massOneParticle

	Make/o/n=(dimsize(dNmatrix,0),dimsize(dNmatrix,1)) dMmatrix
	dMmatrix =3

	For(i=0;i<dimsize(dNmatrix,1);i+=1) // columns
	massOneParticle = ((4/3)*pi*((sizeDias[i]*0.0001)/2)^3)*2.6 // grams
		For(j=0;j<dimsize(dNmatrix,0);j+=1) // rows
			dMmatrix[j][i] = dNmatrix[j][i]*massOneParticle
		EndFor
	EndFor
	dMmatrix = dMmatrix*1000000 // convert from g to ug
	dMmatrix = dMmatrix*1000 // convert from ug/L to ug/m3
	String rename_dM = "dM_"+nameOfWave(dNmatrix)
	Duplicate/o dMmatrix, $rename_dM
End

Function getPM2_5_massconc(dM_matrix, particlesizes)
	Wave dM_matrix, particlesizes

	Variable i,j

	Make/o/n=(dimsize(dM_matrix,0)) massconc_PM10
	massconc_PM10 = 0
	For(i=0;i<numpnts(massconc_PM10);i+=1)
		For(j=0;j< dimsize(dM_matrix,1);j+=1)
		If(particlesizes[j] < 1112.2)
			massconc_PM10[i] = massconc_PM10[i] + dM_matrix[i][j]
		EndIf
		EndFor
```

Kluane 2018_1 - Igor Pro 6.37 - [Kluane 2018 toolz_backup Sept 25.ipf]

File Edit Data Analysis Macros Windows Procedure Misc Help

```
        EndFor
    EndFor
    dMmatrix = dMmatrix*1000000 // convert from g to ug
    dMmatrix = dMmatrix*1000 // convert from ug/L to ug/m3
    String rename_dM = "dM_"+nameOfWave(dNmatrix)
    Duplicate/o dMmatrix, $rename_dM
End

Function getPM2_5_massconc(dM_matrix, particlesizes)
    Wave dM_matrix, particlesizes

    Variable i,j

    Make/o/n=(dimsize(dM_matrix,0)) massconc_PM10
    massconc_PM10 = 0
    For(i=0;i<numpnts(massconc_PM10);i+=1)
        For(j=0;j< dimsize(dM_matrix,1);j+=1)
        If(particlesizes[j] < 1112.2)
            massconc_PM10[i] = massconc_PM10[i] + dM_matrix[i][j]
        EndIf
        EndFor
    EndFor

    massconc_PM10 = massconc_PM10*10^9

End
```

Kluane 2018_1 - Igor Pro 6.37 - [Kluane 2018 toolz_backup Sept 25.ipf]

File Edit Data Analysis Macros Windows Procedure Misc Help

```
// MASS CONCENTRATION FROM 5-min-resolution WAVE

Function massFromNumConc(sizeDia_um, all_fOPC_Matrix)
    Wave sizeDia_um, all_fOPC_Matrix
    // ORIGINAL DATA FILE IS IN particles/liter
    //    Convert size to cm
    Duplicate/o sizeDia_um, sizeDia_cm
    sizeDia_cm = sizeDia_um*0.0001

    // Density
    Variable rho_g_cm3 = 2.6 // in g /cm3
    Variable particle_mass

    //    Calculate mass in each cell
    Duplicate/o all_fOPC_Matrix, all_fOPC_Matrix_dM

    Variable i,j
    For(i=0;i<dimsize(all_fOPC_Matrix,1);i+=1) //cycle thru columns
        For(j=0;j<dimsize(all_fOPC_Matrix,0);j+=1) // cycle thru rows
            particle_mass =rho_g_cm3*(4/3)*pi*(sizeDia_cm[i]/2)^3
            // mass = #particles * volume 1 particle * density
            // mass = #particles * 4/3 pi r3 * density
            all_fOPC_Matrix_dM[j][i] = all_fOPC_Matrix[j][i]*particle_mass
        EndFor
    EndFor

    // Get PM10, PM2.5, PM1 waves

    Make/o/n=(dimsize(all_fOPC_Matrix,0)) all_PM10_fromdM
    Make/o/n=(dimsize(all_fOPC_Matrix,0)) all_PM2_5_fromdM
    Make/o/n=(dimsize(all_fOPC_Matrix,0)) all_PM1_fromdM
    all_PM10_fromdM=0
    all_PM2_5_fromdM=0
    all_PM1_fromdM=0

    For(j=0;j<dimsize(all_fOPC_Matrix,0);j+=1) // cycle thru rows
        For(i=0;i<dimsize(all_fOPC_Matrix,1);i+=1) //cycle thru columns
```

Kluane 2018_1 - Igor Pro 6.37 - [Kluane 2018 toolz_backup Sept 25.ipf]

File Edit Data Analysis Macros Windows Procedure Misc Help

```
        For(i=0;i<dimsize(all_fOPC_Matrix,1);i+=1) //cycle thru columns
            all_PM10_fromdM[j] = all_PM10_fromdM[j] +all_fOPC_Matrix_dM[j][i]

            If(sizeDia_um[i]<=1)
                all_PM1_fromdM[j] = all_PM1_fromdM[j] + all_fOPC_Matrix_dM[j][i]
            EndIf

            If(sizeDia_um[i]<=2.5)
                all_PM2_5_fromdM[j] = all_PM2_5_fromdM[j] + all_fOPC_Matrix_dM[j][i]
            EndIf
        EndFor
    EndFor

    // Convert to ug (from g)
    all_PM10_fromdM = all_PM10_fromdM*10^6
    all_PM2_5_fromdM = all_PM2_5_fromdM*10^6
    all_PM1_fromdM = all_PM1_fromdM*10^6

    // Convert to ug/m3 (from ug/L)
    all_PM10_fromdM = all_PM10_fromdM*1000
    all_PM2_5_fromdM = all_PM2_5_fromdM*1000
    all_PM1_fromdM = all_PM1_fromdM*1000

End

Function calc_PM2_5_from_PM10()
    Wave grav_VC_eastSlims, grav_VC_vc, grav_VC_island

    Duplicate/o grav_VC_eastSlims, grav_VC_eastSlims_PM2_5
    Duplicate/o grav_VC_vc, grav_VC_vc_PM2_5
    Duplicate/o grav_VC_island, grav_VC_island_PM2_5

    grav_VC_eastSlims_PM2_5 =11.911 + 0.2156*grav_VC_eastSlims // from 24-hr data  -51.852 + 0.32435*
    grav_VC_vc_PM2_5 =  11.911 + 0.2156*grav_VC_vc
    grav_VC_island_PM2_5 =  11.911 + 0.2156* grav_VC_island

End
```

```
Function OPC_data_conc_check()
    Wave grav_DV_2m, grav_DV_6m

    Variable i, param_coeff
    param_coeff = -0.53554

    //First do 2m
    Make/o/n=(numpnts(grav_DV_2m)) OPC_PM10_Check_From2mGrav
    For(i=0;i<numpnts(OPC_PM10_Check_From2mGrav);i+=1)
        OPC_PM10_Check_From2mGrav[i] = grav_DV_2m[i] * (param_coeff*ln(3.47/2.63) + 1)
    EndFor

    //Now do 6m
    Make/o/n=(numpnts(grav_DV_6m)) OPC_PM10_Check_From6mGrav
    For(i=0;i<numpnts(OPC_PM10_Check_From6mGrav);i+=1)
        OPC_PM10_Check_From6mGrav[i] = grav_DV_6m[i] * (param_coeff*ln(3.47/5.86) + 1)
    EndFor
End
```

Appendix E: Plotting SEM/EDS Spectra

```
Function plotSEMGraphs(numGraphs, stringList_filenames)
    Variable numGraphs
    Wave/t stringList_filenames


    //Declare all Perrine's waves
     Wave AtomicNumber, Xposition_keV
     Wave/t atomicElement
    Make/O/n=(numGraphs,numpnts(AtomicNumber)) peakMatrix // matrix for cluster analysis

    //Get x-wave
    String stringForXWave = "wave0"
    Duplicate/o $stringForXWave, waveToGetXVals
    Make/o/n=(dimsize(waveToGetXVals,0)) W_energy_keV

    Variable i
    For(i=0;i<numpnts(W_energy_keV);i+=1)
        W_energy_keV[i] = waveToGetXVals[i][0]
    EndFor
    Killwaves waveToGetXVals

    For(i=0;i<numgraphs;i+=1)
    Variable j,k,l,m

     //Get the waves we loaded with DoLoadMultipleFiles()
     String originalTextWave
     originalTextWave="textwave"+num2str(i)
     String originalNumericWave
     originalNumericWave = "wave"+num2str(i+1)

     //Get intensity wave
     Duplicate/o $originalNumericWave, numbersFromSpectra
     Make/o/n=(dimsize(numbersFromSpectra,0)) temp_waveIntensity
     For(j=0;j<dimsize(numbersFromSpectra,0);j+=1)
         temp_waveIntensity[j] = numbersFromSpectra[j][1]
     EndFor
```

Igor_SEM_analysis_final_Aug7_2018 - Igor Pro 6.37 - [Procedure]

File Edit Data Analysis Macros Windows Procedure Misc Help

```
     String reNameIntensity = "Spectrum_"+num2str(i+1)+"_intensity"
     Duplicate/o temp_waveIntensity, $reNameIntensity

     //Get correct elements
     Duplicate/o $originalTextWave, textForElements
     getCorrectElements(textForElements)
     Wave elementNumberInt //from ^^

    //kill original waves
    Killwaves $originalNumericWave, $originalTextWave

    //Delete duplicates from the correct metals
    For(j=(numpnts(elementNumberInt)-1); j>0;j-=1)
        If(elementNumberInt[j]==elementNumberInt[j]-1)
            elementNumberInt[j]=NaN
        EndIf
    EndFor

     // get rid of weird artefact element at the end of the file
     k=0
    For(j=0;j<numpnts(elementNumberInt);j+=1) // get how many integers there are
        If(elementNumberInt[j]>10)
        k+=1
        EndIf
    EndFor
    m=0

    For(j=0;j<numpnts(elementNumberInt);j+=1) // delete the last one
        If(numtype(elementNumberInt[j])==0)
        m+=1
        EndIf

        If(m==(k-1))
        elementNumberInt[j] = NaN
        ElseIf(m==k)
        elementNumberInt[j] = NaN
        break
```

Igor_SEM_analysis_final_Aug7_2018 - Igor Pro 6.37 - [Procedure]

File Edit Data Analysis Macros Windows Procedure Misc Help

```
        EndIf
    EndFor

    For(j=3;j<numpnts(elementNumberInt);j+=1) // double check duplicates
        For(m=0;m<j;m+=1)
            if(elementNumberInt[j]==elementNumberInt[m])
                elementNumberInt[j]=NaN
            EndIf
        EndFor
    EndFor

    Redimension/N=350 elementNumberInt

    // Duplicate Perrine's waves but extract only elements on spectra
    Make/o/n=(numpnts(XPosition_keV)) Xval_onSpect
    Make/o/n=(numpnts(XPosition_keV)) AtmNum_onSpect
    Make/o/t/n=(numpnts(XPosition_keV)) AtomicEl_onSpect
    Make/o/n=(numpnts(XPosition_keV)) flag_loc

                Xval_onSpect=NaN
                AtmNum_onSpect=NaN
                AtomicEl_onSpect=""
                flag_loc=NaN

    For(j=0;j<numpnts(XPosition_keV);j+=1) // value on x-val
        For(m=0;m<numpnts(elementNumberInt);m+=1) //value on wave from text wave
            //If(elementNumberInt[m]==79)
            If(numtype(elementNumberInt[m])==2)

            ElseIf(elementNumberInt[m]==AtomicNumber[j])
                Xval_onSpect[j] = XPosition_keV[j]
                AtmNum_onSpect[j] = AtomicNumber[j]
                AtomicEl_onSpect[j]=AtomicElement[j]
                flag_loc[j] = 1
                break
            EndIf
        EndFor
```

Igor_SEM_analysis_final_Aug7_2018 - Igor Pro 6.37 - [Procedure]

File Edit Data Analysis Macros Windows Procedure Misc Help

```
    EndFor

    // Get location of energy values on x axis
    //But, only plot values where peak is higher than ~ 400 counts
            //Reminder that x = W_energy_keV, y= temp_waveIntensity

    Make/o/n=(numpnts(XPosition_keV)) ptLoc_Energy_keV
    For(j=0;j<numpnts(XPosition_keV);j+=1)
        For(m=0;m<numpnts(W_energy_keV);m+=1)
            If(Xval_onSpect[j]==0)
            ElseIf((W_energy_keV[m]>=(Xval_onSpect[j]-0.005))&& (W_energy_keV[m]<=(Xval_onSpect[j]+0.004)))
                    ptLoc_Energy_keV[j]=m
            EndIf
        EndFor
    EndFor

    //Get rid of gold, carbon, and oxygen peaks
    For(j=0;j<numpnts(XPosition_keV);j+=1) // value on x-val
        If(AtomicNumber[j]==79) // gold
                Xval_onSpect[j] = 0
                flag_loc[j]=0
        ElseIf(AtomicNumber[j]==6) // carbon
                Xval_onSpect[j] = 0
                flag_loc[j]=0
        ElseIf(AtomicNumber[j]==8) // oxygen
                Xval_onSpect[j] = 0
                flag_loc[j]=0
        ElseIf(AtomicNumber[j]==76)
                Xval_onSpect[j] = 0
                flag_loc[j]=0
        EndIf
    EndFor

    //Make sure undesirable elements are deleted
    flag_loc[0]=0 // based on AtomicElement
    flag_loc[1]=0
    flag_loc[45]=0
```

Igor_SEM_analysis_final_Aug7_2018 - Igor Pro 6.37 - [Procedure]

File Edit Data Analysis Macros Windows Procedure Misc Help

```
    flag_loc[46]=0

     Make/o/n=(numpnts(flag_loc)) Intensity_onSpect = 0

    //Plot spectrum
    Variable flag_plots// =1
    flag_plots=1 //COMMENTIZE FOR CLUSTERING
    If(flag_plots==1)
    Display $reNameIntensity vs W_energy_keV // Formatting graphic
    Label left "Counts";DelayUpdate
    Label bottom "Energy (keV)"
    ModifyGraph mirror=2
    SetAxis left 0, 1.1*wavemax(temp_waveIntensity)
    SetAxis bottom 0,wavemax(W_energy_keV)
    String origFileName = stringList_filenames[i]
    TextBox/C/N=text0/F=0/A=MC origFileName // TEXTBOX W FILENAME
    TextBox/C/N=text0/A=RT/X=7.88/Y=20.61
    EndIf

    //Add tags!
    Variable ptLoc_Energy_val
    String atomicElements_String, tagName
    For(k=0;k<numpnts(XPosition_keV);k+=1)
        If((flag_loc[k]==1) && (temp_WaveIntensity[ptLoc_energy_keV[k]]>=400))
        If(flag_plots==1)
        ptLoc_Energy_val = ptLoc_Energy_keV[k]
        atomicElements_String = AtomicEl_onSpect[k]
        tagName=reNameIntensity+"_"+num2str(k)+"_tag"
        •Tag/C/N=$tagName/F=0/X=2/Y=10.00/L=1 $reNameIntensity, ptLoc_Energy_val, atomicElements_String
        EndIf
        Intensity_onSpect[k] = temp_WaveIntensity[ptLoc_energy_keV[k]]
        EndIf
    endfor


    EndFor //should be with original for (based on i)

End

Function getCorrectElements(textWave_x)
    Wave/t textWave_x

    Variable i
    String origString

    Make/o/t/n=(numpnts(textWave_x)) elementNumberText // to hold extracted cells

    For(i=0; i<numpnts(textWave_x);i+=1)
        origString = textWave_x[i]
        //elementNumberText[i] = ""
        If(StringMatch(origString, "*OXINSTLABEL*")==1)
            elementNumberText[i] = origString[StrLen(origString)-2, StrLen(origString)-1]
        EndIf
    EndFor

    //Convert to Integers
    MAKE/o/n=(numpnts(textWave_x)) elementNumberInt
    For(i=0;i<(numpnts(textWave_x));i+=1)
        elementNumberInt[i] = str2num(elementNumberText[i])
    EndFor
End
```

GEOS_Chem_Comparison - Igor Pro 6.37 - [GEOS_Chem_Toolz]

File Edit Data Analysis Macros Windows Procedure Misc Help

```
// ------------------------------- SIZE VS SHEAR STRESS ------------------------------- \\
Function sizeVSthreshold()

    //CALCULATE AIR DENSITY
    Wave AirTC_Avg_1_5m, rel_humidity_1_5m, BP_mb
    Duplicate/o BP_mb, BP_Pa
    BP_Pa = BP_mb*100
    Make/o/n=(numpnts(AirTC_Avg_1_5m)) rho_air
    Make/o/d/n=(numpnts(AirTC_Avg_1_5m)) p_sat //saturation vap pressure
    Variable AirTemp_K, i
    For(i=0;i<numpnts(AirTC_Avg_1_5m); i+=1) // calculating the air density
        if(numtype(AirTC_Avg_1_5m[i])==0 && numtype(BP_Pa[i])==0)
        p_sat[i] = 6.1078*10^((7.5*AirTC_Avg_1_5m[i])/(237.15+AirTC_Avg_1_5m[i])) // in mb
        p_sat[i] = p_sat[i] // in Pa but got rid of conversion bc of RH
        AirTemp_K = AirTC_Avg_1_5m[i] + 273.15 // convert celcius to kelvin
        rho_air[i] = ((rel_humidity_1_5m[i]*p_sat[i])/(461.495*AirTemp_K)) + ((BP_Pa[i] - (rel_humidity_1_5m[i]*p_sat[i]))/(287.058*AirTemp_K)) // kg/m3
        Else
        p_sat[i] = NaN
        rho_air[i] = NaN
        EndIf
```

GEOS_Chem_Comparison - Igor Pro 6.37 - [GEOS_Chem_Toolz]

File Edit Data Analysis Macros Windows Procedure Misc Help

```
        EndIf
    EndFor

    // VARIABLES
    Variable A_dimless_param, acc_grav, rho_particle, soil_moisture
    A_dimless_param = 6.5
    acc_grav = 9.8 // m/s2
    rho_particle = 2600 // g/cm3
    soil_moisture = 0.050 // no units

    Make/o/n=210 particle_diameters_4test
    particle_diameters_4test[0] = 0.3
    particle_diameters_4test[1] = 0.5
    particle_diameters_4test[2] = 0.8
    particle_diameters_4test[3] = 1.6
    particle_diameters_4test[4] = 3.0
    particle_diameters_4test[5] = 5
    particle_diameters_4test[6] = 8
    Variable i
    For(i=7;i<numpnts(particle_diameters_4test);i+=1)
    particle_diameters_4test[i] = i+2
    EndFor
    particle_diameters_4test = particle_diameters_4test/10^6 // convert to meters
    //CALC THRESHOLD VELOCITY
    Make/o/n=(numpnts(particle_diameters_4test)) u_t_forComp
    For(i=0;i<numpnts(particle_diameters_4test);i+=1)
    u_t_forComp[i] = A_dimless_param*sqrt( ((rho_particle - 1.132226188)/1.132226188)*acc_grav*particle_diameters_4test[i])*(1.2+0.2*log(soil_moisture))
    EndFor
    particle_diameters_4test = particle_diameters_4test*10^6
    Display u_t_forComp vs particle_diameters_4test
End
```

Appendix F: APS Data Analysis

Kluane Data - Igor Pro 6.37 - [JTools]

File Edit Data Analysis Macros Windows Procedure Misc Help

```
function makeSizeBinsAPS(particle_sizes)
	Wave particle_sizes
	Variable x
	x =  numpnts(particle_sizes)+1
//	Make/o/n=(x) bins
//	bins[0]=particle_sizes[0]
//	bins[1]=particle_sizes[1]
//	Variable i
//	For(i=2;i<numpnts(particle_sizes)-1;i+=1)
//		bins[i]=(particle_sizes[i+1]+particle_sizes[i])/2
//	endfor
//	bins[numpnts(particle_sizes)] = (particle_sizes[numpnts(particle_sizes)-1] - particle_sizes[numpnts(particle_sizes)-2])+particle_sizes[numpnts(particle_sizes)-1]

	Make/o/n=(numpnts(particle_sizes)) midpnts_OPC
	midpnts_OPC[0]=particle_sizes[0]
	Variable i
	For(i=0;i<numpnts(particle_sizes)-1;i+=1)
		midpnts_OPC[i+1]=(particle_sizes[i+1]+particle_sizes[i])/2
	endfor

end

function normalizetoBinSizes(vector1,matrix1)
	Wave vector1
	Wave matrix1
	Variable x
	x = numpnts(vector1)
	Variable x_1 = x-1
	Make/o/n=(dimsize(matrix1,0),dimsize(matrix1,1)) dNlogDp
	Variable i
	Variable j
	For(i=0;i<dimsize(matrix1,0);i+=1)
		For(j=0;j<numpnts(vector1)-1;j+=1)
			dNlogDp[i][j]=matrix1[i][j]/(log(vector1[j+1])-log(vector1[j]))
		endfor
	endfor
end
```

Appendix G: APS Stokes Correction

```
Function stokesCorrection(bins, particle_sizes, acc_bins, raw_ChanData,T_air, P_air, RH_air)
	Wave bins, particle_sizes, acc_bins, raw_ChanData,T_air, P_air, RH_air
	Make/o/n=(numpnts(acc_bins)) D_a_1
	D_a_1 = initialAeroDias(bins, particle_sizes, acc_bins) // get the uncorrected diameters corresponding to each accumulation bin

	//Get the average air density, viscosity
	Variable air_density, air_viscosity
	air_density = airDensity(T_air, P_air, RH_air)//airDensity(T_air, P_air, RH_air)
	air_viscosity = airViscosity(T_air)//airViscosity(T_air)

	//Get particle density

	// Go through each accumulator to calculate the correct D_a
	Variable i,j, R_one, R_two, temp_acc, temp_D,D_a_2
	Variable denom, numer
	Make/o/n=(numpnts(acc_bins)) W_correctDias
	For(i=0;i<numpnts(acc_bins);i+=1)
	// cut out all bins under limit of APS
		temp_acc = acc_bins[i]
		temp_D = D_a_1[i]
		R_one = R_1(air_density, air_viscosity, temp_acc,temp_D)		// get R_1
		D_a_2 = temp_D // start w. D2 = D1
		//print num2str(R_one)
		// Five iterations to calculate new diameter
		Variable rho_particle
		If(temp_D<2.5)
			rho_particle = 1.6
			For(j=0;j<30;j+=1)
				R_two =R_2(air_density, air_viscosity, temp_acc, D_a_2, rho_particle)
				denom = 6+(R_one^.666667)
				numer = 6+(R_two^.666667)
				D_a_2 = temp_D*((numer/denom)^0.5)
			EndFor
		Else
			rho_particle = 1.6
			For(j=0;j<30;j+=1)
				R_two =R_2(air_density, air_viscosity, temp_acc, D_a_2, rho_particle)//r_2(air_density, air_viscosity, temp_acc, D_a_2, 2.6)
				denom = 6+(R_one^.666667)
				numer = 6+(R_two^.666667)
```

```
                                D_a_2 = temp_D*((numer/denom)^0.5)
                        EndFor
                EndIf
                W_correctDias[i] = D_a_2
        EndFor
        //¥DeletePoints 0,181, W_correctDias
        //String rename_wave = nameOfWave(raw_ChanData)+"_stokes"
        //Duplicate raw_ChanData, $rename_wave
        //¥DeletePoints/M=1 0,181, $rename_wave
        //sortNumberConcs(W_correctDias, raw_ChanData, acc_bins, bins)
End
Function initialAeroDias(bins, particle_sizes, acc_bins) //Warning: this function has to be
manually aborted??
        Wave bins                       // size bins (sides of bins)
        Wave particle_sizes // mean per bin
        Wave acc_bins                   // Raw data accumulator channels

        // From PSL calib curve, calculate which accumulator bins correspond to which sizes
        Make/o/n=(numpnts(bins)) acc_bin_equiv
        acc_bin_equiv = -10^-13*bins^5+4*10^-10*bins^4-4*10^-7*bins^3+2*10^-4*bins^2-
0.0321*bins+1.2556

        // New wave with the INITIAL aerodynamic diameters corresponding to the acc bins
        Make/o/n=(numpnts(acc_bins)) D_a_1
        Variable b,m
        m = 41.628
        b = 156.63
        D_a_1 = (acc_bins-b)/m

        return D_a_1 // initial calculation of aerodynamic diameters

//      // New wave with the aerodynamic diameters corresponding to the acc bins
//      Make/o/n=(1023) D_a_1 // Original D_a assigned by instrument. Each indice
corresponds to raw data bins.
//      Variable i, j
//      i=1
//      j=0
//      do
//              If(acc_bins[j]<acc_bin_equiv[i])
//                      D_a_1[j] = particle_sizes[i-1]
//                      j+=1
//              Else
//                      i+=1
//              EndIf
//      while (i<(numpnts(acc_bin_equiv)))
//
```

```
//	return D_a_1 // return wave with mean dia for each channel number
End
Function airDensity(T_air, P_air, RH_air) // gonna start with dry air for now...
	Wave T_air, P_air,RH_air
	//AIR DENSITY
	Make/o/n=(numpnts(T_air)) rho_Humid
	Make/o/n=(numpnts(T_air)) p_vap
	Variable M_d = 0.028964 //Molar mass of dry air, kg/mol
	Variable M_v=0.018016 //Molar mass of water vapor, kg/mol
	Variable P_sat,i // saturation pressure
	For(i=0;i<numpnts(T_air); i+=1)
		p_sat = 6.1078*10^((17.27*T_air[i])/(T_air[i]+237.3))
	EndFor
	p_vap = RH_air*p_sat// P in Pa (rh is in percent)
	rho_Humid = ((p_air*1000-p_vap)*M_d + p_vap*m_v)/(8.314*(T_air+273.15))// in
kg/m^3
	rho_Humid = rho_Humid*0.001 // convert to g/cm^3
	return mean(rho_Humid)
End
Function airViscosity(T_air)
	Wave T_air
	//AIR VISCOSITY
	Make/o/n=(numpnts(T_air)) air_viscosity
	Variable b = 1.458*10^-6
	air_viscosity = (b*(T_air +273.15)^(3/2))/(T_air +273.15+110.4) // in kg/(m*s) aka
Pa*s
	air_viscosity = air_viscosity*10 // conver to dynes*s/cm^2
	return mean(air_viscosity)
End
Function R_1(rho_air, air_viscosity, acc_bin_number,D_a_1)
	Variable rho_air, air_Viscosity
	Variable acc_bin_number // to be converted to average particle velocity
	Variable D_a_1 // uncorrected aerodynamic diameter

	//Necessary variables
	Variable Air_Vel = 15000 //		cm/s
	Variable Particle_Vel = 100*10^5/(acc_Bin_number*4) // convert to cm/s from um/ns
um/ns
	Variable R_1
	R_1 = (rho_air*(air_vel-particle_vel)*D_a_1)/(air_Viscosity*sqrt(1.05))

	return R_1
End
Function R_2(rho_air, air_viscosity, acc_bin_number, D_a_2, rho_particle)
	Variable rho_air, air_Viscosity
	Variable acc_bin_number // to be converted to average particle velocity
```

```
	Variable D_a_2 // corrected aerodynamic diameter
	Variable rho_particle

	//Necessary variables
	Variable Air_Vel = 15000 //		cm/s
	Variable Particle_Vel = 100*10^5/(acc_Bin_number*4) // convert to cm/s from um/ns
um/ns
	Variable R_2
	R_2 = (rho_air*(air_vel-particle_vel)*D_a_2)/(air_Viscosity*sqrt(rho_particle))

	return R_2
End
Function sortNumberConcs(W_correctDias, raw_ChanData, acc_bins, bins) // put the number
concentrations into the correct size bin
	Wave W_correctDias, raw_ChanData, acc_bins, bins

	//new raw channel matrix
	Make/o/n=((dimsize(raw_ChanData,0)), (numpnts(bins)-1)) new_dN

	//numpnts in W_correctDias should equal number of columns of the raw_ChanData
matrix

	Variable i,j,k,temp_dN, start_index, end_index

	For(i=1;i<(numpnts(bins)-1);i+=1)			// i is the size bins index (new_dN
columns)
		For(j=0;j<numpnts(W_correctDias);j+=1)// j is the acc bins index (raw_dN
columns); FIND the start & end
			if((W_correctDias[j]>=bins[i-1])&&(W_correctDias[j-1]<bins[i-1]))
				start_index = j
			ElseIf((W_correctDias[j]<=bins[i])&&(W_correctDias[j+1]>bins[i]))
				end_index = j
			EndIf
		EndFor

		For(j=start_index;j<=end_index;j+=1) // add all those columns to the new
matrix
			For(k=0;k<dimsize(raw_ChanData,0);k+=1)
				new_dN[k][i] = new_dN[k][i] + raw_ChanData[k][j]
			EndFor
		EndFor

	EndFor
End
Function checkForNans(matrix1)
	Wave matrix1
```

```
	Variable i,j
	For(i=0;i<dimsize(matrix1,0);i+=1)
		For(j=0;j<dimsize(matrix1,1);j+=1)
			if(numtype(matrix1)==2)
				Print "NaN at: " + num2str(i) + "," + num2str(j)
			EndIf
		EndFor
	EndFor
End
//	Wave W_correctDias, raw_ChanData, acc_bins, bins
//
//	//new raw channel matrix
//	Make/o/n=((dimsize(raw_ChanData,0)), (numpnts(bins)-1)) new_dN
//
//	Variable i,j,k
//	For(i=0;i<(numpnts(bins)-1); i+=1)			// index for bins of sizes
//		For(j=0;j<numpnts(W_correctDias);j+=1) // Index for acc bins
//			If((W_correctDias[j]>=bins[i])&&(W_correctDias[j]<bins[i+1])) // if
the acc bin corrected dia is within the size bin....
//				For(k=0;k<dimsize(raw_ChanData,0);k+=1) //rows
//					new_dN[k][i] = new_dN[k][i] + raw_ChanData[k][j]
//					//checkForNans(new_dN)
//				EndFor
//			EndIf
//		EndFor
//	EndFor
Function rawToNumberConc(raw_ChanData)
	Wave raw_ChanData
	Duplicate/o raw_ChanData, raw_ChanData_treated

	Variable i,j
	For(i=0;i<dimsize(raw_ChanData_treated,0);i+=1)
		For(j=0;j<dimsize(raw_ChanData_treated,1);j+=1)
			raw_ChanData_treated[i][j] =
raw_ChanData_treated[i][j]/((5/6)*1000*4.9)
		EndFor
	EndFor
	String treatedWave
	treatedWave = "treated_"+nameofWave(raw_chanData)
	Duplicate/o raw_ChanData_treated, $treatedWave
End
```

Appendix H: SEM Images and SEM/EDS Mapping Results